TÉCNICO LISBOA

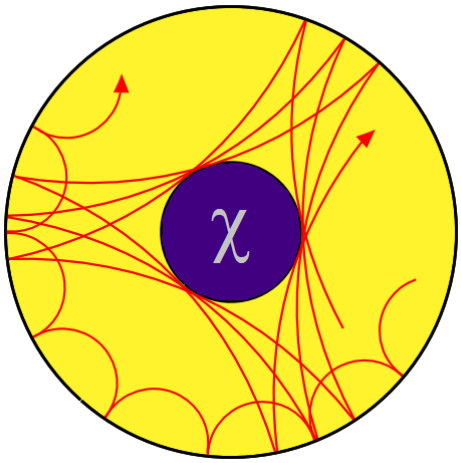

Asymmetric Dark Matter constraints from Asteroseismology:

Using subgiant stars as a probe

João Pedro Inácio da Silva Rato

Thesis to obtain the Master of Science Degree in

Engineering Physics

Supervisor: Prof. Ilídio Pereira Lopes

Examination Committee

Chairperson: Prof. José Pizarro de Sande e Lemos
Supervisor: Prof. Ilídio Pereira Lopes
Member of the Committee: Prof. Justin Christopher Feng

December 2020

”He that breaks a thing to find out what it is,
has left the path of wisdom.”

– J. R. R. Tolkien (1892-1973)
The Fellowship of the Ring (1954)

To my parents.

Acknowledgments

With this journey coming to a close, I look back at the people who made it all possible. It is hard to put a finger on how many individuals impacted my path these last 5 years but my wish is that I could impact as many of you.

First of all, I express my heartfelt gratitude towards my supervisor, Professor Ilídio Lopes, for the confidence he showed in me, the steadfast availability to discuss our work, the invaluable advices and the free reins he gave me to pursue my interests. I also thank the members of CENTRA who helped me along the way. Particularly, José Lopes, for sharing his work with me and showing interest while withstanding the hours of discussions about my work without which I could not have progressed as far as I did.

To my closest friends, who encouraged and inspired me to continue this effort, thank you. Whether you showed interest on my studies and asked physics questions at five in the morning or you answered my own, I deeply cherish those moments. During this time, when socialising was ill-advised, my friends still offered escapes and made me live life as it is supposed to be lived: laughing.

Lastly and most importantly, I thank my Mother and Father for their care, unconditional love and support throughout my whole life and education. Without their vision and sacrifices I would not have had the opportunities I have been so lucky to have nor would I be in the position to pursue even more. Thanks Mom for putting aside your comfort and work-life these past months so that I could focus on my work, in this atypical year where we all had to work from home.

Resumo

Até ao momento a procura por Matéria Escura (ME) tem sido inconclusiva. O uso da asterosismologia tem vindo a ser explorado para assistir neste esforço. Agindo como uma sonda do interior estelar, a asterosismologia permite-nos estudar as regiões mais afectadas por ME nas estrelas. Como a ME é capturada e acumulada no núcleo da estrela, irá produzir maiores efeitos nessa zona, podendo mudar a sua estrutura.

Nesta dissertação, fazemos uso de modelos de evolução estelar para, pela primeira vez, estudar os efeitos da ME Assimétrica (MEA) numa estrela subgigante. Por comparação directa com observações e modelos estelares sem contribuição de ME, estabelecemos a existência de dois regimes que se apresentam dependendo da intensidade das interacções ME-barião no interior da estrela.

Numa segunda fase do trabalho, descobrimos que modelos com uma secção eficaz de interacção dependente do spin entre 10^{-40} e 10^{-38} cm^2 tendem a concordar melhor com os dados observacionais do que modelos sem presença de ME. Estas descobertas foram corroboradas com o uso de diagnósticos asterosísmicos relevantes, definidos para uma melhor análise da estrutura do núcleo da estrela e, portanto, demonstram que a presença de MEA em estrelas deste tipo não é incompatível com a realidade. Estes limites definidos no espaço de parâmetros de ME complementam os estabelecidos por detecção directa. Os métodos apresentados possibilitam a construção de diagramas de exclusão para a massa das partículas de ME e secção eficaz. Espera-se que as próximas missões asterosísmicas possam proporcionar dados ainda mais precisos que certamente serão valiosos neste contexto.

Palavras-chave

Matéria Escura; Asterosismologia; Estrelas Subgigantes; Modelação estelar

Abstract

As of now, the search for Dark Matter (DM) has been inconclusive. Asteroseismology has been pursued in hopes of helping in this endeavour. By acting as a probe into the stellar interior, stellar oscillations allow us to study the most affected regions by DM in stars. Since DM is captured and accumulated in a star's core it will produce greater effects there, possibly changing its structure.

In this work, we make use of stellar evolution models to study for the first time the effects of Asymmetric DM (ADM) in a subgiant star. By direct comparison with observations and stellar models with no DM contribution, we establish the existence of two different regimes that are present depending on the strength of DM-baryon interactions inside the star.

In a second phase of the work, we find that models with a spin-dependent interaction cross section between 10^{-40} and 10^{-38} cm^2 tend to better agree with the observational data than models with no DM presence. These findings were corroborated via the use of relevant asteroseismic diagnostics defined to better infer on the core's structure and, thus, showcase that the presence of ADM in stars of this type is not incompatible with reality. These limits in DM parameter space complement the ones established by direct detection experiments. The methods displayed in this work open the possibility to draw exclusion diagrams for DM particle mass and cross section. Future asteroseismic missions are expected to provide even more precise data which will be valuable in this context.

Keywords

Dark Matter; Asteroseismology; Subgiant Stars; Stellar Modelling

Contents

List of Figures

List of Tables

Acronyms

ADM	Asymmetric Dark Matter
CDM	Cold Dark Matter
CMB	Cosmic Microwave Background
CNO	carbon-nitrogen-oxygen
DM	Dark Matter
HR	Hertzsprung-Russell
KIC	Kepler Input Catalog
ΛCDM	Lambda Cold Dark Matter
MESA	Modules for Experiments in Stellar Astrophysics
MS	main-sequence
PLATO	PLAnetary Transits and Oscillations of stars
RG	red giant
SD	spin-dependent
SG	subgiant
SI	spin-independent
SSG	Standard Subgiant
WIMP	Weakly Interactive Massive Particle

Nomenclature

Physics Constants

h	Reduced Hubble constant	$H_0/(100\ \mathrm{km\ s^{-1}Mpc^{-1}})$
c	Speed of light in a vacuum inertial system	$299,792,458\,m/s$

Physical Quantities

m	Mass
σ	Cross-section of interaction
M	Stellar mass
r	Radius
R	Stellar radius
ρ	Density
p	Pressure
T	Temperature
Φ	Gravitational potential
l	Rate of energy transfer
ε	Energy rate per unit mass
ν	Frequency
ω	Angular frequency
$\Delta\nu$	Large frequency separation
$\delta\nu$	Small frequency separation

r_{02}	Small to large frequency separation ratio
$\Delta\Pi$	Period separation
ξ	Displacement
K	Knudsen number
Ω_x	Density parameter

Subscripts

χ	Dark matter quantity
$\odot$	Solar quantity
0	Equilibrium quantity
nuc	Nuclear quantity
gr	Gravitational quantity
ν	Neutrino quantity
SD	Spin-dependent quantity
SI	Spin-independent quantity
eff	Effective quantity
n	Radial order
ℓ	Spherical degree
m	Azimuthal order
star	Stellar quantity
seis	Seismic quantity

1

Introduction

Contents

In the last century, the existence of additional energy density and mass contributions to the content of the universe has presented itself as one of the biggest conundrums to the scientific community. Stemming from our lack of knowledge, those contributions are rightfully called Dark Energy and Dark Matter (DM) (e.g., [1]).

In 1933, Fritz Zwicky inferred the existence of the "missing matter" by analysing the velocity dispersion of galaxies in the Coma Cluster [2], which was greater than it could be if only luminous matter was present. Later, in the 1970s, Rubin & Ford [3] extended this notion when they found that the rotation curves of galaxies were not in agreement with their visible matter content: the stars farther from the galactic centre are moving faster than expected, hinting towards the presence of some form of invisible matter.

Since those discoveries, the efforts to find this exotic matter have not stopped. More recently, in 2018, the Planck Collaboration [4] released their results on the Lambda Cold Dark Matter (ΛCDM) model parameters from measurements of the Cosmic Microwave Background (CMB) temperature anisotropies. They revealed a matter density parameter of Ω_m = 0.315 $\pm$ 0.007, with the baryonic density $\Omega_b h^2$ = 0.0224 $\pm$ 0.0001 and dark matter density $\Omega_c h^2$ = 0.120 $\pm$ 0.001, which points towards baryonic matter having a contribution of about 5% of the density and Cold Dark Matter (CDM) contributing around 26%. The dark contributions then comprise close to 95% of the total density of the universe. It is then pivotal for the understanding of the universe that we get to know more about this unknown sector. This work aims to partake in that endeavour, by using asteroseismology to study DM and its effects on a subgiant star. From that, our goal is to find new ways to constrain DM properties by applying appropriate asteroseismic diagnostics.

This chapter marks the introduction to this thesis. Firstly, we cover the state-of-the-art of DM research as well as pertinent historical findings, while also discussing the relevant DM candidates and the exclusion limits found for those by direct detection experiments. Then, we establish the connection between stars and the search for DM. We also introduce asteroseismology as a tool to analyse stars and give a brief overview of past, current and future missions that help in that analysis. Finally, the thesis goals and outline are presented as well as the original contributions that accompany this dissertation.

1.1 Dark Matter candidates and established limits

DM is often subdivided into three thermal types: hot, warm and cold. The non-relativistic CDM is regarded as the largest content of total DM since it can account for most relic density and reproduces observations in numerical simulations of large scale structures [5, 6]. Besides, this type of DM is preferred by the properties of the CMB [7]. However, CDM also has its flaws like the apparent lack of predicted substructures – the so-called missing satellites problem [8, 9] – or it predicting too dense

regions towards the centre of the largest simulated DM sub-halos when comparing to the brightest observed dwarf satellite galaxies – the too-big-to-fail problem [10, 11]. A straight forward solution is to consider DM to be mostly cold but also have warm or hot components. Thus, the DM candidate particle problem spans quite a range of possibilities.

The current belief is that DM interacts weakly with itself and ordinary matter, except through gravity. The term ”weak” is not only referring to the strength of the interactions but also their nature (the weak nuclear force). DM candidate research has yielded possibilities within more than 30 orders of magnitude in DM particle mass (m_χ) and about 40 in DM-nucleon interaction cross section ($\sigma_{\chi n}$). Figure 1.1 showcases this wide range of prospects, by plotting the most relevant candidates in DM parameter space, with colour coding for hot, warm and cold DM as red, pink and blue, respectively. It is noticeable that there is a heavily populated region holding most of the candidates between masses 10^{-9} and 10^{6} GeV and cross section below 10^{1} pb (10^{-35} cm^2).

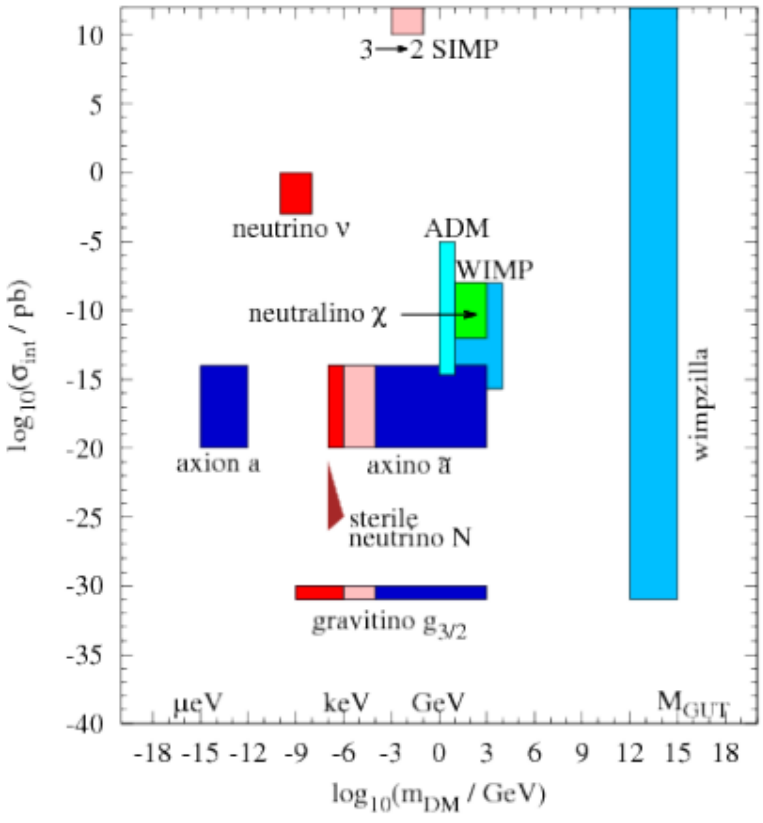

Figure 1.1: DM candidates in parameter space (m_χ, σ), taken from Baer *et al.* [12].

Recent reviews and studies (see, e.g., [1, 7, 13, 14]) discuss this wide array of possible candidates and focus on a particular type of particles which stand out as one of the primary choices: the Weakly

Interactive Massive Particle (WIMP) [15]. WIMP production is mostly explained by the freeze-out mechanism where DM particles decoupled from the early hot Universe plasma by freezing out of equilibrium due to the expansion and cooling of the Universe. While still in equilibrium with standard particles, DM particle production from annihilation balanced each other out. These are particularly favoured when compared to other possibilities due to their appearance in many theoretically well-motivated models. Besides, WIMPs are a promising target for direct detection experiments since their expected detection rates fall on the current (and future) detectors' spectrum (e.g., [16, 17]) and so they are naturally more interesting by being testable by experiment.

Naturally, many of these experiments have been held in the hope of finding these elusive particles (see e.g., [18, 19] and references therein). Despite no detection yet being confirmed (e.g., [20]), a vast number of constraints on the mass and cross section of interactions of WIMPs with baryons have been set [21]. These interactions are usually treated in two separate components: spin-dependent (SD), σ_{SD}, and spin-independent (SI), σ_{SI} [22]. For WIMP masses around $m_\chi \simeq 5$ GeV, recent upper limiting constraints on σ_{SD} (WIMP-proton interactions) have been placed at slightly below 10^{-37} cm^2 by PICASSO [23] and at around 10^{-39} cm^2 by PICO-60 [24]. The XENON-100 experiment [25] placed a limit for σ_{SD} at $\sim 2.5 \times 10^{-36}$ cm^2 for $m_\chi \sim 9$ GeV, while LUX [26] reported an exclusion limit around σ_{SD} = 10^{-36} cm^2 at $m_\chi = 5$ GeV. For σ_{SI} (WIMP-nucleon interactions) the upper limits were found to be at around 5×10^{-41} cm^2 (from both PICASSO and PICO-60). Figure 1.2 displays these results and other relevant ones in what is the state-of-the-art of WIMP direct detection experiments.

Recently, the term WIMP has branched out into somewhat different definitions. Historically, WIMPs require a non-negligible self-annihilation cross section to produce, via a thermal mechanism, the correct abundance of dark matter measured today. However, much like baryons in baryogenesis, it has been hypothesised that a relic asymmetry may have been produced by parent WIMPs in a process often called darkogenesis (e.g., [27]). Succinctly, it is possible to construct a minimal weakly coupled dark sector which generates a matter-antimatter asymmetry that does not disagree with transfers of asymmetry to the standard model sector [28]. Moreover, this Asymmetric Dark Matter (ADM) scenario can be obtained by assuming that one component of the DM relic density from freeze-out is accompanied by one which is set by an initial asymmetry between DM and their anti-particles [29, 30]. Therefore, asymmetric WIMPs, or WIMPs in an ADM scenario, although not used historically, is a widely employed term for ADM particles that comply with all the WIMP requirements except the symmetry. In this work we will consider this type of matter and formalism, hereby referencing the objects of our study as ADM particles. In the ADM framework, the DM and anti-DM densities are unbalanced and make the present-day DM self-annihilation negligible. This choice of framework is mainly interesting in the standpoint of the DM influence on stars: since DM self-annihilation does not occur, the number of DM particles inside a star will naturally be larger than it would be otherwise, making the star more sensible to its effects, which

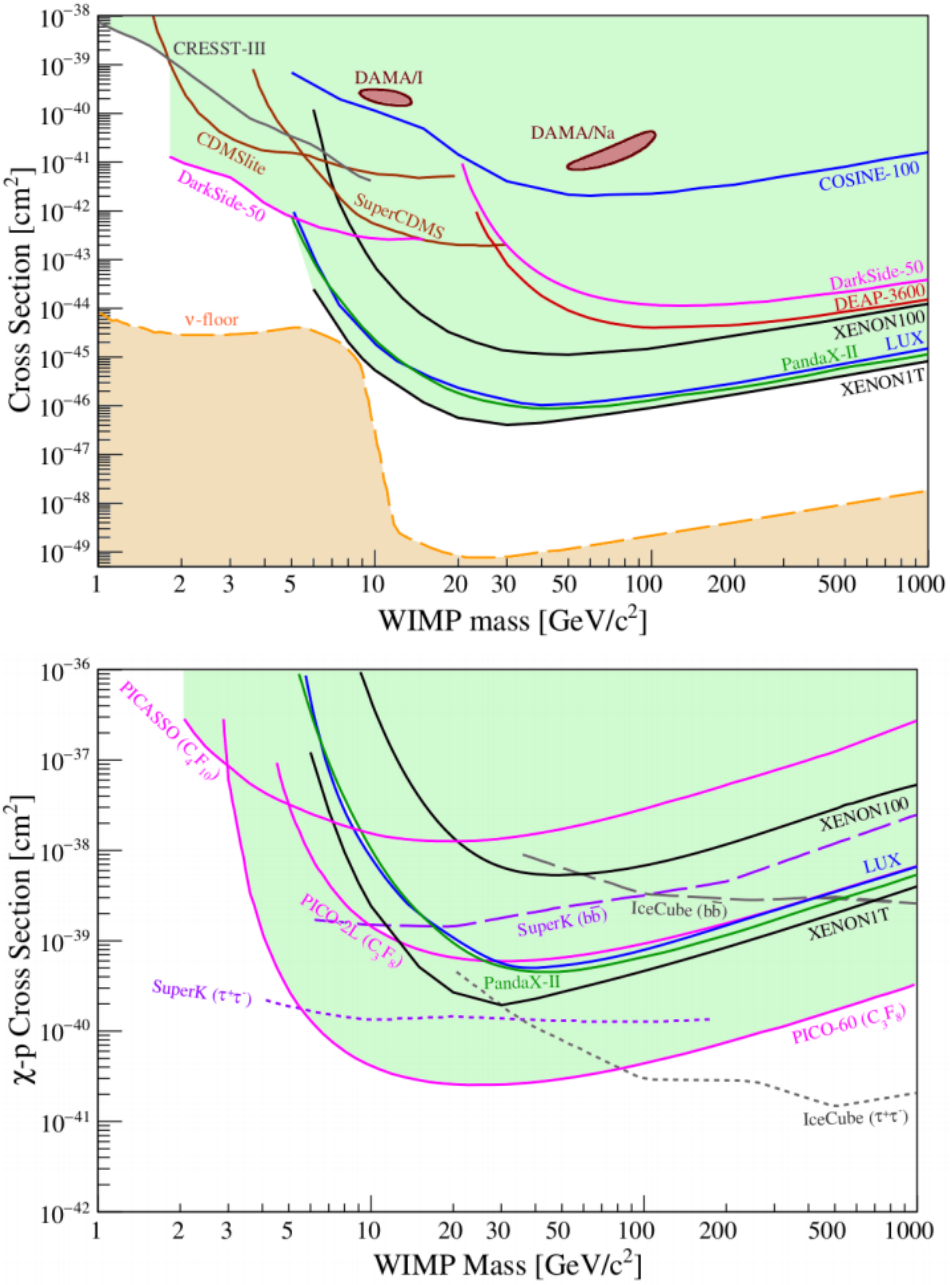

Figure 1.2: Direct detection experiments' latest results, taken from Schumann [20]. **Top:** Spin-independent WIMP-nucleon cross sections. **Bottom:** Spin-dependent coupling in WIMP-proton interactions.

allows for a better study of DM phenomena.

1.2 Stars as Dark Matter laboratories

Large astronomical bodies are now viewed as valuable DM laboratories since, if existent, DM particles are gravitationally attracted and captured by those bodies if their velocity can decrease to below the escape velocity by scattering off of the body's matter (e.g., [31]). As seen before, in the case of WIMPs, DM particles interact (even if feebly) with baryonic matter, thus new or amplified phenomena are expected to appear in those bodies. In the specific case of stars, DM particles will interact stochastically with the plasma, transferring energy from hotter regions to colder ones (from the core outwards). Analogous to the capture, the reverse process may also occur: evaporation. In this case, particles that were already trapped inside the star gain energy from scattering off of the local particles, such that they escape the gravitational pull. Depending on the theoretical framework, DM annihilation may also occur in the stellar core. Naturally, these three processes – capture, evaporation and annihilation – govern the rate of change of the number of DM particles in a star. Since our work is exploring the ADM scenario, annihilation will be neglected, leaving us with the remaining two processes. However, it has been found that, for sun-like stars, the DM mass above which evaporation is also negligible is close to 3.3 GeV (e.g., [32, 33]). Thus, in some specific regimes it would be acceptable to consider capture as the sole process that dictates accumulation of DM particles inside a star. Later on in this document these phenomena will be delved into with more detail.

It is now clear that analysing stars can help in bringing conclusions to the DM field. This analysis can range from observational to stellar modelling or a combination of the two. This field of study has been growing and, particularly for stars, these endeavours have ranged from the study of solar models affected by DM (e.g., [34]) to asteroseismic analysis (e.g., [35–37]) also including neutrino flux constraints (e.g., [38, 39]). The results have been exciting, with distinct and plausible processes happening inside stars that can be explained by the presence of DM particles.

However, using stars and stellar models as an object of study of DM also has its shortcomings, which are mostly inherited from standard stellar modelling. A notable example among these is the so-called solar composition problem or solar abundance problem. Standard solar models using the most recent photospheric abundances (AGSS09 [40]) as inputs present a contradictory prediction of the Sun's internal structure when compared to high-precision results from helioseismology (e.g., [41, 42]). This discrepancy between predictions coming from spectroscopy and helioseismology renders the determination of stellar properties (such as the sound speed profile) through stellar modelling more problematic and affects not only the modelling of the Sun but also other stars since they rely on solar inputs for some quantities, like the relative metallicity $(Z/X)_\odot$. In a recent discussion of this problem,

Capelo & Lopes [43] have shown that measuring neutrino fluxes from the carbon-nitrogen-oxygen (CNO) cycle with a precision that could be achieved by the next generation of experiments could help resolve this issue. While this problem can hinder the ability of using stellar modelling to probe DM properties, DM itself can also be an answer to the abundance problem since it introduces different physics in the interior of stars. Particularly, Lopes *et al.* [44] proposed that the accretion of DM in the Sun's core could lead to a better agreement between helioseismic and neutrino data. In a follow up with a more detailed analysis, Vincent *et al.* [45] show that the solar abundance problem could be solved by the presence of a light asymmetric dark matter particle. The solar abundance problem is then both a hindrance and a motivation to our work. With more precise measurements coming from future spectroscopic missions, abundance calculations will certainly improve in precision. Missions like the Gaia-ESO survey [46], which complements the massive Gaia [47] effort by providing high-resolution spectra for more than 100000 stars, are certainly valuable for the study of stellar chemical abundance and will help in debunking this issue.

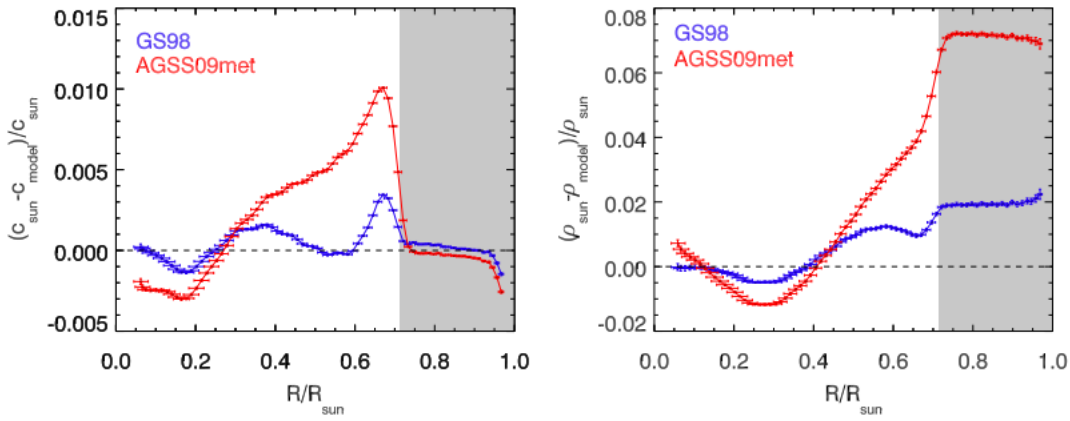

Figure 1.3: Relative difference in sound-speed (c) and density (ρ) profiles for 2 solar chemical compositions, taken from Bergemann & Serenelli [48].

1.3 Asteroseismology as a stellar probing tool

Much alike to what is done on Earth by seismologists, the use of seismic techniques to study stars has been responsible for much of the current knowledge on their interior. For example, helioseismology (asteroseismology applied to our Sun) has delivered remarkable results (see, e.g., Turck-Chièze & Couvidat [49] and references therein). The amount of observed acoustic modes (more than 8000) and the precision of their measurement (up to $\sim 10^{-4}\%$) has enabled many conclusions and inferences on the inner regions of the Sun. In particular, a detailed picture of rotation in the solar interior has been achieved by a precise analysis of the oscillation frequencies (e.g., [50, 51]). Additionally, by applying

inversion techniques it was shown that the solid-body-like profile of the Sun is present down to at least $r \sim 0.2\ \mathrm{R}_\odot$ (e.g., [52]). An extensive review on the topic of asteroseismology is given by Chaplin & Miglio [53].

Interestingly, asteroseismology has been thoroughly exploited in an attempt to find constraints for the properties of DM while using stars as laboratories (e.g., [54]). The premise is fairly straightforward: by analysing oscillation frequencies of stars we can extract valuable information of their interior structure. This is useful for studies related to DM since, as seen before, these particles accumulate inside the star and introduce an additional energy transport mechanism. This can naturally lead to changes in the structure of the star, which can be probed via asteroseismic diagnostics (e.g., [54, 55]).

Understandably, observational data is pivotal to improve this analysis. In that front, missions like CoRoT [56, 57], *Kepler* [58, 59] and TESS [60] have made progress in obtaining the oscillation frequencies of many main-sequence (MS), subgiant (SG) and red giant (RG) stars with great precision, making it possible to study the asteroseismology of stars other than the Sun. Taking full advantage of this diversity of data, seismic diagnostics can be formulated for several stars in different stages of evolution, broadening the spectre of DM laboratories.

Future missions are expected to increase the asteroseismic data both in number and precision. With the primary goal of discovering habitable extra-solar planets, the PLAnetary Transits and Oscillations of stars (PLATO) mission [61], to be launched in 2026, will extend this effort and enable more precise studies by the determination of accurate stellar masses, radii, and ages from asteroseismic data. The oscillation frequency measurements are expected to improve in precision upon those of *Kepler* while also extending the catalogue to include brighter stars. Thus, this will enable the study of the effects of DM on the stellar structure with both greater precision and for a considerably larger number of stars. These are obviously exciting news for asteroseismic studies and in particular for probing the impact of DM in stars.

Since stellar oscillations are well documented and understood, many seismic diagnostics have been defined from an asymptotic standpoint as to study specific regions or phenomena inside the star. Some of these diagnostics are covered in this work since these can be used to infer the impact of DM, expected to be more prevalent in the inner core. The general idea to perceive this impact is to model a known star, usually its whole evolution, and retrieve the oscillation frequencies at the current age. Then the referred diagnostics can be applied and compared to the ones calculated from the observational data of the same star. As it might be expected, the choice of framework and diagnostic will heavily impact the results. As it will be shown, diagnostics weighted towards the stellar core (and thus with less influence from the outer envelope) are particularly useful for this task.

1.4 Thesis Objective and Outline

This work focuses on studying, for the first time, the impact of ADM in a SG star. The object of our study is included in the Kepler Input Catalog (KIC) and is the star KIC 8228742. To study the ADM impact in it, we use a robust calibration and diagnostic method giving special attention to asteroseismic diagnostics. These allow us to build DM parameter space sensitivity diagrams and can lead to the setting of exclusion limits in m_χ and $\sigma_{\rm SD}$.

The structure of this thesis is as follows: Chapter 1 holds the introduction of this work, contextualising it within the current research status of DM and asteroseismology. Following that, Chapter 2 describes the theoretical background regarding stellar evolution and sun-like oscillations, converging onto the asteroseismology of SG stars, the object of our study. In Chapter 3 we continue the theoretical description by introducing with detail the asymmetric dark matter interactions happening inside a star and defining the framework we use.

Chapter 4 presents the new methodology used in this work. The calibration of stellar models is thoroughly explained and the most suitable asteroseismic diagnostics for the task at hand are chosen.

The results of this work are presented in two separate parts. In Chapter 5 we showcase and discuss the impact of ADM in KIC 8228742, by calibrating a set of models with and without DM interactions and comparing both to observations. Chapter 6 contains an asteroseismic analysis of 100 models of the same star with the objective of mapping in DM parameter space (m_χ, $\sigma_{\rm SD}$) the sensitivity of the chosen diagnostics to these quantities. Ultimately, it allows us to suggest exclusion limits for the mass and spin-dependent interaction cross-section of an ADM particle.

Finally, in Chapter 7 we conclude this work by discussing the general picture of the previous chapters and what these results and methodology could mean for future endeavours.

From the work displayed in this thesis, an article was written in collaboration with José Lopes & Ilídio Lopes and is included in Appendix A. It is currently pending review for publication in the Monthly Notices of the Royal Astronomical Society, with the title "*On asymmetric dark matter constraints from the asteroseismology of a subgiant star*".

2

Subgiant Stars and Asteroseismology

Contents

With an increase in spectroscopic and asteroseismic data, stars are now more understood than ever. For obvious reasons, our extensive knowledge of the Sun has proved valuable in understanding other stars, from their energy transport processes to the causes of stellar oscillations. These oscillations are a central part of our work and will be used to classify the performance of stellar models with ADM interactions taken into account.

This chapter marks the beginning of the theoretical background description. We start by covering the relevant stages of stellar evolution and then focus on the formalism of asteroseismology.

2.1 Stellar evolution and energy equations

As our work focuses on SG stars, it is crucial to understand what differs that stage of evolution from others and how a sun-like star reaches that stage.

Initially as massive gaseous clouds, stars are formed when gravitational attraction induces collapse. These clouds are rich in hydrogen and helium and may have other heavier elements if they belong to a newer population, like our Sun (e.g., [62]). Succinctly, the collapsing cloud becomes more opaque and hotter since, through accretion, more material is gathered into it. In this stage, the cloud turns into a proto-star and, if the necessary pressure and temperature conditions (met if the mass exceeds 0.08 $M_\odot$) allow for the ignition of hydrogen fusion in its core, a star is born (e.g., [63]). This new energy production mechanism will eventually balance the gravitational attraction, creating an hydrostatic equilibrium, and the star is effectively in the MS phase. In this stage the star will continue hydrogen fusion into helium in its core.

Even though this fusion is transversal to all stars, the process in which it occurs depends on their mass. For stars with masses less than or close to the Sun's, the pp-chain (proton-proton) reaction dominates the energy production. In this process, four hydrogen nuclei (protons) produce helium through two branches of reactions, with each pair of two protons fusing into deuterium at first and then fusing once again with an additional proton to create a helium light isotope ($^3_2$He). By joining the two branches, through a fusion of these two isotopes, the final $^4_2$He appears. For more massive stars, a process called carbon-nitrogen-oxygen (CNO) cycle takes over. As the name suggests, this mechanism converts H into He by utilising C, N and O isotopes as catalysts. The energy produced in either one of these processes is obviously present in the star's energy equation. Assuming spherical symmetry in a quasi-static star, the energy equation can be defined as (e.g., [63])

$$\frac{\partial l}{\partial m} = \varepsilon_{\mathrm{nuc}} - \varepsilon_\nu - \frac{\partial u}{\partial t} + \frac{p}{\rho^2}\frac{\partial \rho}{\partial t}, \tag{2.1}$$

where l is the net energy per unit time travelling outward a sphere of enclosed mass m, which is related to the shell radius r by

$$\frac{\partial m}{\partial r} = 4\pi r^2 \rho. \tag{2.2}$$

$\varepsilon_{\rm nuc}$ is the nuclear energy rate (energy per unit mass per second), ε_ν is the rate at which neutrinos take away energy per unit mass through processes not accounted for in nuclear reactions (e.g., weak interaction processes). As usual, the internal energy change is denoted as δu, p is the pressure and ρ the density. The time derivative terms may also be rewritten with respect to the entropy of the gas s in a term often denoted $\varepsilon_{\rm gr}$ for its relation with gravitational work

$$\varepsilon_{\rm gr} = -T\frac{\partial s}{\partial t} = -\frac{\partial u}{\partial t} + \frac{P}{\rho^2}\frac{\partial \rho}{\partial t}, \tag{2.3}$$

such that the energy equation may be defined by 3 distinct components,

$$\frac{\partial l}{\partial m} = \varepsilon_{\rm nuc} - \varepsilon_\nu + \varepsilon_{\rm gr}. \tag{2.4}$$

One can see that in case of contraction, the shell will release energy and $\varepsilon_{\rm gr} > 0$. On the contrary, $\varepsilon_{\rm gr} < 0$ represents expansion and will have a negative contribution to the outflow of energy. It also possible that $\varepsilon_{\rm gr} = 0$, in which we have thermal equilibrium, and energy outflow is dominated by the two remaining mechanisms. In this formalism, the enclosed mass m and time t are the Lagrangian independent variables.

The two different MS energy production processes (pp-chain and CNO cycle), which are dependent on mass and thus temperature, lead to differences in the mechanisms of energy transport. In less massive stars, the energy produced in the core is transported outwards via radiative diffusion (as is the case of the Sun) whilst in more massive stars convection is preferred. This is a clear way of distinguishing the two types of stars. Less massive stars exhibit radiative cores and convective outer layers, while a more massive star has a convective core and a radiative envelope [62]. In the first case, the temperature gradient required to carry the luminosity l by radiation is ([63])

$$\frac{\partial T}{\partial m} = -\frac{3}{64\pi^2 ac}\frac{kl}{r^4 T^3}, \tag{2.5}$$

with a being the radiation constant, k the opacity and c the speed of light. It is obvious then that the larger the luminosity l there is to be carried, the larger the temperature gradient is required. However, there is an upper limit to this since an instability in the gas appears if the temperature gradient is too high. These instabilities are what leads to convection. To describe energy transport in this case, there is the need to rely on detailed convection theory which will not be addressed in this work. Nevertheless, one useful simplified approach is the mixing length theory, a one-dimensional formalism based on rough estimates. This theory is the standard use in one-dimensional stellar evolution codes, like Modules for

Experiments in Stellar Astrophysics (MESA) [64–68] which is the backbone of the numerical part of this thesis and that solves the equations of stellar structure, such as Equations (2.1), (2.2) and (2.5), utilising different modules to treat various stellar phenomena.

The MS stage reaches an end when hydrogen is exhausted in the stellar core. Once again, mass dictates what happens next and, since our object of study has a mass around 1.3 $M_\odot$, we will focus on the evolutionary path that concerns that case. With the core being deprived of hydrogen and mostly containing helium, it does not have the necessary temperature and pressure conditions to proceed right away with helium fusion into heavier elements (like carbon). Instead, hydrogen burning continues in a shell surrounding the core. Now, the core's energy production is not sufficient to counter balance the gravitational pull and it contracts, leading to a release of gravitational energy, which in turn increases the temperature of the H-burning shell [62]. This naturally incites more nuclear reactions in that region and rises the global luminosity of the star. From that, the increasing radiation pressure will expand the star's envelope and cool it down, decreasing the effective temperature accordingly. Thus, the star is now moving rightwards in the Hertzsprung-Russell (HR) diagram and populates the so-called subgiant branch (SGB) (see Figure 2.1: horizontal line after TAMS).

The SG phase is rather short when compared to the length of the MS. The entrance of the star in the next stage, the red giant branch (RGB) (see Figure 2.1: upwards ascension after the horizontal SGB), is marked by the formation of a convective region near the surface due to the expansion and cooling of the envelope. From that, the luminosity increases because helium is still being produced in the hydrogen shell and being accreted onto the core, increasing its mass. Consequently, temperature and pressure rise, which once again galvanises the reaction rate in the shell. This cyclic behaviour will eventually come to a stop when temperature and (degenerative) pressure conditions are sufficient to ignite helium fusion in the core via the triple-alpha process [62].

All the stages of evolution referred to in this section are represented in the evolutionary track of a $1M_\odot$ star, modelled in MESA (Figure 2.1). Additional post-subgiant phases are mentioned there but will not be covered in detail as they are not pivotal for the scope of our work.

2.2 Theory of stellar pulsations

2.2.1 Perturbative analysis of the equations of hydrodynamics

Before diving into the specifics of asteroseismology of SG stars it is important to get an overview of the theory of stellar oscillations. A detailed description is given by, for example, Aerts *et al.* [70]. The formalism relies on treating the oscillations as the result of small perturbations to the equilibrium state, provided by the general equations of hydrodynamics.

These equations are the continuity equation, the equation of motion or momentum conservation

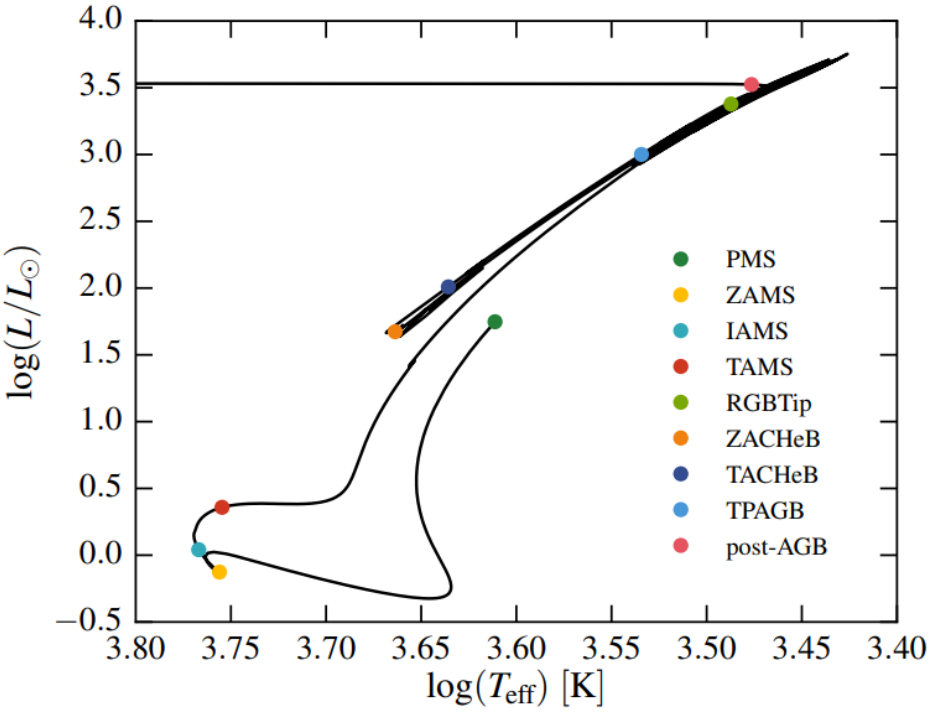

Figure 2.1: Evolutionary track of a $1M_{\odot}$ sun-like star MESA model in a HR diagram, adapted from Choi *et al.* [69]. This covers the star's life, in order, from pre-main sequence (PMS), zero age main sequence (ZAMS), intermediate age main sequence (IAMS), start of the subgiant branch (SGB) or terminal age main sequence (TAMS), tip of the red giant branch (RGBTip), zero age core helium burning (ZACHeB), terminal age core helium burning (TACHeB), thermally pulsating asymptotic giant branch (TPAGB), post asymptotic giant branch (post-AGB) finally to white dwarf cooling sequence (WDCS) which is not explicitly represented and corresponds to a decrease in luminosity and temperature starting from the horizontal line on the top left.

equation, the Poisson equation and the first law of thermodynamics, respectively,

$$\frac{\partial \rho}{\partial t} + \nabla \cdot (\rho \mathbf{v}) = 0, \tag{2.6}$$

$$\rho \frac{\partial \mathbf{v}}{\partial t} + \rho(\mathbf{v} \cdot \nabla \mathbf{v}) = -\nabla p - \rho \nabla \Phi, \tag{2.7}$$

$$\nabla^2 \Phi = 4\pi G \rho, \tag{2.8}$$

$$\frac{\mathrm{d}q}{\mathrm{d}t} = \frac{\mathrm{d}E}{\mathrm{d}t} - \frac{p}{\rho^2}\frac{\mathrm{d}\rho}{\mathrm{d}t}, \tag{2.9}$$

where $\mathbf{v}$ is the fluid velocity, Φ is the gravitational potential, $\mathrm{d}q/\mathrm{d}t$ is the heat gain term, E the internal energy and the remaining variables retain their usual meaning. For the equation of motion, the external forces were neglected as is the usual practice in the linear adiabatic formalism. An additional approximation that can be made is to take Equation (2.9) in this adiabatic regime, in which we assume no energy transfer between the waves and the gas (e.g. [63, 70]). This means that the heating term can

be overlooked and we end up with (by applying thermodynamic identities)

$$\frac{\mathrm{d}p}{\mathrm{d}t} = \Gamma_1 \frac{p}{\rho}\frac{\mathrm{d}\rho}{\mathrm{d}t}, \tag{2.10}$$

$$\text{where} \quad \Gamma_1 = \left(\frac{\partial \ln p}{\partial \ln \rho}\right)_{\mathrm{ad}}. \tag{2.11}$$

Obtaining an analytical (and even numerical) solution for Equations (2.6) to (2.8) and (2.10) is a complex task and, as such, the preferred workaround is to apply the already mentioned perturbation analysis. This is valid since the amplitudes of the oscillations are of a much smaller order than that of the stellar dimension scale. With this approach, we can redefine the scalar quantities as their values at equilibrium plus a small perturbative contribution. For example, in Lagrangian description, a scalar quantity ϕ would be

$$\phi(\mathbf{r} + \boldsymbol{\xi}, t) = \phi_0(\mathbf{r}) + \delta\phi(\mathbf{r}, t), \tag{2.12}$$

where ξ is a displacement from the equilibrium configuration and $\delta\phi$ the perturbation to the fluid. Analogously, in a stationary observer's frame (Eulerian description),

$$\phi(\mathbf{r}, t) = \phi_0(\mathbf{r}) + \phi'(\mathbf{r}, t), \tag{2.13}$$

with ϕ' denoting the perturbation to the fluid in this description. By rearranging Equations (2.12) and (2.13), we arrive to

$$\delta\phi = \phi' + \boldsymbol{\xi} \cdot \nabla\phi_0. \tag{2.14}$$

Moreover, applying the total time derivative to the scalar field one would get

$$\frac{\mathrm{d}\phi}{\mathrm{d}t} = \frac{\partial\phi}{\partial t} + \mathbf{v}\cdot\nabla\phi = \frac{\partial\phi'}{\partial t} + \mathbf{v}\cdot\nabla\phi_0 = \frac{\partial\phi'}{\partial t} + \frac{\partial\boldsymbol{\xi}}{\partial t}\cdot\nabla\phi_0 = \frac{\partial\delta\phi}{\partial t}, \tag{2.15}$$

where the relation $\mathbf{v} = \frac{\partial\boldsymbol{\xi}}{\partial t}$ was used, by neglecting higher order terms.

Applying these identities to the relevant scalar quantities of Equations (2.6) to (2.8) and (2.10) and integrating the first and last equations in time, yields

$$\rho' + \nabla\cdot(\rho_0\boldsymbol{\xi}) = 0, \tag{2.16}$$

$$\rho_0\frac{\partial^2\boldsymbol{\xi}}{\partial t^2} = -\nabla p' - \rho_0\nabla\Phi' - \rho'\nabla\Phi_0, \tag{2.17}$$

$$\nabla^2\Phi' = 4\pi G\rho', \tag{2.18}$$

$$p' + \boldsymbol{\xi}\cdot\nabla p_0 = \Gamma_{1,0}\frac{p_0}{\rho_0}(\rho' + \boldsymbol{\xi}\cdot\nabla\rho_0). \tag{2.19}$$

Furthermore, since, once again, the amplitudes of the oscillations are small when compared to the dimensions of the stellar body, we can consider a spherical symmetric equilibrium state around which these oscillations occur. The usual procedure is then to apply separation of variables to the displacement, in its radial and horizontal components, such that

$$\boldsymbol{\xi} = \xi_r \boldsymbol{e}_r + \boldsymbol{\xi}_h, \tag{2.20}$$

where $\boldsymbol{\xi}_h = \xi_\theta \boldsymbol{e}_\theta + \xi_\varphi \boldsymbol{e}_\varphi$, with $\boldsymbol{e}_i$ the unitary vector in the respective direction. Thus, by separating the angular variables and introducing spherical harmonics, $Y_\ell^m(\theta, \varphi)$, where the spherical degree ℓ and azimuthal order m obey $|m| \leqslant \ell$, we get [70]

$$\boldsymbol{\xi} = \left(\xi_r(r) Y_\ell^m,\ \xi_h(r) \frac{\partial Y_\ell^m}{\partial \theta},\ i\xi_h(r) \frac{m}{\sin\theta} Y_\ell^m \right) e^{-i\omega t}, \tag{2.21}$$

where $\xi_r(r)$ and $\xi_h(r)$ are radial dependent amplitude factors and ω is the frequency.

This formalism is analogously applied to the dependent variables and, after algebraic manipulation, the equations of linear adiabatic stellar oscillation can be written as

$$\frac{\mathrm{d}\xi_r}{\mathrm{d}r} = -\left(\frac{2}{r} + \frac{1}{\Gamma_1 p_0} \frac{\mathrm{d}p_0}{\mathrm{d}r} \right) \xi_r + \frac{1}{\rho_0 c^2} \left(\frac{S_\ell^2}{\omega^2} - 1 \right) p' + \frac{\ell(\ell+1)}{\omega^2 r^2} \Phi', \tag{2.22}$$

$$\frac{\mathrm{d}p'}{\mathrm{d}r} = \rho_0(\omega^2 - N^2)\xi_r + \frac{1}{\Gamma_1 p_0} \frac{\mathrm{d}p_0}{\mathrm{d}r} p' - \rho_0 \frac{\mathrm{d}\Phi'}{\mathrm{d}r}, \tag{2.23}$$

$$\frac{1}{r^2} \frac{\mathrm{d}}{\mathrm{d}r} \left(r^2 \frac{\mathrm{d}\Phi'}{\mathrm{d}r} \right) = 4\pi G \left(\frac{p'}{c^2} + \frac{\rho_0 \xi_r}{g} N^2 \right) + \frac{\ell(\ell+1)}{r^2} \Phi', \tag{2.24}$$

where

$$c^2 = \frac{\Gamma_1 p_0}{\rho_0} \quad \text{is the adiabatic sound speed squared,} \tag{2.25}$$

$$S_\ell^2 = \frac{\ell(\ell+1)c^2}{r^2} \quad \text{is the Lamb frequency (acoustic frequency) squared and} \tag{2.26}$$

$$N^2 = g \left(\frac{1}{\Gamma_1} \frac{\mathrm{d}\ln p_0}{\mathrm{d}r} - \frac{\mathrm{d}\ln \rho_0}{\mathrm{d}r} \right) \quad \text{is the Brunt-Väisäla (buoyancy) frequency squared.} \tag{2.27}$$

As we will see, these two last quantities are relevant to understand the oscillation regime. Equations (2.22) to (2.24) represent an eigenvalue problem where the variables are ξ_r, p' and Φ' and the eigenvalues are the squared frequencies ω^2 of the modes. As usual, these frequencies will be identified by the respective n, ℓ and m of the modes, where n is the radial order. It is possible that n is negative and this simply means that the mode has $|n|$ nodes in the region between the centre of the star and the considered radius. The reverse happens for $n > 0$. Additionally, the azimuthal order m is irrelevant for the eigenfrequencies in the absence of a magnetic field.

To solve the system, we must provide suitable boundary conditions. Because outside the star there

are no density perturbations, we can match the exterior vacuum field with the gravitational potential and its derivative in the interior of the star, such that we get the condition

$$\frac{\mathrm{d}\Phi'}{\mathrm{d}r} + \frac{\ell+1}{r}\Phi' = 0 \quad \text{as } r \to R. \tag{2.28}$$

Additionally, a second constraint comes from the star's surface. In that region the perturbation in pressure (δp) must vanish since the star is isolated,

$$\delta p = 0 \iff p' + \xi_r \frac{\mathrm{d}p}{\mathrm{d}r} = 0 \quad \text{as } r \to R. \tag{2.29}$$

This is a simplified description since the stellar surface is a lot more complicated, with atmosphere also playing a role [70, 71]. Nevertheless, this approximation is sufficient to understand the formalism in light of the scope of the work done in this thesis.

The remaining constraints come from the centre of the star. Expanding the equations near $r = 0$ it can be shown that

$$\frac{\mathrm{d}\xi_r}{\mathrm{d}r} = \frac{\ell-1}{r}\xi_r \quad \text{as } r \to 0, \tag{2.30}$$

$$\frac{\mathrm{d}\delta p}{\mathrm{d}r} = \frac{\ell}{r}\delta p \quad \text{as } r \to 0, \tag{2.31}$$

$$\frac{\mathrm{d}\delta\Phi}{\mathrm{d}r} = \frac{\ell}{r}\delta\Phi \quad \text{as } r \to 0. \tag{2.32}$$

Even with these conditions, Equations (2.22) to (2.24) are only solvable for a number of particular cases.

2.2.2 Asymptotic theory of stellar oscillations

An alternative approach was presented by Cowling [72]. By considering modes with higher n (which happen to be the most observed ones) and applying an asymptotic analysis, the equations can be approximated and simplified and can still describe the physical phenomena at a high accuracy.

The first step is to neglect the Eulerian perturbation in the gravitational potential (Φ') and its derivative ($\mathrm{d}\Phi'/\mathrm{d}r$). The argument behind this assumption is that if n and ℓ are large, then the gravitational potential perturbation is small in comparison to the density perturbation. The system is then reduced to

$$\frac{\mathrm{d}\xi_r}{\mathrm{d}r} = -\left(\frac{2}{r} + \frac{1}{\Gamma_1 p_0}\frac{\mathrm{d}p_0}{\mathrm{d}r}\right)\xi_r + \frac{1}{\rho_0 c^2}\left(\frac{S_\ell^2}{\omega^2} - 1\right)p', \tag{2.33}$$

$$\frac{\mathrm{d}p'}{\mathrm{d}r} = \rho_0(\omega^2 - N^2)\xi_r + \frac{1}{\Gamma_1 p_0}\frac{\mathrm{d}p_0}{\mathrm{d}r}p'. \tag{2.34}$$

Furthermore, since the eigenfunctions vary more rapidly than the equilibrium quantities when at high

radial order, we can neglect the derivatives of such quantities. Thus $\mathrm{d}p_0/\mathrm{d}r$ is dropped. Additionally, one can also drop the first term of Equation (2.33) ($-2\xi_r/r$) since high radial order modes penetrate less. This leaves us with

$$\frac{\mathrm{d}\xi_r}{\mathrm{d}r} = \frac{1}{\rho_0 c^2}\left(\frac{S_\ell^2}{\omega^2} - 1\right) p', \tag{2.35}$$

$$\frac{\mathrm{d}p'}{\mathrm{d}r} = \rho_0(\omega^2 - N^2)\xi_r, \tag{2.36}$$

which, by direct substitution, leads to

$$\frac{\mathrm{d}^2\xi_r}{\mathrm{d}r^2} + \frac{\omega^2}{c^2}\left(1 - \frac{S_\ell^2}{\omega^2}\right)\left(1 - \frac{N^2}{\omega^2}\right)\xi_r = 0 \implies \frac{\mathrm{d}^2\xi_r}{\mathrm{d}r^2} + K^2\xi_r = 0. \tag{2.37}$$

It is easily seen that the regime of oscillations will depend on the sign of K^2. If $K^2 > 0$ the solutions are oscillatory, while in the reverse case they are exponential. Turning points are expected at the radii where $K^2 = 0$. The sign of this quantity is heavily dependent on the Lamb and Brunt-Väisälä frequencies, S_ℓ and N, respectively. If ω is simultaneously larger or smaller than both characteristic frequencies we get the oscillatory case, whereas if ω is in-between S_ℓ and N we are in the damping case. The turning points (the radii where $\omega = S_\ell$ or $\omega = N$) define propagation regions inside the star which are related to the nature of the mode. As seen before, S_ℓ is related to the acoustic regime, whilst N relates to buoyancy (and thus gravity). In fact, stellar oscillations are standing waves driven by restoring pressure and/or gravity forces. Acoustic modes, or pressure modes (p-modes), are excited by pressure and, on the contrary, gravity modes (g-modes) appear through buoyancy. The p-mode and g-mode propagation regions are schematised in Figure 2.2, for a $1\ \mathrm{M}_\odot$ and $7\ \mathrm{R}_\odot$ model. Understandably, the black curve that delimits the blue g-mode region is the line for $\omega = N$ while the dashed (dot-dashed) line that bounds the orange p-mode region is obtained for $\omega = S_1$ ($\omega = S_2$). It is also visible that for certain values of frequency we could have mixed modes. These are modes that have both p and g character, depending on the region of the star. An example of that are the modes within the red band shown in the figure, which showcase a p-mode behaviour in the convective envelope and g-mode behaviour in the stellar interior. Pressure modes are trapped between the surface and the turning point (where $\omega = S_\ell$) where they reflect.

2.3 Asteroseismology of subgiant stars and relevant diagnostics

In this thesis, we want to study the impact of ADM on KIC 8228742 which is expected to be felt in terms of structural changes and to be more intense in the inner regions of the star. The fact that the character of the modes is intertwined with the region they propagate in is a great starting point for stellar

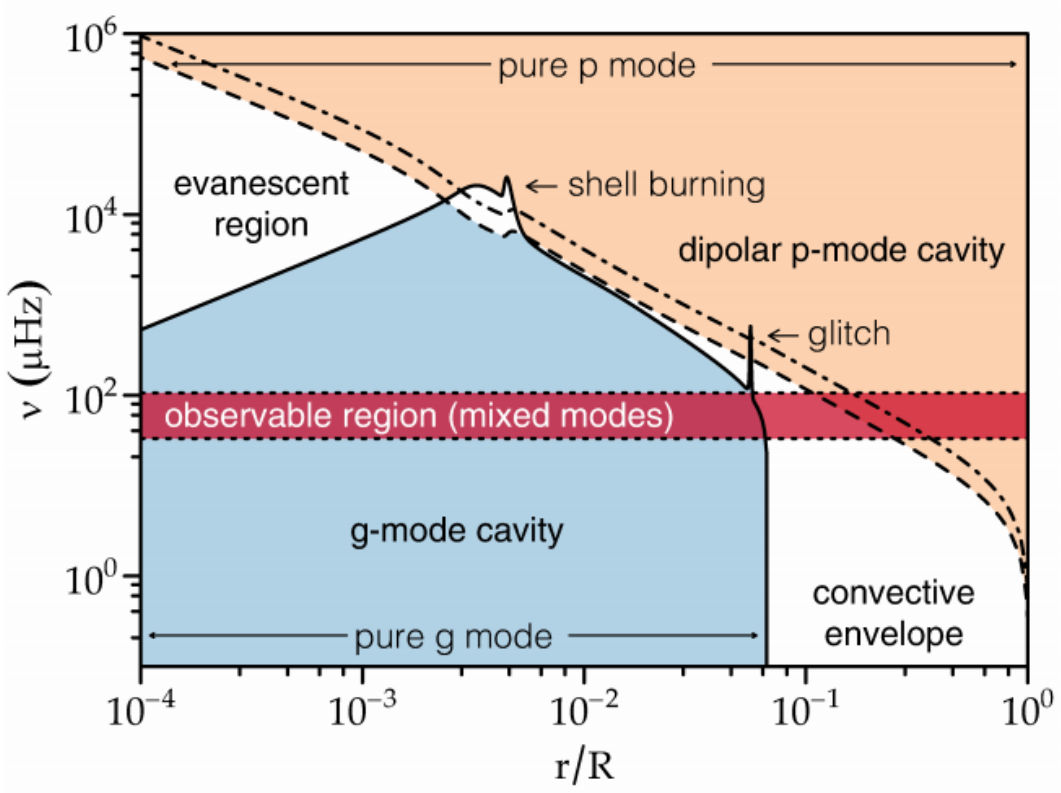

Figure 2.2: Representation of the p and g mode propagation cavities of a red giant star ($1\ \mathrm{M}_\odot$ and $7\ \mathrm{R}_\odot$) taken from Christensen-Dalsgaard *et al.* [73].

probing techniques. Naturally, one can study different depths of the star by analysing the most suitable modes for that task. Additionally, one can define specific diagnostics that enhance the sensitivity in the required regions.

The observational data coming from the already mentioned missions (CoRoT, *Kepler*, TESS, etc.) is often treated through spectrum analysis, with the use of Fourier transforms. This allows one to directly obtain the oscillation frequencies ($\nu_{n,\ell}$) and their associated quantities. For instance, the frequency of maximum power (ν_{max}) is naturally the highest peak in the spectrum. It is specially useful as it obeys the scaling relation [74]

$$\nu_{\mathrm{max}} = \frac{M_{\mathrm{star}}}{M_\odot}\left(\frac{R_\odot}{R_{\mathrm{star}}}\right)^2\left(\frac{T_\odot}{T_{\mathrm{eff}}}\right)^{1/2}\nu_{\mathrm{max}\odot} \tag{2.38}$$

and can, thus, bring insights into some of the fundamental parameters of a star.

Despite the experimental advances made by the aforementioned missions, SG stars are more difficult to find than MS or giant stars since that stage has a relatively shorter lifetime. Another interesting aspect when studying the asteroseismology of SG stars is the lack of detected non-radial acoustic modes ($\ell > 0$). Usually, SG and RGs' most visible oscillations are gravity-dominated mixed modes [75, 76]: due

to the rapid core contraction, the g and acoustic p mode trapping cavities are closer to each other when the stars move off the MS, which results in the coupling of the acoustic and gravity modes. These are the already mentioned mixed modes, which have p-mode characteristics in the convective stellar envelope and g-mode characteristics in the dense radiative stellar core. However, our star, KIC 8228742, exhibits many simple modes (or pure acoustic p-modes) like the sun [77]. This is due to gravity-dominated mixed modes having lower amplitudes than pressure-dominated ones [78,79], so observing them is not always easy. As such, we will first direct our focus to the acoustic simple modes.

Since acoustic waves of low ℓ propagate throughout the entire star, their frequencies encode information of the stellar structure, spanning from the star's core to its surface. Thus, as stated before, obtaining them is pivotal to understand the underlying physics of the internal structure of a star. Naturally, other quantities besides $\nu_{\max}$ can be derived from these frequencies to better probe the stellar structure. The frequencies of acoustic modes with $\ell \ll n$ can be obtained by expanding with the asymptotic approach, yielding [80]

$$\nu_{n,\ell} = \Delta\nu(n + \ell/2 + \varepsilon) - \frac{\Delta\nu^2}{\nu_{n,\ell}} \left[\alpha(\ell(\ell+1)) - \beta\right], \tag{2.39}$$

where ε, α and β are small parameters and the large frequency separation $\Delta\nu = \langle\Delta\nu_{n,l}\rangle$ is defined with the help of (e.g., [80,81])

$$\Delta\nu_{n,\ell} = \nu_{n,\ell} - \nu_{n-1,\ell} \simeq \langle\Delta\nu_{n,l}\rangle = \left(2\int_0^R \frac{\mathrm{d}r}{c(r)}\right)^{-1}, \tag{2.40}$$

where R is the total radius of the star and $c(r)$ represents the sound speed profile inside the star. Thus, $\Delta\nu_{n,\ell}$ is deeply related to the sound speed profile of a star and is useful as a global measure of that quantity [82]. From its definition in Equation (2.40) one can see that it can be directly obtained from the usual spectrum analysis, since it is the difference between peaks with consecutive n and same ℓ.

Additionally, from the noticeable $n+\ell/2$ degeneracy in Equation (2.39), a small frequency separation can also be defined by [80,81]:

$$\delta\nu_{n,\ell} = \nu_{n,\ell} - \nu_{n-1,\ell+2} \simeq -(4\ell+6)\frac{\Delta\nu}{4\pi^2\nu_{n,\ell}}\int_0^R \frac{\mathrm{d}c}{\mathrm{d}r}\frac{\mathrm{d}r}{r}, \tag{2.41}$$

which is particularly sensitive to the thermodynamic conditions of the stellar core.

From this, Roxburgh & Vorontsov [83] defined the useful small to large separation ratio,

$$r_{02}(n) = \frac{\delta\nu_{n,0}}{\Delta\nu_{n,1}} = \frac{\nu_{n,0} - \nu_{n-1,2}}{\nu_{n,1} - \nu_{n-1,1}}. \tag{2.42}$$

This ratio is particularly interesting for this work since in stars other than the Sun it is difficult to

observe modes with $\ell > 2$ due to partial cancellation (e.g., [70]). Furthermore, it aims to give better insights on the stellar core, where the most significant DM influence is expected, since the near-surface effects that highly affect individual frequency separations nearly cancel by applying this ratio. This means that $r_{02}(n)$ is independent of the structure of the outer layers of a star and thus works as a probe into the stellar interior [83].

As discussed before, SG and RG stars often exhibit gravity dominated modes. From these, the period separation $\Delta\Pi_\ell$ is a useful quantity to extract, since g-modes are uniformly separated in period. In the asymptotic limit, it is given by [80]

$$\Delta\Pi_\ell = \frac{2\pi^2}{\sqrt{\ell(\ell+1)}} \left(\int_{r_1}^{r_2} N \frac{dr}{r} \right)^{-1} = \frac{\Pi_0}{\sqrt{\ell(\ell+1)}}, \tag{2.43}$$

where r_1 and r_2 correspond to the lower and upper boundaries of the g-mode cavity, respectively, which extends through the radiative region of the star. Since, in SG stars, r_1 coincides with the interface between the inner convective zone (if there is one) and the radiative region, it follows that $\Delta\Pi_\ell$ directly relates to the size of the convective core.

The link between these diagnostics and the effects of ADM in our star will be clearer with the next chapter, where we discuss the asymmetric dark matter interactions with a stellar body.

3

Asymmetric Dark Matter interactions with a star

Contents

The previously mentioned asteroseismic diagnostics are relevant since it is our goal to infer on the impact ADM particles have in stars and then draw conclusions from it. This is because that impact is expected to be felt structurally, more significantly in the stellar core. We now have the means to probe that impact but it is pivotal to know what produced it. Thus, a detailed description of the interactions between these particles and stellar matter is crucial. By modifying evolution codes, like the already mentioned MESA, we can build stellar models that include these phenomena and that enable the comparison between models with and without DM along with observations.

This chapter contains the description of the main DM processes happening with and within stars, like capture and energy transport, and closes with a contextualisation of those phenomena in stellar evolution codes.

3.1 Accumulation of DM particles in a star

By virtue of being massive, particles in the dark matter halo can be attracted by a star. If they become gravitationally bound to it then they are considered successfully captured and will contribute to the buildup of large concentrations of particles within the centre of the star. The capture process is the main driver of the accumulation of DM particles in stars. Besides that, one has to account for processes that decrease the number of trapped particles. The most relevant of these are the self-annihilation and evaporation. The expression that regulates the number of trapped DM particles N_χ is then

$$\frac{\mathrm{d}N_\chi}{\mathrm{d}t} = C - EN_\chi - AN_\chi^2, \tag{3.1}$$

where C is the capture rate due to the scattering of DM particles off nucleons, E is the evaporation rate and A the self-annihilation rate (annihilation cross section times the relative DM velocity per unit volume). However, Equation (3.1) is only valid in a framework of self-conjugate DM (the historical concept of WIMPs, see Section 1.1) and, in our ADM scenario, self-annihilation is negligible. Furthermore, evaporation—the inverse process of capture in which DM particles that were already trapped inside the star scatter to velocities larger than the local escape velocity— can also be safely neglected since it has been found that, for sun-like stars, the DM mass above which evaporation is negligible is close to 3.3 GeV (e.g., [32, 33]), and in this work we explore larger mass values of ADM particles ($m_\chi \geqslant 4$).

Then, in our ADM case, these assumptions reduce Equation (3.1) to

$$\frac{\mathrm{d}N_\chi}{\mathrm{d}t} = C. \tag{3.2}$$

As stated before, the process of capture consists in the gravitational trapping of DM particles from the galactic halo by losing enough kinetic energy when scattering off stellar matter. It is then mainly defined

by the DM mass (m_χ), the DM–nucleon cross-section ($\sigma_{\chi n}$), the gravitational potential of the star (ϕ) and the local DM density (ρ_χ). In our case, KIC 8228742 is just 0.17 kpc away from the Sun, therefore we assume a local DM density corresponding to what is found in the solar neighbourhood, $\rho_\chi = 0.38$ GeV/cm^3 [84]. The capture rate formalism adopted in this work is the one derived by Gould [85] and it is fairly complex in its standard form. A simplified form, which helps giving clearer insight into the process, was given by Zentner [86] for DM capture in the Sun,

$$C_n \simeq \sqrt{\frac{3}{2}} \frac{\rho_\chi}{m_\chi} \sigma_{\chi n} v_{\rm esc}(\mathrm{R}_\odot) \frac{v_{\rm esc}(\mathrm{R}_\odot)}{\overline{v}} f_n \frac{\mathrm{M}_\odot}{m_n} \langle \hat{\phi}_n \rangle \frac{\mathrm{erf}(\eta)}{\eta}, \tag{3.3}$$

where C_n is the capture rate calculated for the nuclear species n ($C = \sum_n C_n$), $v_{\rm esc}(\mathrm{R}_\odot)$ is the escape speed from the surface of the star, $\overline{v}$ is the local three-dimensional velocity dispersion of DM particles in the halo, f_n is the fraction of the solar mass in nucleus n such that $f_n \frac{\mathrm{M}_\odot}{m_n}$ is the number of that nuclei, $\langle \hat{\phi}_n \rangle$ is the average (dimensionless) potential experienced by those nuclei and, finally, η is a dimensionless speed that defines the Sun's movement through the galactic halo: $\eta = \sqrt{3/2} v_\odot / \overline{v}$, with $v_\odot$ being the speed of the star relative to the DM halo. By examining Equation (3.3), one sees that overall the capture rate scales as $C \propto m_\chi^{-1}$. This is coherent because heavier DM particles are expected to require more interactions to slow their speed down to less than the escape velocity.

One interesting factor is the treatment of the DM-nucleon cross-section. In most model-independent DM studies it is usual to assume the already mentioned spin-independent $\sigma_{\rm SI}$ and spin-dependent $\sigma_{\rm SD}$ effective constant cross sections to describe the ADM particles' interactions with the baryons in the stellar plasma. However, in this work we are mainly interested in spin-dependent scatterings, effectively setting $\sigma_{\rm SD} \gg \sigma_{\rm SI} \to 0$. This, in the case of solar-like stars, essentially means that the relevant nuclear species for scattering with DM particles are mostly reduced to hydrogen.

3.2 Energy transport via ADM interactions with stellar matter

After accumulating and thermalising within the star, captured DM particles interact with baryons in the stellar interior. In scatterings such as these, energy is naturally transferred from one particle to the other. Since both the baryonic density and temperature are higher in the inner regions of the star, the nucleons there have higher energy than the ones inhabiting the outer regions. Consequently, DM particles are expected to, on average, gain energy upon colliding with nucleons in the inner layers of the star and lose energy after scattering off nucleons in the outer regions. Additionally, as a result of the high density of both DM and baryonic matter, there are also more DM-baryon interactions in central regions. As such, these phenomena create an additional mechanism for transporting energy from the core outwards, adding an extra term to the standard equation of energy transport in stars, already

discussed in Section 2.1. It is expected that the inclusion of this process creates substantial differences in the structure and evolution of a star.

The formalism used to define the additional energy transport term depends on the regime of the Knudsen number K. In this case,

$$K \equiv \frac{\ell_{\chi,0}}{r_\chi}, \tag{3.4}$$

where $\ell_{\chi,0}$ denotes the mean-free-path of an ADM particle in the centre of the star and r_χ is the typical scale radius of the ADM distribution in the stellar core,

$$r_\chi = \frac{3}{2\sqrt{\pi}} \left(\frac{k_B T_c}{G \rho_c m_\chi} \right)^{1/2} \tag{3.5}$$

with index c referring to a core quantity.

In a limit where $K \to 0$, the energy transfer is local since the ADM particles travel short distances before interacting again. In this regime, particles are in local thermodynamic equilibrium and, by determining their number density it is possible to compute the energy transported by ADM particles [87, 88],

$$l_{K\to 0}(r) = 4\pi r^2 \kappa(r) n_\chi(r) \ell_{\chi,r} \left(\frac{k_B T(r)}{m_\chi c^2} \right)^{1/2} k_B \frac{\mathrm{d}T}{\mathrm{d}r}, \tag{3.6}$$

where $\kappa(r)$ is a dimensionless thermal conductivity, $n_\chi(r)$ is the number density of ADM particles at radius r and the time dependence is dropped but is implicit in all quantities.

However, in the so-called Knudsen limit where $K \gg 1$, particles orbit the stellar core many times between interactions with the plasma. Therefore, their mean-free-path is large when compared with the typical dimensions of the system (r_χ). In this regime, energy transfer is non-local and ADM particles have an isothermal (Boltzmann) distribution, rendering the treatment of the energy transport term in this limit highly non-trivial. An analytical approximation was first obtained by Spergel & Press [89] and Gould & Raffelt [90] followed that endeavour by numerically replicating the results by essentially modifying the ADM luminosity in the limit $K \to 0$ with a multiplicative suppressing factor, which naturally depends on K,

$$l_\chi \propto \mathcal{S}(K) l_{K\to 0}. \tag{3.7}$$

The energy balance of the star will then have an additional term of the form

$$\varepsilon_\chi = \frac{\partial l_\chi}{\partial m}, \tag{3.8}$$

which is negative where energy is carried from the sphere of mass m outwards and positive where

DM particles lose (and thus deposit) energy by interacting with less energetic stellar matter. The term in Equation (3.8) is then to be included in Equation (2.4).

As a matter of fact, the mean-free-path of an ADM particle in a common MS star is several times larger than the typical dimensions of the system and so, the Knudsen limit applies. In this work, we chose this direction since a large K was also observed.

3.3 Stellar models with DM contribution: previous findings and integration within MESA

In the preceding section we discussed the fact that ADM interactions introduce a new energy transport mechanism. This indicates that it is possible that ADM presence in stars impacts their structure and evolution. Previous studies regarding the impact of ADM in the Sun showed that due to the flux of energy carried outwards from the innermost regions of the star by ADM particles with a mass of $7\ \mathrm{GeV}$ and $\sigma_{\mathrm{SD}} \simeq 10^{-36}\ \mathrm{cm}^2$, the stellar core exhibited a decrease in temperature when compared to the standard (non-DM) case, while the reverse happened with the (baryonic) density [34] (see Figure 3.1). This effect, whose intensity is naturally related to the interaction cross-section, is in fact counter-intuitive given that any transport of energy away from the core should lead to its contraction, which would in turn lead to an increase in temperature. This however is not the case, since the energy transported away by the ADM particles is of a higher order of magnitude than the one released by the core contraction, countering its heating effects.

Another well-known consequence of the extra energy transport by DM is the suppression of convection – generally in the centre of the star – which was firstly proposed by Renzini [91] and Bouquet & Salati [92] and later studied by Casanellas & Lopes [36] and Casanellas *et al.* [93], particularly for stars with masses between 1.1 and 1.3 $\mathrm{M}_{\odot}$. This suppression is directly related to the decrease in the temperature gradient, which prevents the arise of convection as it would in cases where there is no energy transport by DM.

In this work, to study the effects of the interactions between ADM and the stellar plasma during the evolution of star KIC 8228742 we use the new modifications to the MESA stellar evolution code presented by Lopes [37, 94]. These include the processes described before, namely capture and energy transport. We consider DM Capture as described by Gould [85], and the energy transport is computed taking into account the numerical results by Gould & Raffelt [90]. During the stellar evolution, the capture rate is computed at each time step, and the total number of ADM particles inside the star is updated accordingly. This information is then used to compute the extra energy term, which is fed to the usual set of differential equations that govern stellar evolution, already defined in MESA. The detailed process of the stellar modelling carried out throughout this work will be given in the next chapter.

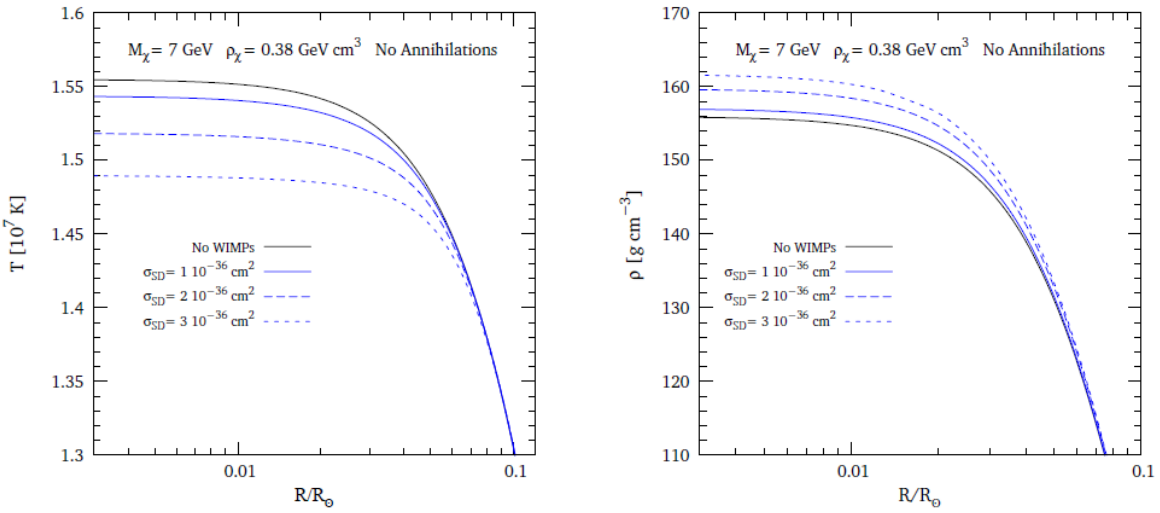

Figure 3.1: Impact of ADM energy transfer on the temperature and baryonic density profiles of the Sun, for different σ_{SD}, taken from Taoso *et al.* [34].

4

High precision calibration and diagnostics of stars

Contents

As our work focuses on finding ways to constrain ADM properties through asteroseismic analysis, comparing observational data with model data is pivotal to, e.g., better probe the DM parameter space (m_χ, σ_{SD}). Furthermore, obtaining stellar models that match the observed star is obviously crucial to validate our conclusions. Therefore, a great portion of this thesis is focused on building and analysing relevant stellar models for our problem.

Stellar modelling has been extremely helpful in allowing us to better understand the physics at play inside stars. The already mentioned Modules for Experiments in Stellar Astrophysics (MESA) [64–68], an open-source 1-D stellar evolution code, is a powerful tool in this regard. Combining various modules that aim to precisely describe different stellar phenomenology, MESA allows the user to model a wide variety of stars, given a set of stellar parameters as inputs. By virtue of being a robust open-source and community-driven stellar evolution code, MESA is widely used in the astrophysical scientific community. Our work uses MESA extensively and, as seen before, even exploits different modifications and additions to it that treat the DM phenomena.

In this chapter, a more detailed view on the methodology used throughout this work to obtain the results appearing in following chapters is given.

4.1 Process of star selection

As presented in Chapter 1 and Section 3.3, the use of stars, namely the Sun, to study DM properties is nothing new. In fact, the Sun proves to be a valuable DM laboratory since our understanding of it is much more refined than that of any other star. However, our intent with this work is not only to advance the techniques of building exclusion diagrams for DM parameters through the use of seismic diagnostics but also to explore the impact of ADM in a different set of stellar data. With that in mind, we decided to perform this study on a SG star for the first time.

We chose to focus on the *Kepler* mission catalogue [58, 59] since it offers precise asteroseismic measurements. Appourchaux *et al.* [77] determined the oscillation mode frequencies for a *Kepler* subset of 61 MS and SG stars and, thus, that constitutes our candidate set.

To be considered a good candidate for this study a star ought to have enough observed individual oscillation modes and good estimations for its fundamental properties (luminosity, effective temperature, etc.). Moreover, a star that has been modelled before grants the opportunity to compare our models and infer on their perceived quality. All these arguments pointed our choice towards KIC 8228742, a F9IV-V spectral type star [95] with a previously modelled mass of $\sim$1.27 $M_\odot$ [96] and 32 detected individual oscillation modes [77].

4.2 Observables and Calibration

Modelling the SG star KIC 8228742 comes down to a calibration procedure which aims to find the optimal input parameters that produce the closest outputs to the observed quantities of this star. This constitutes an optimisation problem which, in the case of MESA, is handled by the *astero* module [65].

Using this module as a starting point, we produce a high precision stellar model calibration process which allows for both seismic and spectroscopic calibrations by taking as inputs $\{M,\ Y_i,\ [\mathrm{Fe/H}]_i,\ \alpha,\ f_{\mathrm{ov}}\}$ (stellar mass, initial helium abundance, initial metallicity, mixing-length parameter and overshooting parameter, respectively) and then producing an evolutionary model from pre-MS to current-day which is compared head-to-head with observations. This comparison is accomplished by computing a χ^2_{star} value at every step of the simulation that has weighted contributions from both spectroscopic (χ^2_{spec}) and seismic (χ^2_{seis}) observables. In this work we use the default 2/3 weight on the seismic contribution and 1/3 on the spectroscopic counterpart, i.e., $\chi^2_{\mathrm{star}} = 1/3\chi^2_{\mathrm{spec}} + 2/3\chi^2_{\mathrm{seis}}$ [65, 97]. The diagnostics χ^2_{spec} and χ^2_{seis} are quadratic deviations from the spectroscopic and seismic observational data, respectively, with their uncertainties taken into account:

$$\chi^2_{\mathrm{spec/seis}} = \frac{1}{N}\sum_{i=1}^{N}\left(\frac{X_i^{\mathrm{mod}} - X_i^{\mathrm{obs}}}{\sigma_{X_i}}\right)^2, \tag{4.1}$$

where N is the number of parameters, X_i^{mod} and X_i^{obs} are the stellar model and observed values of the i^{th} parameter, respectively, with σ_{X_i} being the observational uncertainty. Throughout this work, the observational constraints for KIC 8228742 are taken from Chaplin *et al.* [98] for the spectroscopic parameters and from Appourchaux *et al.* [77] for the oscillation frequencies, as published in the Asteroseismic Modelling Portal (AMP) [99]. From these, the observational parameters used in χ^2_{spec} are $\{L, T_{\mathrm{eff}}, [\mathrm{Fe/H}]\}$ = $\{4.57 \pm 1.45\ \mathrm{L}_\odot,\ 6042 \pm 84\ \mathrm{K},\ \text{-}0.14 \pm 0.09\}$ (luminosity, effective temperature and metallicity), and in χ^2_{seis} is $\{\Delta\nu\}$ = $\{62.1 \pm 0.13\ \mu\mathrm{Hz}\}$. Additionally, to calculate $[\mathrm{Fe/H}]$ through $[\mathrm{Fe/H}] = \log[(\mathrm{Z/X})/(\mathrm{Z/X})_\odot]$ we use the solar value of $(\mathrm{Z/X})_\odot = 0.02293$ computed by Bahcall *et al.* [100] based on the composition from Grevesse & Sauval [101].

As for the calibration procedure, we use a method that is commonly used throughout the literature (e.g., [43, 102]) which relies on minimising χ^2_{star}. This is achieved through an automatised optimisation process which uses a direct search method —the downhill simplex algorithm [103]— to find the optimal set of inputs that produce the group of outputs $\{L, T_{\mathrm{eff}}, [\mathrm{Fe/H}], \Delta\nu\}$ that are closest to their observed counterparts. When accounting for DM effects by using the new code mentioned in Section 3.3, we can also take advantage of the optimisation algorithm to find optimal values for DM parameters. To do that, we extend the standard calibration process to also include the relevant DM parameters as inputs, which extends the input set to $\{M,\ Y_i,\ [\mathrm{Fe/H}]_i,\ \alpha,\ f_{\mathrm{ov}},\ m_\chi,\ \sigma_{\mathrm{SD}}\}$ while maintaining the same outputs and comparison strategy. This is possible because the *astero* module allows the user to define

custom parameters that can behave as inputs to the stellar simulation and therefore are included in the optimisation process. Then, the variables from the DM code mentioned in Section 3.3 can be connected to that mechanism via the adequate *Fortran* scripts. A few additional changes were also made to the base code of the DM package as to minimise computation time without the loss of accuracy. Namely, we skip the calculation of the capture rate when the two previous steps exhibit similar capture rates (within a user defined ε).

More specifically, in a single MESA simulation, the *astero* module is called each step to produce the $\chi^2_{\rm star}$ values from the parameters coming from the MESA model at that step. This is done until the simulation reaches its designated end – if the user set a terminal age – or the $\chi^2_{\rm star}$ values explode. The best value from that run (i.e., the smallest $\chi^2_{\rm star}$) is then recorded and the respective model is taken as the best for that set of input parameters. In our case, since we choose to use one of the module's optimisation algorithms, *astero* will automatically start a new simulation with different input parameters, so as to find the set that minimises $\chi^2_{\rm star}$, and the whole process is identical. After the designated number of optimisation steps or the stagnation of the $\chi^2_{\rm star}$ values, one can conclude that the algorithm has converged. All the values are then recorded in an ordered $\chi^2_{\rm star}$ table with the respective model input and output parameters that produced them.

4.3 Seismic ratio diagnostics

While ensuring that a model is consistent with observations in terms of spectroscopy is valuable in itself, in most cases these parameters do not fully mirror what is happening in the stellar interior. These are the situations where thoroughly analysing the oscillation frequencies of a star becomes a powerful diagnostic tool.

To build upon the calibration process described in the last section, we resort to a more detailed seismic diagnostic of the stellar interior based on the observed and model frequencies $\nu_{n,\ell}$. The oscillation frequencies and respective eigenfunctions of a stellar model are obtained using the GYRE code [104, 105]. This is a robust pulsation code that computes the oscillations in both adiabatic and non-adiabatic regimes. In our case, the code was used to solve the system of linear adiabatic oscillations under the Cowling approximation [72], given by Equations (2.33) and (2.34).

Following the arguments presented in Chapters 2 and 3, the small to large separation ratio r_{02} defined in Equation (2.42) is chosen as a diagnostic to better probe the region that ADM is expected to impact more severely: the stellar core. Conveniently, we define a new χ^2 to assess the seismic quality of a given stellar model in terms of the r_{02} ratio:

$$\chi^2_{r_{02}} = \sum_{n=14}^{22} \left[\frac{r_{02}^{\rm obs}(n) - r_{02}^{\rm model}(n)}{\sigma_{r_{02}^{\rm obs}}} \right]^2 , \tag{4.2}$$

where $r_{02}^{\text{obs}}(n)$ and $r_{02}^{\text{model}}(n)$ represent the ratio defined in eq. (2.42) computed using both the observed and model frequencies, respectively, while $\sigma_{r_{02}^{\text{obs}}}$ stands for the observed uncertainty which is computed through error propagation from the individual frequencies' uncertainties. For the star considered here, we can observe 32 modes with $\ell \leqslant 2$ [77] and n running from 14 to 22, amounting to 9 different instances of r_{02} in the sum defined in eq. (4.2). The resulting value of $\chi^2_{r_{02}}$ along side the other mentioned diagnostics will provide the classification of the models.

One important point to bear in mind is that $\chi^2_{r_{02}}$ is used as an additional diagnostic, independent from the original calibration process. This is mainly because it creates a robust two-step rejection method and also due to computational time constraints. Thus, only χ^2_{spec} and χ^2_{seis} are computed at each step of the calibration process. It should be noted that while χ^2_{seis} does imply the computation of the large frequency separation, this is accomplished by taking into account the asymptotic approximation in eq. (2.40) instead of the actual computation of the oscillation modes, and as such, it does not represent the time-consuming effort that r_{02} would. After the calibration process presented in the previous section is completed, the r_{02} ratios are computed for the accepted models of that step (usually by defining a cut-off χ^2_{star}).

5

Stellar Models: Impact of ADM on a subgiant star

Contents

Having set the building blocks, we focus on the end goals of this work. If existent, asymmetric dark matter clusters together in the inner regions of stars, producing distinct signatures. The first step towards building a reliable method of ADM parameter exclusion is probing this impact and comparing it with present day observations.

In this chapter, we present the first results of this work. We calibrate the SG star KIC 8228742 using the methods described in the previous chapter firstly assuming no ADM influence and then applying the effects described in chapter 3. Comparisons and conclusions are made regarding the quality of no-DM and DM models, while the impact of ADM in the star is also discussed.

5.1 Standard stellar model of the subgiant KIC 8228742

We start by calibrating a standard stellar model of the star that will serve both as a comparative and as a backbone model. Thus, using the calibration methods described in Chapter 4 with all five inputs $\{M$, Y_i, [Fe/H]$_i$, α, $f_{\rm ov}\}$ as free parameters, we obtain several stellar models with no dark matter interactions. These are obtained in the optimisation procedure that aims to minimise $\chi^2_{\rm star}$ and the whole process is stopped only when that diagnostic stagnates or starts to deteriorate. After that, from these models, the best one in terms of $\chi^2_{\rm star}$ is chosen as the benchmark model for future analysis and is henceforth also referred to as Standard Subgiant (SSG) model. The resulting parameters are shown in the first row of Table 5.1, where $\chi^2_{r_{02}}$ is also included. It should be noted that directly comparing $\chi^2_{\rm star}$ with $\chi^2_{r_{02}}$ is misleading, as their definitions and normalisation are different.

In comparison with other models found in the literature, the SSG model's parameters fall well within the limits proposed in most works (e.g., [106]) with the exception of the initial metallicity and mixing-length parameters found in Verma *et al.* [107], which had an initial parameter range that did not include the values of [Fe/H]$_i$ and α displayed in Table 5.1. However, this does not amount to a large discrepancy and thus the model is accepted to be a good reference model. Additionally, the SSG model exhibits a convective core during the MS that extends up to $0.065\mathrm{R}_\odot$ (0.035 of the total radius $\mathrm{R} \approx 1.88$) and showcases a helium core (surrounded by a hydrogen shell) at the end of the evolution (see fig. 5.3), which is the expected structure for stars in this stage of evolution, with these values of stellar mass (e.g., [108–111]).

5.2 Comparison of dark matter models with a standard stellar model

A valuable asset of the improved calibration method considered in this work is that it allows for the DM properties to be treated as free parameters in the calibration. In this sense, we allow the algorithm to vary the values of the ADM particles' mass in between 4 and 12 GeV and the spin-dependent cross

Model	m_χ (GeV)	$\sigma_{\rm SD}$ (10^{-36} cm^2)	M ($M_\odot$)	Y_i	$[{\rm Fe/H}]_i$	α	$f_{\rm ov}$ (10^{-36})	age (Gyrs)	L ($L_\odot$)	R ($R_\odot$)	$\log\left(\frac{T_c}{1\ {\rm K}}\right)$	$\log\left(\frac{\rho_c}{1\ {\rm gcm^{-3}}}\right)$	$\chi^2_{\rm star}$ (10^{-3})	$\chi^2_{r_{02}}$	$\Delta\Pi_1$ (s)	$\Delta\Pi_2$ (s)
SSG	-	-	1.2565	0.244	-0.139	1.403	1.622	4.52	4.254	1.884	7.42	2.53	5.735	27.8	1636	945
DM Calib	9.12	2.32	1.2517	0.227	-0.140	1.467	1.626	5.03	4.270	1.886	7.32	2.95	5.287	29.2	548	316
DM A	6.00	10^{-3}	1.2580	0.244	-0.140	1.406	1.623	4.50	4.263	1.884	7.42	2.53	5.586	26.7	1642	948
DM B	6.00	10^{-1}	1.2591	0.243	-0.139	1.407	1.622	4.50	4.264	1.885	7.42	2.53	5.486	37.8	1644	949
DM C	5.00[a]	1	1.2516	0.227	-0.138	1.480	1.623	5.06	4.268	1.887	7.32	2.96	5.245	20.0	543	313
DM D	6.00	10	1.2590	0.229	-0.139	1.403	1.622	4.76	4.339	1.884	7.32	2.96	17.879	64.3	564	326

[a] A slightly different mass value was used in this case due to model convergence limitations.

Table 5.1: KIC 8228742 models. The 4 bottom models were calibrated with fixed pairs of (m_χ, $\sigma_{\rm SD}$) while DM Calib allowed the two parameters to vary. The first 2 columns are the DM parameters and the 5 following columns are the input parameters of the calibration. The following columns correspond (from left to right) to: age, luminosity, total radius and the logarithms of the central temperature and central density. The χ^2 used in calibration and diagnostics are also displayed. Finally, the period spacing is shown for $\ell = 1$ and $\ell = 2$.

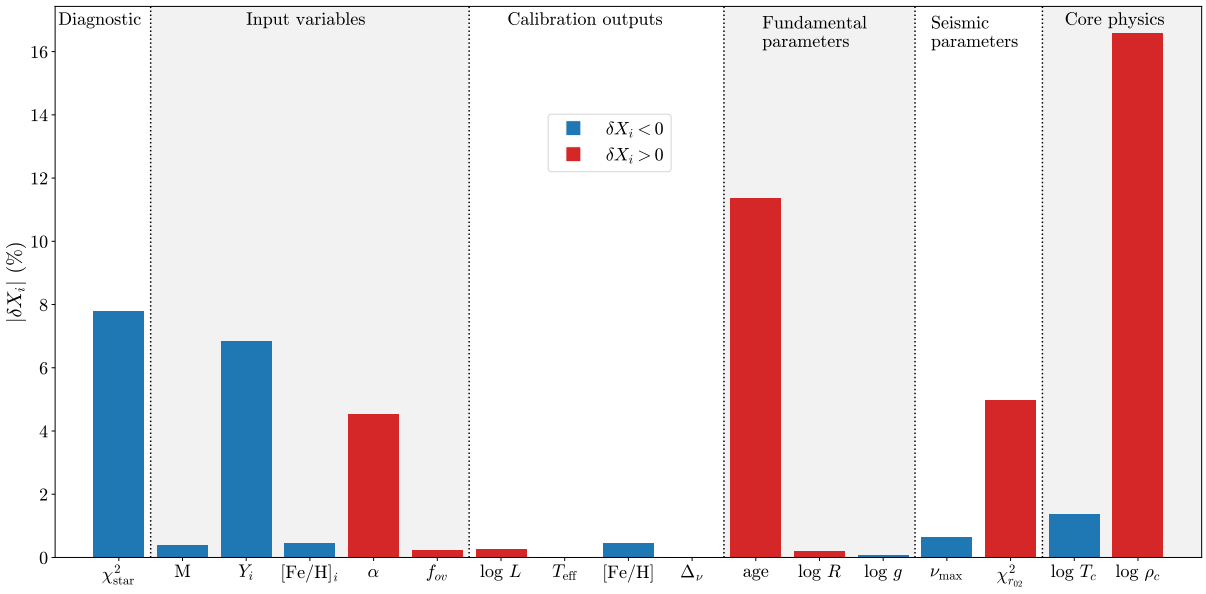

Figure 5.1: Direct comparison of the DM Calib and Standard Subgiant models: the percentage variations were recorded relatively to the SSG model (see Table 5.1). As some variations are negative, we use blue for negative values and red otherwise.

section in between 10^{-40} and 10^{-35} cm^2 since this is both included in the region of the parameter space currently being probed by DM direct detection experiments and also the region that produces greater effects on stars (e.g., [36, 55]).

As before, the standard stellar inputs shown in the last section were treated as free parameters, so it is expected that the set of optimal parameters is different than the values shown in the first row of Table 5.1. Taking into account the DM phenomenology described in Chapter 3, we carried out the optimisation process, from which we retrieved the best model (i.e., with the lowest $\chi^2_{\rm star}$). This model (DM Calib) found an optimal dark matter particle with a mass of $m_\chi = 9.12$ GeV and a spin-dependent interaction cross section of $\sigma_{\rm SD} = 2.32 \times 10^{-36}$ cm^2, which is within the limits of the XENON-100 experiment mentioned in Chapter 1. The fact that this model is calibrated, by definition, means that it is bound to be in agreement with the corresponding observations. However, it is interesting to note that the best agreement – within the considered parameter range – occurs for the aforementioned values of m_χ and $\sigma_{\rm SD}$, even though they fall inside the excluded area of other more recent experiments (e.g., [24]).

As expected, fig. 5.1 shows that the optimal inputs changed with respect to the parameters obtained in the SSG model, some more drastically than others, as is the case of the initial Helium abundance Y_i and the mixing-length parameter α. In terms of model outputs, the inclusion of the DM effects and parameters in the calibration process made the stellar age change in around 12% while the most noticeable difference is the 16% increase in the logarithm of the central density, which translates to a factor

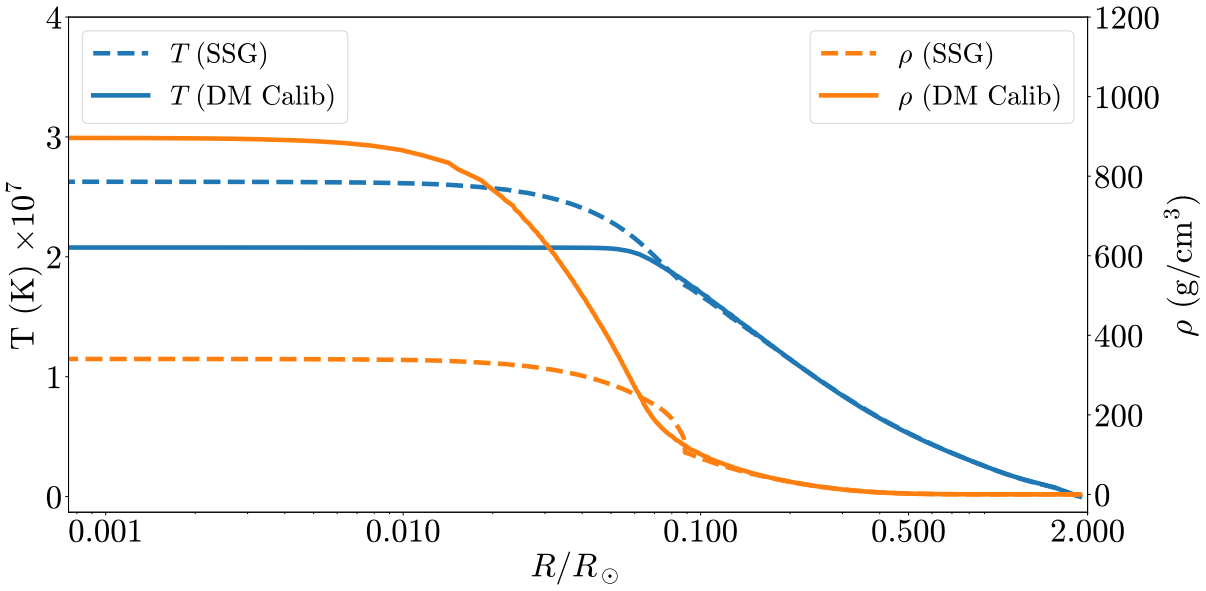

Figure 5.2: Temperature (left axis) and baryonic density (right axis) profiles of the SSG and DM Calib stellar models (see Table 5.1).

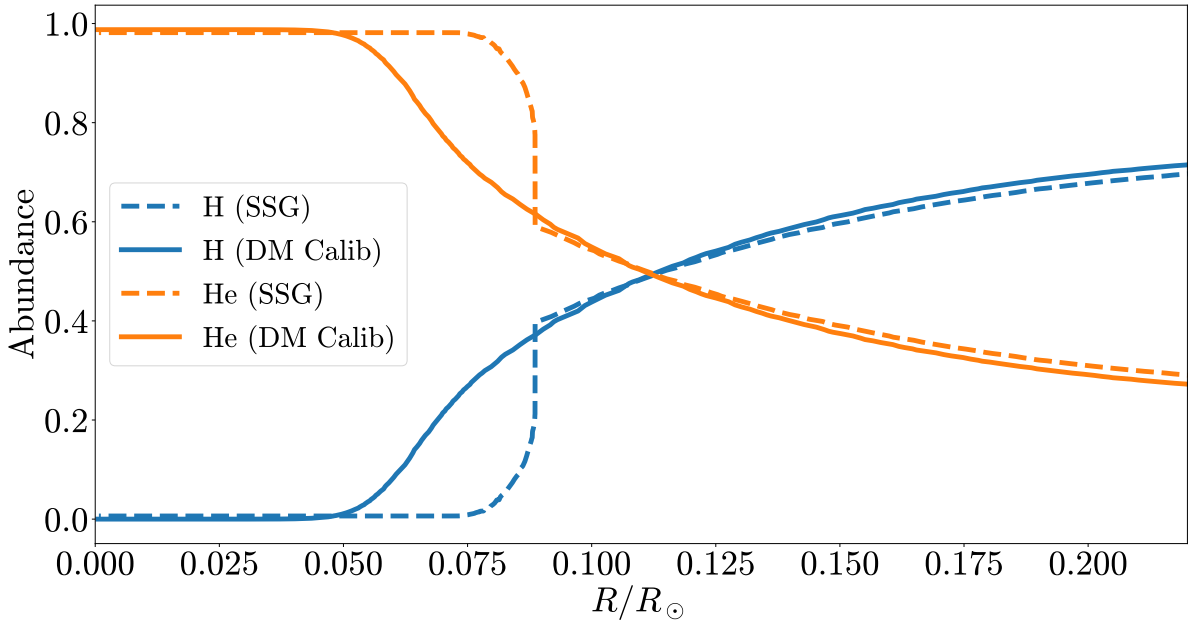

Figure 5.3: Hydrogen and helium abundances of the SSG and DM Calib stellar models (see Table 5.1).

of around 2.5 in the central density itself. This discrepancy is best viewed by comparing the respective profiles shown in fig. 5.2, where it is visible that the star forms an isothermal core at a lower temperature, which is consistent with other results for the Sun and other sun-like stars (e.g., [34, 112]). Such is also the case of the baryonic density profile, which displays an increase in the innermost regions of the star when considering ADM capture and interactions, as shown in Section 3.3. One important aspect to remember is the fact that, by only considering spin-dependent couplings, the DM-stellar matter scatterings are practically reduced to DM-hydrogen interactions. This means that, in fact, we neglect most of the DM energy transport that occurs during the actual SG phase, given that in these stars the region inhabited by ADM particles, i.e., the core, is mostly devoid of hydrogen. Thus, the DM signatures shown here – and the resulting departures from the standard non-DM models – are in fact a consequence of DM interactions that occurred mainly during the MS. Therefore, the comparison with different studies in the literature about similar effects in MS stars is reasonable since we are looking at the remnants of ADM interactions during the MS phase through a SG star. It should also be noted that although we are not comparing both models at the same age (nor do they have the same standard stellar inputs), as is the usual practice, the comparison is still of interest (and thus this effect is still expected) since it is made between two calibrated models of the same star, meaning that they are spectroscopically similar. Nevertheless, one could argue that the change in the star's age could be the driving factor of the differences found between the two models. But, in fact, that is not the case: By analysing the same profiles of the two models for the same age (for example, at t = 4.52 Gyrs, see Table 5.1) we confirm that the two distinct regimes are still present and identical to what is seen in Figures 5.2 and 5.3.

Unlike the Standard model of this star, DM Calib did not exhibit a convective core. In fact, the suppression of the convective core is a recurring feature of DM influence on stars as mentioned in Section 3.3. Furthermore, by studying the star chemical profiles (Figure 5.3) we see that while hydrogen is completely exhausted in the inner regions of the stellar core, there is a smooth increase in the hydrogen abundance (vice-versa for helium), instead of the sharp variation which is usual in stars with $M \simeq 1.3\ M_{\odot}$.

This is a direct consequence of the stellar core being radiative, as opposed to convective, during the main-sequence: the arise of core convection during the MS promotes the homogenisation of the chemical species in the central regions of the star, and thus the exhaustion of hydrogen that characterises the end of the MS occurs everywhere within the convective zone – instead of locally in centre of the star.

One other effect that is found in this model is the extension of the MS lifetime [94]. While the star with DM has a radiative core during the largest part of its MS lifetime, and thus nuclear burning is limited to the local hydrogen supply, the decrease in central temperature slows down the hydrogen burning rate thus extending the MS lifetime. The age of the model itself may be another indicator of this effect since the best agreements with observations (which are the goals of a successful calibration) were found to be at a later stellar age than in the standard case.

In addition to the model DM Calib, we decided to repeat the calibration process accounting for DM effects, but instead with pre-defined fixed values of m_χ and σ_{SD}. Stellar DM models from A to D are the best models for each of the (m_χ, σ_{SD}) pairs showcased in Table 5.1. The first conclusion to be taken is that DM Calib, which produced an optimal pair of (m_χ, σ_{SD}), does not have the lowest χ^2_{star}. This means that the full calibration optimisation method most likely hit a local minimum around the displayed values.

A closer inspection at the remaining columns of Table 5.1 reveals that the SSG model, DM A and DM B all share similar outputs. The same happens for models DM Calib, C and D, where the latter slightly deviates from the rest, leading to a χ^2_{star} of an higher order of magnitude. These two distinct regimes are expected once we take into account the mass and cross-section values of the dark matter impacted models: for $\sigma_{\mathrm{SD}} \geqslant 10^{-36}$ cm^2 the effects from ADM interactions have a noticeable impact on the star, while for smaller values of σ_{SD} the effects are mostly negligible. We also confirm the prevalence of the two regimes when drawing profiles similar to figs. 5.2 and 5.3 for the remaining models, i.e., the curves of Standard, DM A and DM B have similar behaviour between themselves whilst the remaining models follow the signature of DM Calib (see fig. 5.4).

Then, it is expected that the suppression of the convective core, already noticed in DM Calib, is present in the models that have the same behaviour (i.e., DM C and D). Likewise, DM A and B should have a convective core like the SSG. The existence of convective and radiative zones can be confirmed by plotting the Brunt-Väisälä frequency, already defined in Section 2.2.1. The previously mentioned GYRE [104, 105] code allows the direct extraction of N^2 for each model and, applying the same rationale of fig. 2.2, we can conclude from fig. 5.5 that the two classes of models are distinctly separated in the left-hand side of the plot. While the cold-coloured models (SSG, DM A and DM B) exhibit the g-mode cavity (radiative region) starting at ~ 0.035 R (blue vertical line on the left), which is precisely the convective core size stated in Section 5.1, the hot-coloured models (DM Calib, DM C and DM D) showcase no convective region besides the outer envelope ($r \gtrsim 0.8$ R). As stated before, the increase in size of the radiative region, and thus g-cavity, is a consequence of the decrease in temperature in the stellar core, which renders convection unfeasible in the region. Once again, the two different signatures between DM and (essentially) non-DM models are present and reinforce the consistency of the results.

Finally, it is interesting to note that some DM models have a lower χ^2_{star} than the SSG model. For DM Calib, the decrease in almost 8% of this quantity is substantial and the fact that DM A, B and C also represent an improvement on the Standard model's value reinforces the argument that the existence of DM is not incompatible with the current observational data for this star. However, the $\chi^2_{r_{02}}$ diagnostic increased in about 4% for DM Calib (even more for DM B) which hints towards the fact that the model might have fallen victim to an equivalent of overfitting. This means that, since the optimisation is done with respect to χ^2_{star}, other parameters of the star might have been affected to achieve a better performance in that specific diagnostic. Either way, the deviation on $\chi^2_{r_{02}}$ is not as significant as in the previous

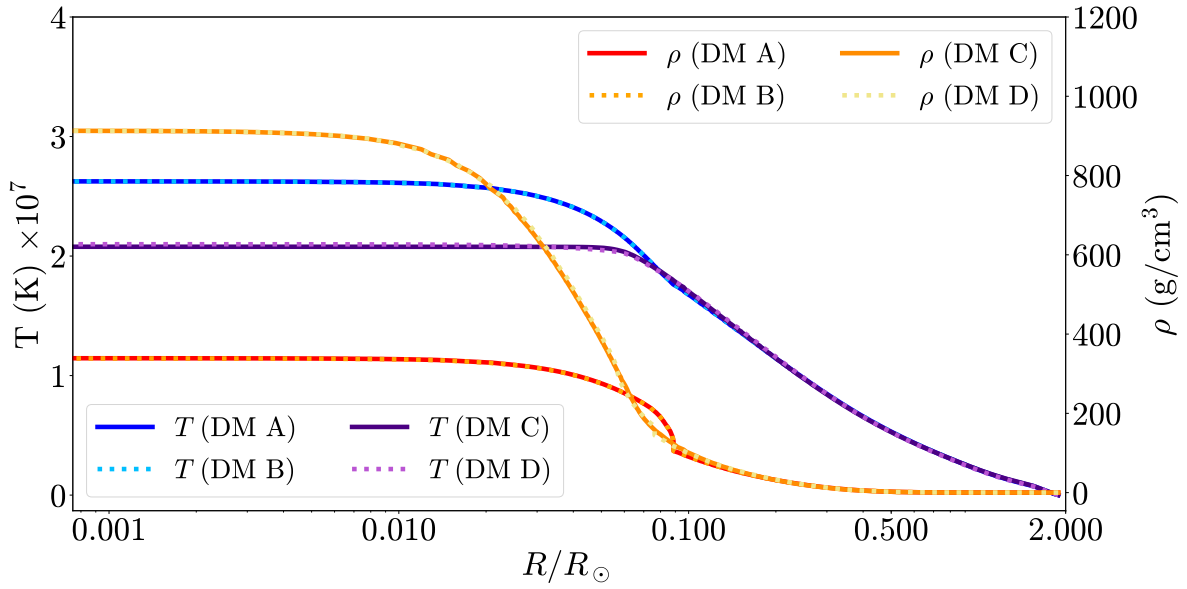

Figure 5.4: Temperature (left axis) and baryonic density (right axis) profiles of the DM stellar models (see Table 5.1).

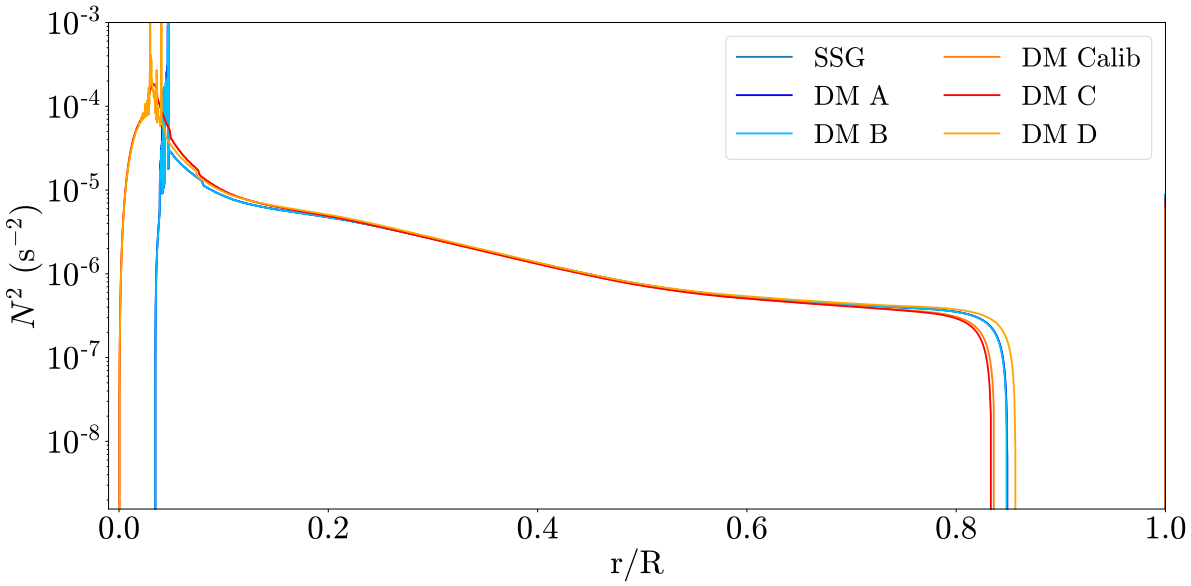

Figure 5.5: Brunt-Väisälä frequency diagram for the models in Table 5.1. The region below the curves is the g-mode cavity – and radiative region –, in accordance with fig. 2.2. The extremes of this cavity are r_1 and r_2 and are present in the integral of eq. (2.43).

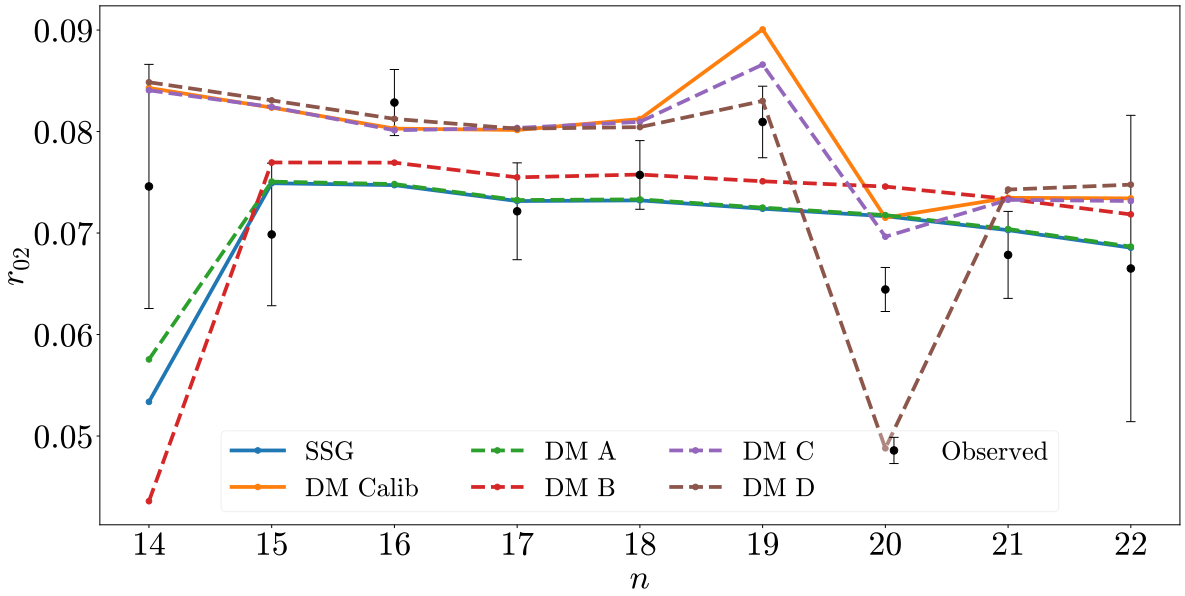

Figure 5.6: r_{02} ratios (see eq. (2.42)) for the models in Table 5.1 compared to observations. The dashed lines represent the 4 models with fixed values of (m_χ, $\sigma_{\rm SD}$).

diagnostic. To better infer on the $\chi^2_{r_{02}}$ discrepancy, we compute $r_{02}(n)$ as shown in fig. 5.6.

The results for $r_{02}(n)$ show that although the DM Calib ratio values deviate more from the observational average than the SSG's, the behaviour pattern is similar to that of the observed r_{02} (particularly around $n \sim 19-20$). Fig. 5.6 also shows that model DM C has the same regime as DM Calib, but slightly closer to the observation values, which is reflected in its smaller $\chi^2_{r_{02}}$.

Again, the two regimes are distinctively visible, with DM B being somewhat of an intermediate model. This is also expected since in this model $\sigma_{\rm SD}$ is in-between that of DM A and DM C, which showcase each one of the two different regimes.

6

Asteroseismic analysis in the DM parameter space

Contents

After understanding some of the impact that ADM produces in KIC 8228742, it is interesting to use that knowledge to devise a method to constrain the mass and spin-dependent cross-section of the DM particles. As seen before, this could be achieved by delving into the inner stellar regions by using the suitable probing mechanisms. In this chapter we apply some of the asteroseismic diagnostics defined in Sections 2.3 and 4.3 to better infer on the sensitivity of stellar models to ADM effects and to draw constraints on DM properties.

6.1 Probing the parameter space $m_\chi - \sigma_{\mathrm{SD}}$

Using the input stellar parameters of the SSG model as benchmark (see first row, columns 3-7 in Table 5.1) and enabling the ADM interactions described in Chapter 3, we decide to explore the sensitivity of the models in DM parameter space. This is achieved by computing 100 models in a $m_\chi - \sigma_{\mathrm{SD}}$ grid with fixed dark matter parameters within the range $4 \leqslant m_\chi \leqslant 12$ GeV and $10^{-40} \leqslant \sigma_{\mathrm{SD}} \leqslant 10^{-35}$ cm^2. As before, this range of values was chosen in agreement with the DM parameter space usually explored in the literature (e.g., [55]). Each input group in this grid was then used to create a model (i.e., one single model, differently from the optimisation process discussed in the previous sections) for which χ^2_{star} was computed, allowing for the drawing of contour plots showcasing the parameter region of interest and corresponding DM parameters (fig. 6.1).

A normalised $\overline{\chi}^2_{\mathrm{star}}$ was defined as:

$$\overline{\chi}^2_{\mathrm{star}} = \frac{\chi^2_{\mathrm{DM}}}{\chi^2_{\mathrm{SSG}}}, \tag{6.1}$$

where χ^2_{DM} corresponds to the χ^2_{star} of each model taking DM into account and, likewise, χ^2_{SSG} is that same value for the Standard model (in this case $\chi^2_{\mathrm{SSG}} = 5.735 \times 10^{-3}$, see Table 5.1).

On the one hand, it is visible that the overall tendency is for stellar models with lower interaction cross-section to agree better with observations. On the other hand, there are some models with higher σ_{SD} that do not converge, meaning that the benchmark input parameters coupled with the given DM quantities cannot converge to an acceptable solution of the stellar evolution differential equations. This happened for models with σ_{SD} larger than 4×10^{-36} cm^2, where although not explicitly shown in the figure, the χ^2 values rose to orders of magnitude of 10^2. This relation between the cross-section and $\overline{\chi}^2_{\mathrm{star}}$ is somewhat expected since the lower the σ_{SD} the smaller the influence of DM is on the stellar structure. Thus, the lower region of the grid performs better than the upper region since it naturally tends to the SSG case. However, it is still worth noting that for σ_{SD} as high as 10^{-37} cm^2 some models seem to perform well.

Furthermore, by looking at the contour line that defines models as good as the SSG model (at $\overline{\chi}^2_{\mathrm{star}} = 1$, see fig. 6.1), it is visible that a large portion of the 100 DM stellar models outperform it. This means that most dark matter models with the same inputs as the SSG but with m_χ between 4 and 12

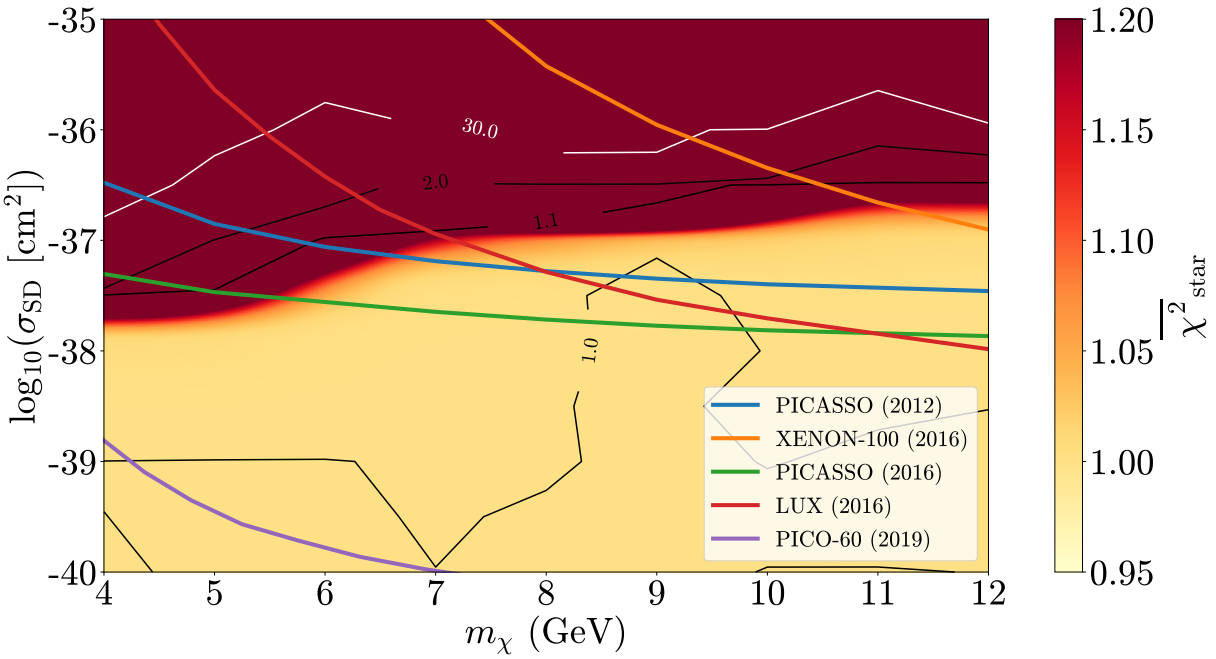

Figure 6.1: Contours for $\overline{\chi}^2_{\rm star}$ (see eqs. (4.1) and (6.1)): lighter shades represent lower χ^2 and thus better models for this specific diagnostic. The contour for $\overline{\chi}^2_{\rm star} = 1$ represents models as good as the SSG model. Direct detection experiment results from XENON-100 [113], LUX [26], PICASSO [23, 114] and PICO-60 [24] are shown as solid lines.

GeV and $\sigma_{\rm SD}$ between 10^{-40} and 4×10^{-39} cm^2 fit the spectroscopy and large frequency separation observations better than the best performing no-DM model. It should be noted that despite the fact that $\sigma_{\rm SD} = 10^{-40}$ cm^2 is a hard limit, i.e., it was chosen by default, that does not mean that the improvement in $\overline{\chi}^2_{\rm star}$ is observed for any $\sigma_{\rm SD}$ below this value. In fact, we also obtained models below the minimum cross-section considered in fig. 6.1 (e.g., $\sigma_{\rm SD} = 10^{-42}$ cm^2) and observed that the $\chi^2_{\rm star}$ diagnostic again tended to the SSG value (i.e., $\overline{\chi}^2_{\rm star} = 1$), which is expected since DM is less influential for lower interaction cross-sections. Additionally, we found a model near $m_\chi = 9$ GeV and $\sigma_{\rm SD} = 3 \times 10^{-38}$ cm^2 that exhibits the lowest $\chi^2_{\rm star}$ of the set.

It is interesting, however, to study the performance of the best performing model and all the others under the $\chi^2_{r_{02}}$ diagnostic defined in Section 4.3. To achieve that, the r_{02} ratio was computed for all models in the grid and compared to observations, i.e., the ratio that was computed with the 32 frequencies observed in the star. After that, $\chi^2_{r_{02}}$ was computed and yet again plotted in contours.

The results shown in fig. 6.2 confirm the overall trend seen before in fig. 6.1: models in the lower region of the grid seem to more accurately agree with the observed r_{02} which, in itself, grants more confidence to the previous results. The contour that defines models with similar performance to that of the SSG model was again explicitly drawn at $\overline{\chi}^2_{r_{02}} = 1$. Once more, most models with $\sigma_{SD} < 10^{-38}$ cm^2 outperform the best model with no dark matter interactions, this time on a different diagnostic that better

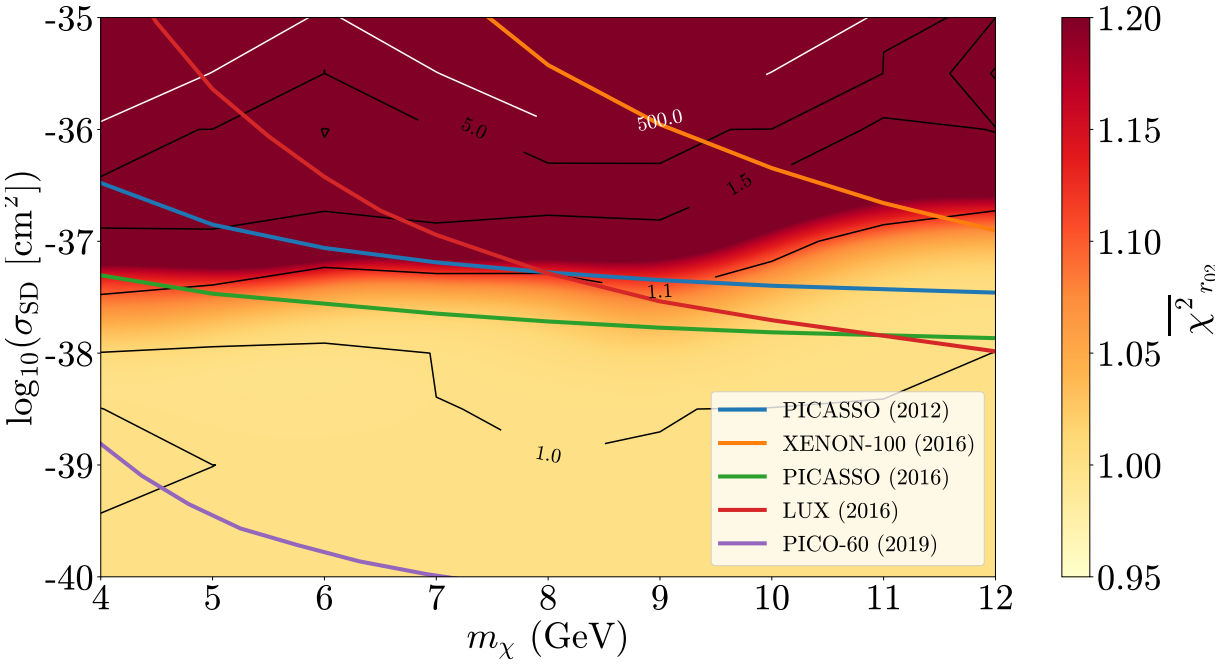

Figure 6.2: Contours for $\overline{\chi}^2_{r_{02}}$ (eq. (4.2) and normalised similarly to eq. (6.1)): lighter shades represent lower χ^2 and thus better models for this specific diagnostic. The contour for $\overline{\chi}^2_{r_{02}} = 1$ represents models as good as the SSG model. Direct detection experiment results from XENON-100 [113], LUX [26], PICASSO [23, 114] and PICO-60 [24] are shown as solid lines.

represents the core structure.

It is also interesting to note that the best performing model of the previous set (fig. 6.1) is not in the same region of the best performing models in the $\chi^2_{r_{02}}$ diagnostic. This is a case where the spectroscopic results out-shadowed the structural differences in the first diagnostic, which was then covered by calculating the r_{02} ratio. Hence, the two step rejection method proves to be valuable in cases like this, since normally that model would have been accepted by passing the $\chi^2_{\rm star}$ diagnostic with the lowest value.

A simple additional test can be done by combining the two methods, taking the maximum value of both diagnostics, $\overline{\chi}^2_{\rm total} = \max(\overline{\chi}^2_{\rm star}, \overline{\chi}^2_{r_{02}})$. This is shown in fig. 6.3, as well as the region within the $\overline{\chi}^2_{\rm total} = 1$ contour which represents the models that outperform the SSG model in both diagnostics.

When comparing the aforementioned grids with the direct detection experiment's limits we see that our method could provide complementary $m_\chi - \sigma_{\rm SD}$ exclusion diagrams. This could be achieved by defining a cut-off χ^2 since it is visible that there is a steep transition region between the two regimes (from yellow to dark red) which indicates a rapid disagreement between the stellar models and the observational data. The behaviour showcased in figs. 6.1 to 6.3 can be compared to that of the limits from PICASSO [23, 114] and LUX [26]. Moreover, it seems to suggest harder limits than those of XENON-100 [113], which is not as competitive for lower m_χ. Taking into account the SSG model as

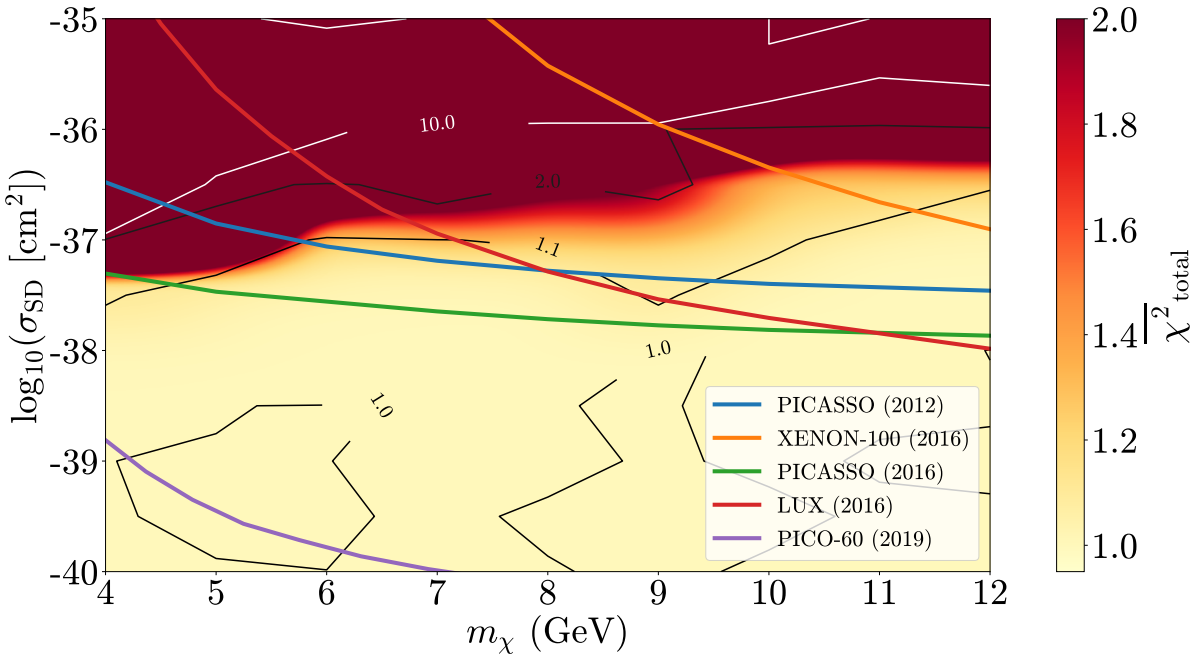

Figure 6.3: Maximum value between $\chi^2_{\rm star}$ and $\chi^2_{r_{02}}$: the contour for $\overline{\chi}^2_{\rm total} = 1$ represents the models with an equated performance to the SSG model, using their worst diagnostic. Direct detection experiment results from XENON-100 [113], LUX [26], PICASSO [23, 114] and PICO-60 [24] are shown as solid lines.

the benchmark we can hint towards the region with $\sigma_{\rm SD} \gtrsim 10^{-37}\ {\rm cm}^2$ where $\overline{\chi}^2_{\rm total}$ rapidly increases, meaning that ADM presence in this SG star is strongly disfavoured by both spectroscopic and seismic observations.

Finally, it should be noted that the models obtained in the previous section – which were obtained by calibrating the stellar and, in the case of DM Calib, the DM parameters – can fall in the excluded region suggested in fig. 6.3 (see Table 5.1) and still yield stellar models that are in agreement with the observational data. This may be due to the increase in the degrees of freedom associated with the extra free parameters which, given that the observational error for the star in question is substantial, allows the method to find different combinations of parameters that still fit the reality. Therefore, with access to more precise measurements from future spectroscopy and asteroseismology missions, one can expect to calibrate a standard benchmark model that allows the drawing of exclusion diagrams with more certainty.

6.2 Period Spacing Analysis

When further analysing the oscillation eigenfunctions of several models, it is clear that the amplitude rapidly falls off within the first outer 20% of the star radius (see fig. 6.4). This means that despite using

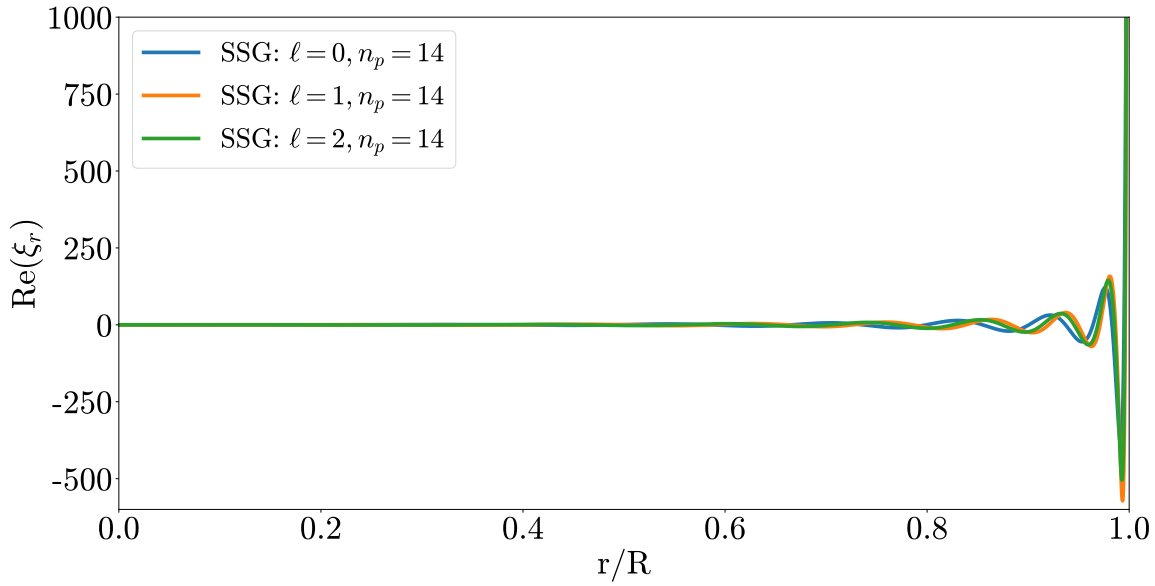

Figure 6.4: Radial displacement ξ_r for p-modes of $n = 14$ and $\ell = 0, 1, 2$ for the SSG model.

a seismic ratio that is designed to gather more information about the stellar interior, the acoustic modes that defined the diagnostic fall short on this task. Thus, we can conclude that the r_{02} diagnostic is not as sensitive to the core as expected, being more representative of the stellar envelope, contrary to what happens in a typical MS star.

Motivated by this, we change our focus to the gravitational character of the oscillations, which, as seen before, should be specially sensitive to the stellar interior. This is done by analysing the mixed modes of the various models, which allows the extraction of the relevant quantities of the gravity contribution.

In particular, the asymptotic value of the large period separation presented in eq. (2.43) can be computed from the MESA models for $\ell = 1$ and $\ell = 2$, for which there are mixed modes. It is expected that if the presence of DM in stars directly affects the size of their convective cores, as we have seen in previous sections, then the period spacing will serve as a good probing tool [37]. The $\Delta\Pi_\ell$ values are shown in the two last columns of Table 5.1. The already mentioned regimes are once again clearly noticeable: there is a substantial decrease in period spacing when DM is strongly influential that can go up to 66% of the benchmark value (from SSG). This, again, is explained by the suppression of the convective core caused by DM, which in turn leads to an increase of the g-mode cavity, producing a direct effect on the integral in eq. (2.43). This effect is clearly visible in fig. 5.5.

As before, we define the $\Delta\Pi_\ell$ deviation from the SSG model for the same grid of DM models to better understand the impact that the different DM parameters have on the core of the star. The variation of $\Delta\Pi_1$ is shown in fig. 6.5. We only show the case with $\ell = 1$, given that, by definition, in the asymptotic limit, $\Delta\Pi_1$ and $\Delta\Pi_2$ only differ by a multiplying constant. The darker region represents models where

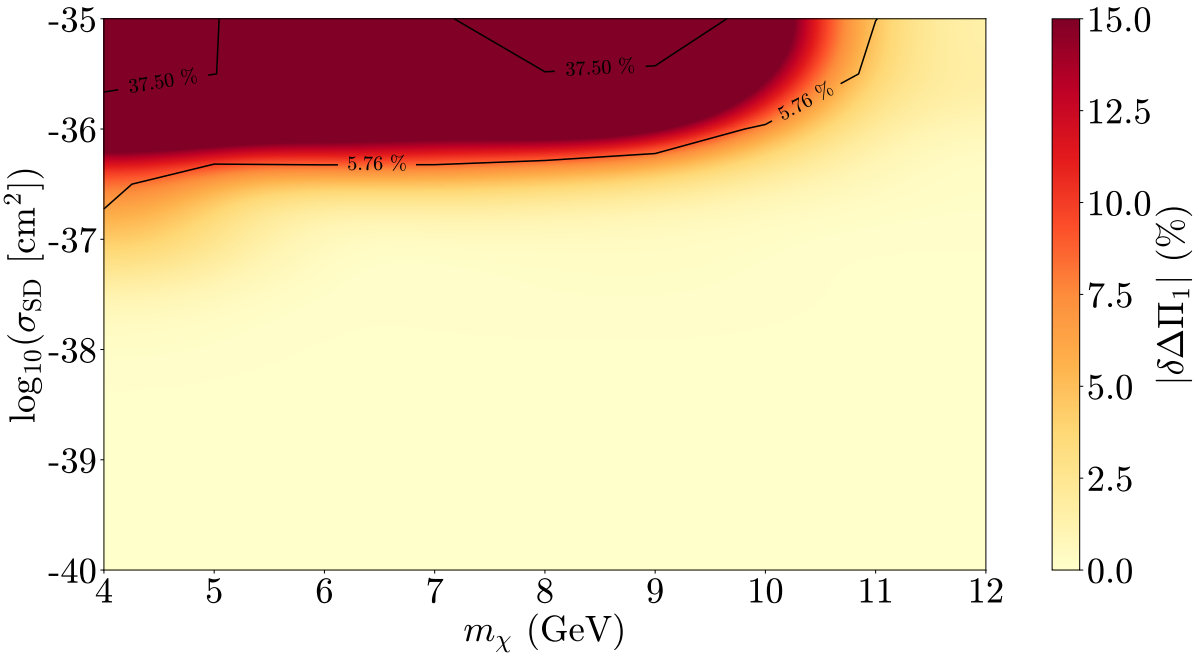

Figure 6.5: Contour plot of the deviation of the period separation $\Delta\Pi_1$ from the SSG model for the same grid of models. The two black curves represent the lower and upper boundaries of the relative error of measurement of this quantity for 39 SG stars from Mosser *et al.* [115] ([37]).

$|\delta\Delta\Pi_1|$ is larger than 15% and, in some cases, models reach the 60% mark as was already the case for some models in Table 5.1. It is also clear that larger masses of ADM particles tend to result in less effects. This is twofold: first, these particles are harder to capture by virtue of requiring a larger transfer of momentum upon recoil in order to reach a velocity lower than the escape velocity (e.g., [85, 116]); secondly, if eventually captured, they cluster strongly in the innermost regions of the star and, thus, their impact is naturally not felt as much. It is important to note that most of the deviations shown in the grid happen in the negative direction, with DM impacted models exhibiting a smaller period spacing, as expected.

The overall tendency in fig. 6.5 mimics that of figs. 6.1 to 6.3: models in the upper part of the grid show a larger ADM influence on the star. Yet again, the transition region between the two regimes is narrow. The region below the 5.76% contour represents models whose $\Delta\Pi_1$ variation is lower than the lowest relative uncertainty among the large period separation measurements in Mosser *et al.* [115]. Likewise, models above the 37.50% curve exhibit a variation that surpasses the uncertainty of the less precise measurements. Both these statements mean that current experiments may not have enough sensitivity to resolve DM signatures in SG stars in the transition region (where the lower relative uncertainty contour is) and particularly in the region below the 37.50% contour. Above that curve, the effect should be detected, with the deviation being greater than the observable uncertainty in the worst cases. However, one should note that if this analysis is carried out for a SG star which allows for a more precise

measurement of $\Delta\Pi_1$ (i.e., closer to the 5.76% mark) there should be enough sensitivity to draw any valuable conclusions regarding the acceptability of DM models for that star. In the future, this diagnostic could be used with measurement data as the benchmark, providing a strong case for model rejection and, additionally, ADM parameter constraints.

7

Conclusions

Contents

This thesis focuses on ADM interactions with stellar matter and their effects on SG stars. We use asteroseismology to infer on constraints for DM parameters: mass and SD cross-section of interaction.

Subgiant stars are but a small fraction of the currently observed stars by virtue of that evolutionary stage being relatively short. Despite that, they can pose as important laboratories for the study of dark matter constraints. In this work, we obtained calibrated stellar models of the SG KIC 8228742 assuming both the presence and absence of ADM spin-dependent interactions. Focusing on SD interactions allows us to directly compare our results to the corresponding constraints placed by detectors which study the same type of interactions. More importantly, by studying only SD couplings, we essentially neglect interactions with elements heavier than hydrogen, and thus also any direct effect that DM has on the star during the SG phase. Then, by carrying out this study we take advantage of the seismological benefits of the SG phase to study DM interactions in the MS stage.

The results shown in this dissertation point towards the fact that, overall, DM models are in agreement with current observations of this star.

We present a new robust method of stellar calibration that can take into account the DM parameters. This, in theory, could provide sensible values for m_χ and $\sigma_{\rm SD}$ of ADM particles by being applied to a star with precise measurements of both fundamental and seismic properties. Besides, by using seismic diagnostics weighed towards the core of the star, we probe the DM parameter space

7.1 Summary and Achievements

Firstly, in an attempt to study the possibility of ADM presence in SG stars, we present a new robust method of stellar modelling that introduces dark matter parameters into the calibration and optimisation processes. This is a new approach which aims to find the best models, in terms of the diagnostics proposed in this work, disregarding any prior standard (with no dark matter influence) benchmark models. In theory, using this method could provide sensible optimal values for m_χ and $\sigma_{\rm SD}$ of ADM particles by being applied to a star with precise measurements of both fundamental and seismic properties.

As for results, calibrated models with strong DM influence showcased a different regime from both the standard (SSG) model and DM models with lower $\sigma_{\rm SD}$. Phenomena like the suppression of the convective core, the cooling of the inner core and the increase in density of that region were all present and in agreement with past findings (e.g., [34, 36, 93, 112]). We later conclude that the results obtained at this stage of the work, which provided an optimal pair of ADM particle mass and spin-dependent cross-section of $m_\chi = 9.12\ \mathrm{GeV}$ and $\sigma_{\rm SD} = 2.32 \times 10^{-36}\mathrm{cm}^2$ may not be sufficient to constrain the DM particle candidates' properties (see section 7.2).

Using seismological diagnostics as a second probing tool, we then present a method to study the influence of DM in the interior of stars, with direct applicability to SGs. The r_{02} ratio is used in an attempt

to probe the stellar core, which is the region that ADM severely impacts. A study of the deviation of r_{02} from observational measurements allows us to draw several sensitivity grids (see figs. 6.1 to 6.3) which showcase the increasing influence that DM has with the increase of the spin-dependent cross-section of the interaction between ADM particles and stellar matter.

Moreover, those same figures show a class of models with $10^{-40} \leqslant \sigma_{\mathrm{SD}} < 10^{-38}$ cm^2 that consistently outperform the best standard models, which strengthens the argument that the presence of ADM particles in this star does not go against observations. Additionally, a σ_{SD} admissible region is suggested for values up to 10^{-37} cm^2 where the χ^2 diagnostics start to deteriorate from observations. This value is comparable to those of the PICASSO ([23, 114]) and LUX ([26]) experiments and improves that of XENON-100 ([113]). Then, an exclusion limit may be drawn with more certainty at $\sigma_{\mathrm{SD}} \gtrsim 10^{-35}$ cm^2 since results from both Chapter 5 and 6 find this region as incompatible with current observations. This conclusion is similar to what Casanellas & Lopes [36] and Martins *et al.* [55] found previously for MS stars.

Lastly, we propose an additional seismic parameter to study DM influence on SG stars that allows us to further probe the stellar core. As the acoustic modes were mainly probing the stellar envelope (contrary to what typically happens in MS stars), we turned our attention to gravity and mixed modes, which carry more information about the core since they travel deeper into the stellar interior. The $\Delta\Pi_\ell$ diagnostic was calculated for the same grid of models and the results again confirm the previous analysis and hint towards the possibility of drawing exclusion diagrams for a SG star for which we have the $\Delta\Pi_\ell$ observations.

7.2 Limitations and Future Work

Naturally, the development of a thesis does not come without limitations and shortcomings. For instance, as referred in the previous section, the method here devised to include m_χ and σ_{SD} into the optimisation process of stellar calibrations falls short when compared to later results.

A number of limitations can be pointed out as the cause for this. The number of spectroscopic quantities of this star that we have measurements for pose a problem when introducing more parameters into the input group, since overfitting – typical of situations where there are too many parameters relative to the available data points – may be happening here. The precision of the current measurements is also a factor since it broadens the accepted model spectrum and limits the certainty of a possible exclusion limit. Lastly, computational time constraints were a large limitation to the minimisation problem and this is an aspect that has the potential for clear improvements. The rationale behind using DM parameters as direct inputs for the optimisation process of a stellar calibration has a lot of potential to aid the discovery of new exclusion limits for these properties. Having enough computational resources will render this task

more feasible and, for example, the study done in Chapter 6 could then be carried out without a no-DM model serving as benchmark, but instead with all 100 DM models being calibrated and optimised one by one.

Additionally, in the future, missions like PLATO [61], which will provide high precision measurements of both spectroscopic and seismic quantities, will allow for a more extensive analysis of the impact of ADM in stars and, more importantly, will make the drawing of exclusion diagrams possible, using the method we present in Section 6.2. With better measurements, we also expect the calibration with DM quantities as inputs to provide a better result, with less impact from numerical constraints. In fact, we expect to publish a second article based on this analysis, for another SG star, for which there are $\Delta\Pi_\ell$ measurements.

Another aspect to consider in the future is the inclusion of spin-independent interactions which will certainly drive the DM impact in the later stages of the stellar evolution, by allowing the interaction with helium and heavier elements as well.

Bibliography

[1] G. Bertone, D. Hooper, and J. Silk, "Particle dark matter: evidence, candidates and constraints," *Physics Reports*, vol. 405, no. 5-6, p. 279–390, Jan 2005. [Online]. Available: http://dx.doi.org/10.1016/j.physrep.2004.08.031

[2] F. Zwicky, "Die Rotverschiebung von extragalaktischen Nebeln," *Helvetica Physica Acta*, vol. 6, pp. 110–127, Jan. 1933.

[3] V. C. Rubin *et al.*, "Motion of the Galaxy and the Local Group determined from the velocity anisotropy of distant Sc I galaxies. I. The data." *Astronomical Journal*, vol. 81, pp. 687–718, Sep. 1976.

[4] N. Aghanim *et al.*, "Planck 2018 results," *Astronomy & Astrophysics*, vol. 641, p. A6, Sep 2020. [Online]. Available: http://dx.doi.org/10.1051/0004-6361/201833910

[5] V. N. Lukash, E. Mikheeva, and A. Malinovsky, "Formation of the large-scale structure of the Universe," *Uspekhi Fizicheskih Nauk*, vol. 181, no. 10, p. 1017, 2011. [Online]. Available: http://dx.doi.org/10.3367/UFNr.0181.201110a.1017

[6] C. Frenk and S. White, "Dark matter and cosmic structure," *Annalen der Physik*, vol. 524, no. 9-10, p. 507–534, Sep 2012. [Online]. Available: http://dx.doi.org/10.1002/andp.201200212

[7] L. Roszkowski, E. M. Sessolo, and S. Trojanowski, "WIMP dark matter candidates and searches—current status and future prospects," *Reports on Progress in Physics*, vol. 81, no. 6, p. 066201, May 2018. [Online]. Available: http://dx.doi.org/10.1088/1361-6633/aab913

[8] B. Moore, S. Ghigna, F. Governato, G. Lake, T. Quinn, J. Stadel, and P. Tozzi, "Dark matter substructure within galactic halos," *The Astrophysical Journal*, vol. 524, no. 1, p. L19–L22, Oct 1999. [Online]. Available: http://dx.doi.org/10.1086/312287

[9] A. Klypin, A. V. Kravtsov, O. Valenzuela, and F. Prada, "Where are the missing galactic satellites?" *The Astrophysical Journal*, vol. 522, no. 1, p. 82–92, Sep 1999. [Online]. Available: http://dx.doi.org/10.1086/307643

[10] M. Boylan-Kolchin, J. S. Bullock, and M. Kaplinghat, "Too big to fail? the puzzling darkness of massive Milky Way subhaloes," *Monthly Notices of the Royal Astronomical Society: Letters*, vol. 415, no. 1, p. L40–L44, Jun 2011. [Online]. Available: http://dx.doi.org/10.1111/j.1745-3933.2011.01074.x

[11] ——, "The Milky Way's bright satellites as an apparent failure of ΛCDM," *Monthly Notices of the Royal Astronomical Society*, vol. 422, no. 2, p. 1203–1218, Mar 2012. [Online]. Available: http://dx.doi.org/10.1111/j.1365-2966.2012.20695.x

[12] H. Baer, K.-Y. Choi, J. E. Kim, and L. Roszkowski, "Dark matter production in the early universe: Beyond the thermal wimp paradigm," *Physics Reports*, vol. 555, p. 1–60, Feb 2015. [Online]. Available: http://dx.doi.org/10.1016/j.physrep.2014.10.002

[13] J. L. Feng, "Dark matter candidates from particle physics and methods of detection," *Annual Review of Astronomy and Astrophysics*, vol. 48, no. 1, p. 495–545, Aug 2010. [Online]. Available: http://dx.doi.org/10.1146/annurev-astro-082708-101659

[14] G. Bertone and T. M. P. Tait, "A new era in the search for dark matter," *Nature*, vol. 562, no. 7725, p. 51–56, Oct 2018. [Online]. Available: http://dx.doi.org/10.1038/s41586-018-0542-z

[15] G. Bertone and D. Hooper, "History of dark matter," *Rev. Mod. Phys.*, vol. 90, p. 045002, Oct 2018. [Online]. Available: https://link.aps.org/doi/10.1103/RevModPhys.90.045002

[16] S. Lazanu, I. Lazanu, and G. Ciobanu, "Modelling the transient processes produced under heavy particle irradiation," *Nuclear Instruments and Methods in Physics Research Section B: Beam Interactions with Materials and Atoms*, vol. 269, no. 4, p. 498–503, Feb 2011. [Online]. Available: http://dx.doi.org/10.1016/j.nimb.2010.12.064

[17] J. Vergados, H. Ejiri, and K. Savvidy, "Theoretical direct wimp detection rates for inelastic scattering to excited states," *Nuclear Physics B*, vol. 877, no. 1, p. 36–50, Dec 2013. [Online]. Available: http://dx.doi.org/10.1016/j.nuclphysb.2013.09.010

[18] G. Bertone, "The moment of truth for wimp dark matter," *Nature*, vol. 468, no. 7322, p. 389–393, Nov 2010. [Online]. Available: http://dx.doi.org/10.1038/nature09509

[19] T. M. Undagoitia and L. Rauch, "Dark matter direct-detection experiments," *Journal of Physics G: Nuclear and Particle Physics*, vol. 43, no. 1, p. 013001, Dec 2015. [Online]. Available: http://dx.doi.org/10.1088/0954-3899/43/1/013001

[20] M. Schumann, "Direct detection of wimp dark matter: concepts and status," *Journal of Physics G: Nuclear and Particle Physics*, vol. 46, no. 10, p. 103003, Aug 2019. [Online]. Available: http://dx.doi.org/10.1088/1361-6471/ab2ea5

[21] J. Beringer *et al.*, "Review of particle physics," *Phys. Rev. D*, vol. 86, p. 010001, Jul 2012. [Online]. Available: https://link.aps.org/doi/10.1103/PhysRevD.86.010001

[22] V. Barger, W.-Y. Keung, and G. Shaughnessy, "Spin dependence of dark matter scattering," *Physical Review D*, vol. 78, no. 5, Sep 2008. [Online]. Available: http://dx.doi.org/10.1103/PhysRevD.78.056007

[23] E. Behnke *et al.*, "Final results of the picasso dark matter search experiment," *Astroparticle Physics*, vol. 90, p. 85–92, Apr 2017. [Online]. Available: http://dx.doi.org/10.1016/j.astropartphys.2017.02.005

[24] C. Amole *et al.*, "Dark matter search results from the complete exposure of the pico-60 c3f8 bubble chamber," *Physical Review D*, vol. 100, no. 2, Jul 2019. [Online]. Available: http://dx.doi.org/10.1103/PhysRevD.100.022001

[25] E. Aprile *et al.*, "Limits on spin-dependent wimp-nucleon cross sections from 225 live days of xenon100 data," *Physical Review Letters*, vol. 111, no. 2, Jul 2013. [Online]. Available: http://dx.doi.org/10.1103/PhysRevLett.111.021301

[26] D. Akerib *et al.*, "Results on the spin-dependent scattering of weakly interacting massive particles on nucleons from the run 3 data of the lux experiment," *Physical Review Letters*, vol. 116, no. 16, Apr 2016. [Online]. Available: http://dx.doi.org/10.1103/PhysRevLett.116.161302

[27] Y. Cui and R. Sundrum, "Baryogenesis for weakly interacting massive particles," *Physical Review D*, vol. 87, no. 11, Jun 2013. [Online]. Available: http://dx.doi.org/10.1103/PhysRevD.87.116013

[28] J. Shelton and K. M. Zurek, "Darkogenesis: A baryon asymmetry from the dark matter sector," *Physical Review D*, vol. 82, no. 12, Dec 2010. [Online]. Available: http://dx.doi.org/10.1103/PhysRevD.82.123512

[29] M. L. Graesser, I. M. Shoemaker, and L. Vecchi, "Asymmetric wimp dark matter," *Journal of High Energy Physics*, vol. 2011, no. 10, Oct 2011. [Online]. Available: http://dx.doi.org/10.1007/JHEP10(2011)110

[30] H. Iminniyaz, M. Drees, and X. Chen, "Relic abundance of asymmetric dark matter," *Journal of Cosmology and Astroparticle Physics*, vol. 2011, no. 07, p. 003–003, Jul 2011. [Online]. Available: http://dx.doi.org/10.1088/1475-7516/2011/07/003

[31] W. H. Press and D. N. Spergel, "Capture by the sun of a galactic population of weakly interacting, massive particles," *The Astrophysical Journal*, vol. 296, pp. 679–684, Sep. 1985.

[32] A. Gould, “Evaporation of WIMPs with Arbitrary Cross Sections,” *Astrophysical Journal*, vol. 356, p. 302, Jun. 1990.

[33] C. Kouvaris, “Probing light dark matter via evaporation from the sun,” *Physical Review D*, vol. 92, no. 7, Oct 2015. [Online]. Available: http://dx.doi.org/10.1103/PhysRevD.92.075001

[34] M. Taoso *et al.*, “Effect of low mass dark matter particles on the sun,” *Phys. Rev. D*, vol. 82, p. 083509, Oct 2010. [Online]. Available: https://link.aps.org/doi/10.1103/PhysRevD.82.083509

[35] I. P. Lopes, J. Silk, and S. H. Hansen, “Helioseismology as a new constraint on supersymmetric dark matter,” *Monthly Notices of the Royal Astronomical Society*, vol. 331, no. 2, pp. 361–368, 03 2002. [Online]. Available: https://doi.org/10.1046/j.1365-8711.2002.05238.x

[36] J. Casanellas and I. Lopes, “First asteroseismic limits on the nature of dark matter,” *The Astrophysical Journal*, vol. 765, no. 1, p. L21, Feb 2013. [Online]. Available: http://dx.doi.org/10.1088/2041-8205/765/1/L21

[37] J. Lopes, I. Lopes, and J. Silk, “Asteroseismology of red clump stars as a probe of the dark matter content of the galaxy central region,” *The Astrophysical Journal*, vol. 880, no. 2, p. L25, jul 2019. [Online]. Available: https://doi.org/10.3847%2F2041-8213%2Fab2fdd

[38] I. P. Lopes, G. Bertone, and J. Silk, “Solar seismic model as a new constraint on supersymmetric dark matter,” *Monthly Notices of the Royal Astronomical Society*, vol. 337, no. 4, pp. 1179–1184, 12 2002. [Online]. Available: https://doi.org/10.1046/j.1365-8711.2002.05835.x

[39] S. Turck-Chièze, R. García, I. Lopes *et al.*, “First study of dark matter properties with detected solar gravity modes and neutrinos,” *The Astrophysical Journal Letters*, vol. 746, p. L12, 01 2012.

[40] M. Asplund, N. Grevesse, A. J. Sauval, and P. Scott, “The chemical composition of the sun,” *Annual Review of Astronomy and Astrophysics*, vol. 47, no. 1, p. 481–522, Sep 2009. [Online]. Available: http://dx.doi.org/10.1146/annurev.astro.46.060407.145222

[41] J. Christensen-Dalsgaard, “Helioseismology,” *Reviews of Modern Physics*, vol. 74, no. 4, p. 1073–1129, Nov 2002. [Online]. Available: http://dx.doi.org/10.1103/RevModPhys.74.1073

[42] J. N. Bahcall, A. M. Serenelli, and S. Basu, “New solar opacities, abundances, helioseismology, and neutrino fluxes,” *The Astrophysical Journal*, vol. 621, no. 1, p. L85–L88, Jan 2005. [Online]. Available: http://dx.doi.org/10.1086/428929

[43] D. Capelo and I. Lopes, “The impact of composition choices on solar evolution: age, helio- and asteroseismology, and neutrinos,” *Monthly Notices of the Royal Astronomical Society*, vol. 498, no. 2, p. 1992–2000, Sep 2020. [Online]. Available: http://dx.doi.org/10.1093/mnras/staa2402

[44] I. Lopes, P. Panci, and J. Silk, "Helioseismology with long-range dark matter-baryon interactions," *The Astrophysical Journal*, vol. 795, no. 2, p. 162, Oct 2014. [Online]. Available: http://dx.doi.org/10.1088/0004-637X/795/2/162

[45] A. C. Vincent, P. Scott, and A. Serenelli, "Possible indication of momentum-dependent asymmetric dark matter in the sun," *Physical Review Letters*, vol. 114, no. 8, Feb 2015. [Online]. Available: http://dx.doi.org/10.1103/PhysRevLett.114.081302

[46] Gaia-ESO Survey Team *et al.*, "The Gaia-ESO Public Spectroscopic Survey," *The Messenger*, vol. 147, pp. 25–31, Mar. 2012.

[47] Gaia Collaboration, "The Gaia mission," *Astronomy & Astrophysics*, vol. 595, p. A1, Nov. 2016.

[48] M. Bergemann and A. Serenelli, "Solar abundance problem," *GeoPlanet: Earth and Planetary Sciences*, p. 245–258, 2014. [Online]. Available: http://dx.doi.org/10.1007/978-3-319-06956-2_21

[49] S. Turck-Chièze and S. Couvidat, "Solar neutrinos, helioseismology and the solar internal dynamics," *Reports on Progress in Physics*, vol. 74, no. 8, p. 086901, Jul 2011. [Online]. Available: http://dx.doi.org/10.1088/0034-4885/74/8/086901

[50] M. J. Thompson, J. Christensen-Dalsgaard, M. S. Miesch, and J. Toomre, "The internal rotation of the sun," *Annual Review of Astronomy and Astrophysics*, vol. 41, no. 1, pp. 599–643, 2003. [Online]. Available: https://doi.org/10.1146/annurev.astro.41.011802.094848

[51] R. Howe, "Solar interior rotation and its variation," *Living Reviews in Solar Physics*, vol. 6, 2009. [Online]. Available: http://dx.doi.org/10.12942/lrsp-2009-1

[52] M. H. Pinsonneault, S. D. Kawaler, S. Sofia, and P. Demarque, "Evolutionary Models of the Rotating Sun," *Astrophysical Journal*, vol. 338, p. 424, Mar. 1989.

[53] W. J. Chaplin and A. Miglio, "Asteroseismology of solar-type and red-giant stars," *Annual Review of Astronomy and Astrophysics*, vol. 51, no. 1, p. 353–392, Aug 2013. [Online]. Available: http://dx.doi.org/10.1146/annurev-astro-082812-140938

[54] J. Casanellas and I. Lopes, "Towards the use of asteroseismology to investigate the nature of dark matter," *Monthly Notices of the Royal Astronomical Society*, vol. 410, no. 1, p. 535–540, Oct 2010. [Online]. Available: http://dx.doi.org/10.1111/j.1365-2966.2010.17463.x

[55] A. Martins, I. Lopes, and J. Casanellas, "Asteroseismic constraints on asymmetric dark matter: Light particles with an effective spin-dependent coupling," *Phys. Rev. D*, vol. 95, no. 2, p. 023507, 2017.

[56] M. Fridlund, A. Baglin, J. Lochard, and L. Conroy, "The corot mission pre-launch status - stellar seismology and planet finding," *ESA*, vol. 1306, 10 2006. [Online]. Available: https://www.researchgate.net/publication/234467556_The_CoRoT_Mission_Pre-Launch_Status_-_Stellar_Seismology_and_Planet_Finding

[57] E. Michel *et al.*, "CoRoT Measures Solar-Like Oscillations and Granulation in Stars Hotter Than the Sun," *Science*, vol. 322, no. 5901, p. 558, Oct. 2008.

[58] W. J. Borucki *et al.*, "Kepler planet-detection mission: Introduction and first results," *Science*, vol. 327, no. 5968, pp. 977–980, 2010.

[59] D. G. Koch *et al.*, "KEPLER MISSION DESIGN, REALIZED PHOTOMETRIC PERFORMANCE, AND EARLY SCIENCE," *The Astrophysical Journal*, vol. 713, no. 2, pp. L79–L86, mar 2010. [Online]. Available: https://doi.org/10.1088%2F2041-8205%2F713%2F2%2Fl79

[60] G. R. Ricker, J. N. Winn, R. Vanderspek *et al.*, "Transiting exoplanet survey satellite," *Journal of Astronomical Telescopes, Instruments, and Systems*, vol. 1, no. 1, p. 014003, Oct 2014. [Online]. Available: http://dx.doi.org/10.1117/1.JATIS.1.1.014003

[61] H. Rauer *et al.*, "The plato 2.0 mission," *Experimental Astronomy*, vol. 38, no. 1-2, p. 249–330, Sep 2014. [Online]. Available: http://dx.doi.org/10.1007/s10686-014-9383-4

[62] B. W. Carroll and D. A. Ostlie, *An Introduction to Modern Astrophysics*, 2nd ed. Cambridge University Press, 2017.

[63] R. Kippenhahn, A. Weigert, and A. Weiss, *Stellar Structure and Evolution*, 2012.

[64] B. Paxton, L. Bildsten, A. Dotter *et al.*, "Modules for Experiments in Stellar Astrophysics (MESA)," *The Astrophysical Journal Supplement Series*, vol. 192, p. 3, jan 2011.

[65] B. Paxton, M. Cantiello, P. Arras *et al.*, "Modules for Experiments in Stellar Astrophysics (MESA): Planets, Oscillations, Rotation, and Massive Stars," *The Astrophysical Journal Supplement Series*, vol. 208, p. 4, sep 2013.

[66] B. Paxton, P. Marchant, J. Schwab *et al.*, "Modules for Experiments in Stellar Astrophysics (MESA): Binaries, Pulsations, and Explosions," *The Astrophysical Journal Supplement Series*, vol. 220, p. 15, sep 2015.

[67] B. Paxton, J. Schwab, E. B. Bauer *et al.*, "Modules for Experiments in Stellar Astrophysics (MESA): Convective Boundaries, Element Diffusion, and Massive Star Explosions," *The Astrophysical Journal Supplement Series*, vol. 234, p. 34, feb 2018.

[68] B. Paxton, R. Smolec, J. Schwab *et al.*, "Modules for Experiments in Stellar Astrophysics (MESA): Pulsating Variable Stars, Rotation, Convective Boundaries, and Energy Conservation," *The Astrophysical Journal Supplement Series*, vol. 243, no. 1, p. 10, Jul 2019.

[69] J. Choi, A. Dotter, C. Conroy, M. Cantiello, B. Paxton, and B. D. Johnson, "Mesa isochrones and stellar tracks (mist). i. solar-scaled models," *The Astrophysical Journal*, vol. 823, no. 2, p. 102, May 2016. [Online]. Available: http://dx.doi.org/10.3847/0004-637X/823/2/102

[70] C. Aerts, J. Christensen-Dalsgaard, and D. W. Kurtz, *Asteroseismology*. Springer, 2010.

[71] D. O. Gough, "Linear adiabatic stellar pulsation." in *Astrophysical Fluid Dynamics - Les Houches 1987*, Jan. 1993, pp. 399–560.

[72] T. G. Cowling, "The non-radial oscillations of polytropic stars," *Monthly Notices of the Royal Astronomical Society*, vol. 101, p. 367, Jan. 1941.

[73] J. Christensen-Dalsgaard, V. Silva Aguirre, S. Cassisi, M. Miller Bertolami, A. Serenelli, D. Stello, A. Weiss, G. Angelou, C. Jiang, Y. Lebreton, and et al., "The aarhus red giants challenge," *Astronomy & Astrophysics*, vol. 635, p. A165, Mar 2020. [Online]. Available: http://dx.doi.org/10.1051/0004-6361/201936766

[74] H. Kjeldsen and T. R. Bedding, "Amplitudes of stellar oscillations: the implications for asteroseismology." *Astronomy & Astrophysics*, vol. 293, pp. 87–106, Jan. 1995.

[75] S. Hekker and A. Mazumdar, "Solar-like oscillations in subgiant and red-giant stars: mixed modes," *Proceedings of the International Astronomical Union*, vol. 9, no. S301, p. 325–331, Aug 2013. [Online]. Available: http://dx.doi.org/10.1017/S1743921313014531

[76] N. Gai, Y. Tang, P. Yu, and X. Dou, "Asteroseismic diagram for subgiants and red giants," *The Astrophysical Journal*, vol. 836, no. 1, p. 3, feb 2017. [Online]. Available: https://doi.org/10.3847%2F1538-4357%2F836%2F1%2F3

[77] T. Appourchaux *et al.*, "Oscillation mode frequencies of 61 main-sequence and subgiant stars observed by kepler," *Astronomy & Astrophysics*, vol. 543, p. A54, Jun 2012. [Online]. Available: http://dx.doi.org/10.1051/0004-6361/201218948

[78] M.-A. Dupret *et al.*, "Theoretical amplitudes and lifetimes of non-radial solar-like oscillations in red giants*," *A&A*, vol. 506, no. 1, pp. 57–67, 2009. [Online]. Available: https://doi.org/10.1051/0004-6361/200911713

[79] M. Grosjean, M.-A. Dupret, K. Belkacem *et al.*, "Theoretical power spectra of mixed modes in low-mass red giant stars," *Astronomy & Astrophysics*, vol. 572, p. A11, Nov 2014. [Online]. Available: http://dx.doi.org/10.1051/0004-6361/201423827

[80] M. Tassoul, “Asymptotic approximations for stellar nonradial pulsations.” *The Astrophysical Journal*, vol. 43, pp. 469–490, Aug. 1980.

[81] I. Lopes and S. Turck-Chieze, “The second order asymptotic theory for the solar and stellar low degree acoustic mode predictions,” *Astronomy and Astrophysics*, vol. 290, pp. 845–860, Oct. 1994.

[82] H. O. Floranes, J. Christensen-Dalsgaard, and M. J. Thompson, “The use of frequency-separation ratios for asteroseismology,” *Monthly Notices of the Royal Astronomical Society*, vol. 356, no. 2, pp. 671–679, 01 2005. [Online]. Available: https://doi.org/10.1111/j.1365-2966.2004.08487.x

[83] I. W. Roxburgh and S. V. Vorontsov, “The ratio of small to large separations of acoustic oscillations as a diagnostic of the interior of solar-like stars,” *A&A*, vol. 411, no. 2, pp. 215–220, 2003. [Online]. Available: https://doi.org/10.1051/0004-6361:20031318

[84] R. Catena and P. Ullio, “A novel determination of the local dark matter density,” *Journal of Cosmology and Astroparticle Physics*, vol. 2010, no. 08, p. 004–004, Aug 2010. [Online]. Available: http://dx.doi.org/10.1088/1475-7516/2010/08/004

[85] A. Gould, “Resonant Enhancements in Weakly Interacting Massive Particle Capture by the Earth,” *Astrophysical Journal*, vol. 321, p. 571, Oct. 1987.

[86] A. R. Zentner, “High-energy neutrinos from dark matter particle self-capture within the sun,” *Physical Review D*, vol. 80, no. 6, Sep 2009. [Online]. Available: http://dx.doi.org/10.1103/PhysRevD.80.063501

[87] R. L. Gilliland, J. Faulkner, W. H. Press, and D. N. Spergel, “Solar Models with Energy Transport by Weakly Interacting Particles,” *The Astrophysical Journal*, vol. 306, p. 703, Jul. 1986.

[88] A. Gould and G. Raffelt, “Thermal Conduction by Massive Particles,” *The Astrophysical Journal*, vol. 352, p. 654, Apr. 1990.

[89] D. N. Spergel and W. H. Press, “Effect of hypothetical, weakly interacting, massive particles on energy transport in the solar interior,” *The Astrophysical Journal*, vol. 294, pp. 663–673, Jul. 1985.

[90] A. Gould and G. Raffelt, “Cosmion Energy Transfer in Stars: The Knudsen Limit,” *Astrophysical Journal*, vol. 352, p. 669, Apr. 1990.

[91] A. Renzini, “Effects of cosmions in the sun and in globular cluster stars,” *Astronomy and Astrophysics*, vol. 171, no. 1-2, p. 121, Jan. 1987. [Online]. Available: https://ui.adsabs.harvard.edu/abs/1987A&A...171..121R

[92] A. Bouquet and P. Salati, “Dark matter and the suppression of stellar core convection,” *The Astrophysical Journal*, vol. 284-288, 1989. [Online]. Available: http://adsabs.harvard.edu/full/1989ApJ...346..284B

[93] J. Casanellas, I. Brandão, and Y. Lebreton, “Stellar convective cores as dark matter probes,” *Phys. Rev. D*, vol. 91, p. 103535, May 2015. [Online]. Available: https://link.aps.org/doi/10.1103/PhysRevD.91.103535

[94] J. Lopes and I. Lopes, “Asymmetric dark matter imprint on low-mass main-sequence stars in the milky way nuclear star cluster,” *The Astrophysical Journal*, vol. 879, no. 1, p. 50, Jul 2019. [Online]. Available: http://dx.doi.org/10.3847/1538-4357/ab2392

[95] J. Molenda-Żakowicz *et al.*, “Atmospheric parameters of 169 f-, g-, k- and m-type stars in the kepler field,” *Monthly Notices of the Royal Astronomical Society*, vol. 434, no. 2, p. 1422–1434, Jul 2013. [Online]. Available: http://dx.doi.org/10.1093/mnras/stt1095

[96] T. S. Metcalfe *et al.*, “PROPERTIES OF 42 SOLAR-TYPE KEPLER TARGETS FROM THE ASTEROSEISMIC MODELING PORTAL,” *The Astrophysical Journal Supplement Series*, vol. 214, no. 2, p. 27, oct 2014. [Online]. Available: https://doi.org/10.1088%2F0067-0049%2F214%2F2%2F27

[97] T. S. Metcalfe *et al.*, “Asteroseismology of the Solar Analogs 16 Cyg A and B from Kepler Observations,” *The Astrophysical Journal Letters*, vol. 748, no. 1, p. L10, Mar. 2012.

[98] W. J. Chaplin *et al.*, “Asteroseismic fundamental properties of solar-type stars observed by the nasa kepler mission,” *The Astrophysical Journal Supplement Series*, vol. 210, no. 1, p. 1, Dec 2013. [Online]. Available: http://dx.doi.org/10.1088/0067-0049/210/1/1

[99] T. Metcalfe, “AMP | Run Details | KIC 8228742,” May 2014, accessed 13-May-2020. [Online]. Available: https://amp.wdrc.org/browse/simulation/648/

[100] J. N. Bahcall, A. M. Serenelli, and S. Basu, “10,000 standard solar models: A monte carlo simulation,” *The Astrophysical Journal Supplement Series*, vol. 165, no. 1, p. 400–431, Jul 2006. [Online]. Available: http://dx.doi.org/10.1086/504043

[101] N. Grevesse and A. J. Sauval, “Standard Solar Composition,” *Space Sci. Rev.*, vol. 85, pp. 161–174, May 1998.

[102] S. Deheuvels, I. Brandão, V. Silva Aguirre *et al.*, “Measuring the extent of convective cores in low-mass stars usingkeplerdata: toward a calibration of core overshooting,” *Astronomy & Astrophysics*, vol. 589, p. A93, Apr 2016. [Online]. Available: http://dx.doi.org/10.1051/0004-6361/201527967

[103] J. A. Nelder and R. Mead, “A Simplex Method for Function Minimization,” *The Computer Journal*, vol. 7, no. 4, pp. 308–313, 01 1965. [Online]. Available: https://doi.org/10.1093/comjnl/7.4.308

[104] R. H. D. Townsend and S. A. Teitler, “GYRE: an open-source stellar oscillation code based on a new Magnus Multiple Shooting scheme,” *Monthly Notices of the Royal Astronomical Society*, vol. 435, pp. 3406–3418, nov 2013.

[105] R. H. D. Townsend, J. Goldstein, and E. G. Zweibel, “Angular momentum transport by heat-driven g-modes in slowly pulsating B stars,” *Monthly Notices of the Royal Astronomical Society*, vol. 475, pp. 879–893, Mar. 2018.

[106] E. P. Bellinger, S. Hekker, G. C. Angelou, A. Stokholm, and S. Basu, “Stellar ages, masses, and radii from asteroseismic modeling are robust to systematic errors in spectroscopy,” *Astronomy & Astrophysics*, vol. 622, p. A130, Feb 2019. [Online]. Available: http://dx.doi.org/10.1051/0004-6361/201834461

[107] K. Verma *et al.*, “Helium abundance in a sample of cool stars: measurements from asteroseismology,” *Monthly Notices of the Royal Astronomical Society*, vol. 483, no. 4, pp. 4678–4694, 12 2018. [Online]. Available: https://doi.org/10.1093/mnras/sty3374

[108] J. R. Hurley, O. R. Pols, and C. A. Tout, “Comprehensive analytic formulae for stellar evolution as a function of mass and metallicity,” *Monthly Notices of the Royal Astronomical Society*, vol. 315, no. 3, p. 543–569, Jul 2000. [Online]. Available: http://dx.doi.org/10.1046/j.1365-8711.2000.03426.x

[109] M. Salaris and S. Cassisi, *The Hydrogen Burning Phase*. John Wiley & Sons, Ltd, 2006, ch. 5, pp. 117–159. [Online]. Available: https://onlinelibrary.wiley.com/doi/abs/10.1002/0470033452.ch5

[110] ——, *The Helium Burning Phase*. John Wiley & Sons, Ltd, 2006, ch. 6, pp. 161–186. [Online]. Available: https://onlinelibrary.wiley.com/doi/abs/10.1002/0470033452.ch6

[111] ——, *The Advanced Evolutionary Phases*. John Wiley & Sons, Ltd, 2006, ch. 7, pp. 187–237. [Online]. Available: https://onlinelibrary.wiley.com/doi/abs/10.1002/0470033452.ch7

[112] I. P. Lopes and J. Silk, “Solar neutrinos: Probing the quasi-isothermal solar core produced by supersymmetric dark matter particles,” *Physical Review Letters*, vol. 88, no. 15, Apr 2002. [Online]. Available: http://dx.doi.org/10.1103/PhysRevLett.88.151303

[113] E. Aprile *et al.*, “Xenon100 dark matter results from a combination of 477 live days,” *Physical Review D*, vol. 94, no. 12, Dec 2016. [Online]. Available: http://dx.doi.org/10.1103/PhysRevD.94.122001

[114] S. Archambault *et al.*, "Constraints on low-mass wimp interactions on 19f from picasso," *Physics Letters B*, vol. 711, no. 2, p. 153–161, May 2012. [Online]. Available: http://dx.doi.org/10.1016/j.physletb.2012.03.078

[115] B. Mosser *et al.*, "Mixed modes in red giants: a window on stellar evolution," *Astronomy and Astrophysics*, vol. 572, p. L5, Dec. 2014.

[116] A. Nuñez-Castiñeyra, E. Nezri, and V. Bertin, "Dark matter capture by the sun: revisiting velocity distribution uncertainties," *Journal of Cosmology and Astroparticle Physics*, vol. 2019, no. 12, p. 043–043, Dec 2019. [Online]. Available: http://dx.doi.org/10.1088/1475-7516/2019/12/043

A

Article

In this appendix we present the scientific paper currently in review for publication in the Monthly Notices of the Royal Astronomical Society that results from the work discussed in this thesis, namely in Chapters 5 and 6.

MONTHLY NOTICES of the Royal Astronomical Society

On asymmetric dark matter constraints from the asteroseismology of a subgiant star

Journal:	*Monthly Notices of the Royal Astronomical Society*
Manuscript ID	Draft
Manuscript type:	Main Journal
Date Submitted by the Author:	n/a
Complete List of Authors:	Rato, João; Instituto Superior Técnico Departamento de Física, Physics Lopes, José; CENTRA, Physics Lopes, Ilidio; Instituto Superior Tecnico, Universidade de Lisboa, Fisica
Keywords:	asteroseismology < Physical Data and Processes, stars: evolution < Stars, stars: oscillations (including pulsations) < Stars, (cosmology:) dark matter < Cosmology

MNRAS **000**, 1–10 (2020) Preprint 20 December 2020 Compiled using MNRAS LATEX style file v3.0

On asymmetric dark matter constraints from the asteroseismology of a subgiant star

João Rato,[1]★ José Lopes[1] and Ilídio Lopes[1]
[1]*Centro de Astrofísica e Gravitação - CENTRA, Departamento de Física, Instituto Superior Técnico - IST, Universidade de Lisboa - UL, Av. Rovisco Pais 1, P-1049-001 Lisboa, Portugal*

Accepted XXX. Received YYY; in original form ZZZ

ABSTRACT

The asteroseismic modelling of solar-like stars has proved to be valuable in the search for dark matter constraints. In this work we study for the first time the influence of asymmetric dark matter (ADM) in the evolution of a subgiant star (KIC 8228742) by direct comparison with observational data. Both spectroscopic and seismic data are analysed with a new approach to the stellar calibration method, in which dark matter properties can also be considered as free inputs. In another phase of this study, a calibrated standard stellar model (without DM) is used as the benchmark for DM models. We find that the latter models consistently outperform the former for $10^{-40} \leqslant \sigma_{\rm SD} < 10^{-38}$ cm^2, hinting that the presence of asymmetric dark matter in stars of this type does not go against observations. Moreover, we show that stellar seismology allows us to suggest exclusion limits that complement the constraints set by direct detection experiments. Different seismic observables are proposed to study DM properties and $\Delta\Pi_\ell$ is found to be the most reliable, having the potential to build future DM exclusion diagrams. This new methodology can be a powerful tool in the analysis of the data coming from the next generation of asteroseismic missions.

Key words: asteroseismology – stars: evolution – (stars:) subgiants – stars: oscillations (including pulsations) – (cosmology:) dark matter

1 INTRODUCTION

Since the dark matter (DM) hypothesis arose from the discrepancy between theory and the observation of the galaxies' rotation curves (Rubin et al. 1976), direct detection experiments have been conducted in the hope of finding these elusive particles (e.g., Bertone 2010; Undagoitia & Rauch 2015, and references therein). Although some constraints on the mass and cross section of interactions of DM particles with baryons have been set (e.g., Beringer et al. 2012), no detection has yet been confirmed (e.g., Schumann 2019).

Weakly Interacting Massive Particles (WIMPs) stand out as one of the primary candidates for DM (Bertone et al. 2005; Bertone & Hooper 2018). These particles have a non-negligible scattering cross section with baryons which is usually treated in two separate components: spin-dependent, $\sigma_{\rm SD}$, and spin-independent interactions, $\sigma_{\rm SI}$ (Barger et al. 2008). For WIMP masses around $m_\chi \simeq 5$ GeV, recent upper limiting constraints on $\sigma_{\rm SD}$ (WIMP-proton interactions) have been placed at slightly below 10^{-37} cm^2 by PICASSO (Behnke et al. 2017) and at around 10^{-39} cm^2 by PICO-60 (Amole et al. 2019). The XENON-100 experiment (Aprile et al. 2016) placed a limit for $\sigma_{\rm SD}$ at $\sim 10^{-36}$ cm^2 for $m_\chi \sim 9$ GeV. For $\sigma_{\rm SI}$ (WIMP-nucleon interactions) the upper limits were found to be at around 5×10^{-41} cm^2 (from both PICASSO and PICO-60).

In this study, we consider WIMPs in an asymmetric dark matter (ADM) scenario, in which the DM annihilation cross section is negligible. Much like baryons in baryogenesis, dark matter asymmetry is hypothesised to have been produced in a process often called darkogenesis (e.g., Shelton & Zurek 2010). Thus, in the ADM framework, the DM and anti-DM densities are unbalanced and make the present-day DM self-annihilation negligible. This choice of framework is mainly interesting in the standpoint of the DM influence on stars: since DM self-annihilation does not occur, the number of DM particles inside a star will naturally be larger than it would be otherwise, making the star more sensible to its effects, which allows for a better study of DM phenomena.

Besides the already mentioned direct detection achievements, stars have also been used in the search for DM. These endeavours have ranged from the study of solar models affected by DM (e.g., Lopes & Silk 2010; Taoso et al. 2010) to asteroseismic analysis (e.g., Lopes et al. 2002a; Casanellas & Lopes 2013; Lopes et al. 2019) also including neutrino flux constraints (e.g., Lopes et al. 2002b; Turck-Chièze et al. 2012). Using stars and stellar models as an object of study of DM also has its shortcomings, which are mostly inherited from standard stellar modelling. A notable example among these is the so-called solar composition problem. Standard solar models using the most recent photospheric abundances (AGSS09: Asplund et al. (2009)) as inputs present a contradictory prediction of the Sun's internal structure when compared to high-precision results from helioseismology (e.g., Christensen-Dalsgaard 2002; Bahcall et al. 2005). This discrepancy between predictions coming from spectroscopy and helioseismology renders the determination of stellar properties (such as the sound speed profile) through stellar modelling problematic and affects not only the modelling of the Sun but also other stars since they rely on solar inputs for some quantities, like the relative metal-

★ E-mail: jpedrorato@tecnico.ulisboa.pt

licity Z/X. In a recent discussion of this problem, Capelo & Lopes (2020) have shown that measuring neutrino fluxes from the CNO cycle with a precision that could be achieved by the next generation of experiments could help resolve this issue. While this problem can hinder the ability of using stellar modelling to probe DM properties, DM itself can also be an answer to the abundance problem since it introduces different physics in the interior of stars. Particularly, Lopes et al. (2014) proposed that the accretion of DM in the Sun's core could lead to a better agreement between helioseismic and neutrino data. In a follow up with a more detailed analysis, Vincent et al. (2015) show that the solar abundance problem could be solved by the presence of a light asymmetric dark matter particle.

Asteroseismology has particularly been thoroughly exploited in an attempt to find constraints for the properties of DM while using stars as laboratories (Casanellas & Lopes 2010). The premise is fairly straightforward: by analysing oscillation frequencies of stars we can extract valuable information of their interior structure. This is related to DM because the capture and subsequent accumulation of these particles via gravitational effects introduce an additional energy transport mechanism. This new phenomenology can naturally lead to changes in the structure of the star, which can be probed via asteroseismic diagnostics (e.g., Casanellas & Lopes 2010; Martins et al. 2017). Missions like CoRoT (Fridlund et al. 2006; Michel et al. 2008), *Kepler* (Borucki et al. 2010; Koch et al. 2010) and TESS (Ricker et al. 2014) have made progress in obtaining the oscillation frequencies of many main-sequence (MS), subgiant (SG) and red-giant (RG) stars with great precision, making it possible to study the asteroseismology of stars other than the Sun. To take full advantage of this diversity of data, seismic diagnostics can be formulated for several stars in different stages of evolution, broadening the spectre of potential DM laboratories. With the primary goal of discovering habitable extra-solar planets, the PLAnetary Transits and Oscillations of stars (PLATO) mission (Rauer et al. 2014), to be launched in 2026, will extend this effort and enable more precise studies by the determination of accurate stellar masses, radii, and ages from asterosesimic data. The oscillation frequency measurements are expected to improve in precision upon those of *Kepler* while also extending the catalogue to include brighter stars. Thus, this will enable the study of the effects of DM on the stellar structure with both greater precision and for a considerably larger number of stars.

In the following section we focus on the asteroseismology of SG stars and important quantities for describing stellar oscillations are introduced. We then describe the calibration methodology and the diagnostics used to infer on the quality of the calibrated models, in Section 3. In Section 4 we address the interactions between ADM and stars. Results are then shown in two separate parts. In Section 5 we calibrate a SG star with and without ADM presence, where the stellar inputs are treated as free parameters and are thus optimised to better fit the observational data. After that, in Section 6, we take on the work of the previous section by choosing the best no-DM model as benchmark to build a set of DM models with different properties and fixed standard stellar inputs. We then use the diagnostics defined in Section 3 to classify this set of models and enquire about constraints on the properties of ADM. Finally, conclusions and closing remarks are presented in the last section.

2 ASTEROSEISMOLOGY OF SUBGIANT STARS

The study of the impact of DM on the Sun and other MS sun-like stars using asteroseismology has allowed to constrain properties of different types of particle DM (e.g., Lopes et al. 2002a,b; Frandsen & Sarkar 2010; Lopes et al. 2019). In this work we focus on stars in a different stage of evolution – the subgiant phase. This stage follows the MS, i.e., after hydrogen burning ceases in the centre of the star and moves to a shell right above the helium ashes that compose the inert stellar core.

In particular, the object of our study is the subgiant KIC 8228742, a F9IV-V spectral type star (Molenda-Żakowicz et al. 2013) with a previously modelled mass of 1.27 $M_\odot$ (Metcalfe et al. 2014). Throughout this work, the observational constraints were taken from Chaplin et al. (2013) for the spectroscopic parameters and from Appourchaux et al. (2012) for the oscillation frequencies, as published in the Asteroseismic Modelling Portal (AMP) (Metcalfe 2014).

Despite the experimental advances made by the aforementioned missions, SG stars are more difficult to find than MS or giant stars since that stage has a relatively shorter lifetime. Another interesting aspect when studying the asteroseismology of SG stars is the lack of detected non-radial acoustic modes. Usually, SG and RGs' most visible oscillations are gravity-dominated mixed modes (Hekker & Mazumdar 2013; Gai et al. 2017): due to the rapid core contraction, the gravity (g-) and acoustic (p-) mode trapping cavities are closer to each other when the stars move off the MS, which results in the coupling of the acoustic and gravity modes. These are called mixed modes, which have p-mode characteristics in the convective stellar envelope and g-mode characteristics in the dense radiative stellar core. However, KIC 8228742 exhibits many simple modes (or pure acoustic p-modes) like the sun (Appourchaux et al. 2012). This is due to gravity-dominated mixed modes having lower amplitudes than pressure-dominated ones (Dupret et al. 2009; Grosjean et al. 2014), so observing them is not always easy. As such, we first direct our focus to the acoustic simple modes.

Since acoustic waves of low spherical degree (ℓ) propagate throughout the entire star, their frequencies encode information of the whole stellar structure, spanning from the star's core to its surface. Thus, as stated before, obtaining them is pivotal to understand the underlying physics of the internal structure of a star. Naturally, quantities stemming from these frequencies can be defined to better probe the stellar structure. The large frequency separation is defined as (e.g., Tassoul 1980; Lopes & Turck-Chieze 1994)

$$\Delta\nu_{n,\ell} = \nu_{n,\ell} - \nu_{n-1,\ell} \simeq \left(2\int_0^R \frac{dr}{c(r)}\right)^{-1}, \tag{1}$$

where $\nu_{n,\ell}$ denotes the frequency of the mode with radial order n and spherical degree ℓ, r is the radial coordinate, R is the total radius of the star and $c(r)$ represents the sound speed profile inside the star. Thus, $\Delta\nu_{n,\ell}$ is deeply related to the sound speed profile of a star and is useful as a global measure of that quantity (Floranes et al. 2005).

Additionally, a small frequency separation can also be defined as (Tassoul 1980; Lopes & Turck-Chieze 1994)

$$\delta\nu_{n,\ell} = \nu_{n,\ell} - \nu_{n-1,\ell+2}, \tag{2}$$

which is particularly sensitive to the thermodynamic conditions of the stellar core.

As discussed before, subgiant and giant stars often exhibit gravity dominated modes. From these, the period separation $\Delta\Pi_\ell$ is a useful quantity to extract and, in the asymptotic limit, it is given by (Tassoul 1980)

$$\Delta\Pi_\ell = \frac{2\pi^2}{\sqrt{\ell(\ell+1)}}\left(\int_{r_1}^{r_2} N\frac{dr}{r}\right)^{-1} = \frac{\Pi_0}{\sqrt{\ell(\ell+1)}}, \tag{3}$$

where N is the Brunt-Väisälä (or buoyancy) frequency and r_1 and r_2 correspond to the boundaries of the g-mode cavity which

extends through the radiative region of the star. Since, in SG stars, r_1 coincides with the interface between the inner convective zone (if there is one) and the radiative region, it follows that $\Delta\Pi_\ell$ directly relates to the size of the convective core.

3 CALIBRATION AND DIAGNOSTIC METHODS

3.1 Observables and calibration

Stellar modelling has been extremely helpful in allowing us to better understand the physics at play inside stars. Modules for Experiments in Stellar Astrophysics (MESA) (Paxton et al. 2011, 2013, 2015, 2018, 2019), an open-source 1-D stellar evolution code, is a powerful tool in this regard. By combining various modules that aim to precisely describe different stellar phenomenology, MESA allows the user to model a wide variety of stars, given a set of stellar parameters as inputs.

In our work, we take advantage of the full capabilities of MESA, with special emphasis on the *astero* module (Paxton et al. 2013), as it governs calibrations. Using this module as a starting point, we produce a high precision stellar model calibration process which allows for both seismic and spectroscopic calibrations by taking as inputs $\{M,\ Y_i,\ [\mathrm{Fe/H}]_i,\ \alpha,\ f_{\mathrm{ov}}\}$ (stellar mass, initial helium abundance, initial metallicity, mixing-length parameter and overshooting parameter, respectively) and then producing an evolutionary model that is compared head-to-head with observations. This comparison is accomplished by computing a χ^2_{star} value that has weighted contributions from both spectroscopic (χ^2_{spec}) and seismic (χ^2_{seis}) observables. In this work we use the default 2/3 weight on the seismic contribution and 1/3 on the spectroscopic counterpart, i.e., $\chi^2_{\mathrm{star}} = 1/3\chi^2_{\mathrm{spec}} + 2/3\chi^2_{\mathrm{seis}}$ (Metcalfe et al. 2012; Paxton et al. 2013). The diagnostics χ^2_{spec} and χ^2_{seis} are quadratic deviations from the spectroscopic and seismic observational data, respectively, with their uncertainties taken into account:

$$\chi^2_{\mathrm{spec/seis}} = \frac{1}{N}\sum_{i=1}^{N}\left(\frac{X_i^{\mathrm{mod}} - X_i^{\mathrm{obs}}}{\sigma_{X_i}}\right)^2, \tag{4}$$

where N is the number of parameters, X_i^{mod} and X_i^{obs} are the stellar model and observed values of the i^{th} parameter, respectively, with σ_{X_i} being the observational uncertainty. The observational parameters used in χ^2_{spec} are $\{L, T_{\mathrm{eff}}, [\mathrm{Fe/H}]\} = \{4.57 \pm 1.45\ \mathrm{L}_\odot, 6042 \pm 84\ \mathrm{K}, -0.14 \pm 0.09\}$ (luminosity, effective temperature and metallicity), and in χ^2_{seis} is $\{\Delta\nu\} = \{62.1 \pm 0.13\ \mu\mathrm{Hz}\}$.

As for the calibration procedure, we use a method that is commonly used throughout the literature (e.g., Deheuvels et al. 2016; Capelo & Lopes 2020) which relies on minimising χ^2_{star}. This is achieved through an automatised optimisation process which uses a direct search method – the downhill simplex algorithm (Nelder & Mead 1965) – to find the optimal set of inputs that produce the group of outputs $\{L, T_{\mathrm{eff}}, [\mathrm{Fe/H}], \Delta\nu\}$ that are closest to their observed counterparts. To account for DM effects, we extend the standard calibration process to also include the relevant DM parameters as inputs, which extends the input set to $\{M, Y_i, [\mathrm{Fe/H}]_i, \alpha, f_{\mathrm{ov}}\ m_\chi, \sigma_{\mathrm{SD}}\}$ while maintaining the same outputs and comparison strategy.

3.2 Seismic ratio diagnostics

While ensuring that a model is consistent with observations in terms of spectroscopy is valuable in itself, in most cases these parameters do not fully mirror what is happening in the stellar interior. These are the situations where thoroughly analysing the oscillation frequencies of a star becomes a powerful diagnostic tool.

To build upon the calibration process described in the last section, we resort to a more detailed seismic diagnostic of the stellar interior based on the observational frequencies $\nu_{n,\ell}$. Since in stars other than the Sun it is difficult to observe modes with $\ell > 2$ due to partial cancellation (e.g., Aerts et al. 2010), we decide to use the ratio of the small to large separations r_{02},

$$r_{02}(n) = \frac{\delta\nu_{n,0}}{\Delta\nu_{n,1}}. \tag{5}$$

Equation (5) aims to give better insights on the stellar core – where the most significant DM influence is expected – since the near-surface effects that highly affect individual frequency separations nearly cancel out by computing this ratio. This means that $r_{02}(n)$ is independent of the structure of the outer layers of a star and thus works as a probe into the stellar interior (Roxburgh & Vorontsov 2003). Conveniently, we define a new χ^2 to assess the seismic quality of a given stellar model in terms of the r_{02} ratio:

$$\chi^2_{r_{02}} = \sum_{n=14}^{22}\left[\frac{r_{02}^{\mathrm{obs}}(n) - r_{02}^{\mathrm{model}}(n)}{\sigma_{r_{02}^{\mathrm{obs}}}}\right]^2, \tag{6}$$

where $r_{02}^{\mathrm{obs}}(n)$ and $r_{02}^{\mathrm{model}}(n)$ represent the ratio defined in eq. (5) computed using both the observed and model frequencies, respectively, while $\sigma_{r_{02}^{\mathrm{obs}}}$ stands for the observed uncertainty which is computed through error propagation from the individual frequencies' uncertainties. For the star considered here, we can observe 32 modes with $\ell \leqslant 2$ and n running from 14 to 22, amounting to 9 different instances of r_{02} in the sum defined in eq. (6). The resulting value of $\chi^2_{r_{02}}$ along side the other mentioned diagnostics will provide the classification of the models.

One important point to bear in mind is that $\chi^2_{r_{02}}$ is used as an additional diagnostic, independent from the original calibration process. This is mainly because it creates a robust two-step rejection method and also due to computational time constraints. Thus, only χ^2_{spec} and χ^2_{seis} are computed at each step of the calibration process. It should be noted that while χ^2_{seis} does imply the computation of the large frequency separation, this is accomplished by taking into account the approximation in eq. (1) instead of the actual computation of the oscillation modes, and as such, it does not represent the time-consuming effort that r_{02} would. After the calibration process is completed the r_{02} ratios are then computed for the accepted models of the previous step (usually by defining a cut-off χ^2_{star}).

4 ASYMMETRIC DARK MATTER INTERACTIONS WITH A STAR

In the case of ADM, the interactions between DM particles and a given star are limited to capture, evaporation and energy transport, all due to scattering with the baryonic matter that constitutes the stellar plasma. For the models considered in this work, it is safe to neglect evaporation – the process in which DM particles that were already trapped inside the star scatter to velocities larger than the local escape velocity – since it has been found that, for sun-like stars, the DM mass above which evaporation is negligible is close to 3.3 GeV (e.g., Gould 1990; Kouvaris 2015), and here we explore larger mass values of ADM particles. Additionally, as stated before, the annihilation cross section of ADM particles is negligible and, thus, the process that defines the number of dark matter particles inside the star is the capture. This process, which consists in the

gravitational trapping of DM particles from the galactic halo, is mainly defined by the DM mass, the DM–nucleon cross-section, the gravitational potential of the star and the local DM density. In our case, KIC 8228742 is just 0.17 kpc away from the Sun, therefore we assume a DM density corresponding to what is found in the solar neighbourhood, $\rho_\chi = 0.38$ GeV/cm^3 (Catena & Ullio 2010).

After accumulating and thermalising within the star, captured particles interact with baryons in the stellar interior. These scatterings will create an additional mechanism for transporting energy, adding an extra term to the standard equation of energy transport in stars. In most model-independent DM studies it is usual to assume the already mentioned σ_{SI} and σ_{SD} effective constant cross sections to describe the ADM particles' interactions with the baryons in the stellar plasma. In this work, we focus on SD interactions, which, in the case of solar-like stars, correspond mostly to scatterings with hydrogen. Previous studies regarding the impact of ADM in the Sun showed that due to the flux of energy carried outwards from the innermost regions of the star by ADM particles with a mass of 7 GeV and $\sigma_{SD} \simeq 10^{-36}$ cm^2, the stellar core exhibited a decrease in temperature when compared to the standard case, while the reverse happened with the (baryonic) density (Taoso et al. 2010). This effect, whose intensity is naturally related to the interaction cross-section, is in fact counter intuitive given that any transport of energy away from the core should lead to its contraction, which would in turn lead to an increase in temperature. This however is not the case, since the energy transported away by the ADM particles is of a higher order of magnitude than the one released by the core contraction, countering its heating effects.

Another well-known consequence of the extra energy transport by DM is the suppression of convection – generally in the centre of the star – which was firstly proposed by Renzini (1987) and Bouquet & Salati (1989) and later studied by Casanellas & Lopes (2013) and Casanellas et al. (2015), particularly for stars with masses between 1.1 and 1.3 $M_\odot$. This suppression is directly related to the decrease in the temperature gradient, which prevents the arise of convection as it would in cases where there is no energy transport by DM.

In this work, to study the effects of the interactions between ADM and the stellar plasma during the evolution of star KIC 8228742 we modified the MESA stellar evolution code to include the processes described above, namely capture and energy transport. We consider DM capture as described by Gould (1987), and energy transport is computed taking into account the numerical results by Gould & Raffelt (1990). During the evolution, the capture rate is computed at each time step, and total number of ADM particles inside the star is updated accordingly. This information is then used to compute the extra energy term, which is fed to the usual set of differential equations that govern stellar evolution.

5 STELLAR MODELS

5.1 Standard stellar model of the subgiant KIC 8228742

Using the calibration methods described in Section 3 with all five inputs $\{M, Y_i, [\mathrm{Fe/H}]_i, \alpha, f_{ov}\}$ as free parameters, we obtain several stellar models with no dark matter interactions. From these models, the best one in terms of χ^2_{star} was chosen as the benchmark model for future analysis and is henceforth also referred to as Standard Subgiant (SSG) model. The resulting parameters are shown in the first row of Table 1, where $\chi^2_{r_{02}}$ is also included. It should be noted that directly comparing χ^2_{star} with $\chi^2_{r_{02}}$ is misleading, as their definitions and normalisation are different.

In comparison with other models found in the literature, the SSG model's parameters fall well within the limits proposed in most works (e.g., Bellinger et al. 2019) with the exception of the initial metallicity and mixing-length parameters found in Verma et al. (2018). This does not amount to a large discrepancy and thus the model is accepted to be a good reference model. Additionally, the SSG model exhibits a convective core during the MS that extends up to 0.065 $R_\odot$ and showcases a helium core (surrounded by a hydrogen shell) at the end of the evolution (See Fig. 3), which is the expected structure for stars in this stage of evolution, with these values of stellar mass (e.g., Hurley et al. 2000; Salaris & Cassisi 2006a,b,c).

5.2 Comparison of dark matter models with a standard stellar model

A valuable asset of the improved calibration method considered in this work is that it allows for the DM properties to be treated as free parameters in the calibration. In this sense, we allow the algorithm to vary the values of the ADM particles' mass in between 4 and 12 GeV and the spin-dependent cross section in between 10^{-40} and 10^{-35} cm^2 since this is both included in the region of the parameter space currently being probed by DM direct detection experiments and also the region that produces greater effects on stars (e.g., Casanellas & Lopes 2013; Martins et al. 2017).

As before, the standard stellar inputs shown in the previous section were treated as free parameters, so it is expected that the set of optimal parameters is different than the values shown in the first row of Table 1. Taking into account the DM phenomenology described in Section 4, we carried out the optimisation process, from which we retrieved the best model (i.e., with the lowest χ^2_{star}). This model (DM Calib) found an optimal dark matter particle with a mass of $m_\chi = 9.12$ GeV and a spin-dependent interaction cross section of $\sigma_{SD} = 2.32 \times 10^{-36}$ cm^2, which is within the limits of the XENON-100 experiment mentioned in Section 1. The fact that this model is calibrated, by definition, means that it is bound to be in agreement with the corresponding observations. However, it is interesting to note that the best agreement – within the considered parameter range – occurs for the aforementioned values of m_χ and σ_{SD}, even though they fall inside the excluded area of other more recent experiments (e.g., Amole et al. 2019).

As expected, Fig. 1 shows that the optimal inputs changed with respect to the parameters obtained in the SSG model, some more drastically than others, as is the case of the initial Helium abundance Y_i and the mixing-length parameter α. In terms of model outputs, the inclusion of the DM effects and parameters in the calibration process made the stellar age change in around 12% while the most noticeable difference is the 16% increase in the logarithm of the central density, which translates to a factor of around 2.5 in the central density itself. This discrepancy is best viewed by comparing the respective profiles shown in Fig. 2, where it is visible that the star forms an isothermal core at a lower temperature, which is consistent with other results for the Sun and other sun-like stars (e.g., Lopes & Silk 2002; Taoso et al. 2010). Such is also the case of the baryonic density profile, which displays an increase in the innermost regions of the star when considering ADM capture and interactions. One important aspect to remember is the fact that, by only considering spin-dependent couplings, the DM-stellar matter scatterings are practically reduced to DM-hydrogen interactions. This means that, in fact, we neglect most of the DM energy transport that occurs during the actual SG phase, given that in these stars the region inhabited by ADM particles,

Table 1. KIC 8228742 models. The 4 bottom models were calibrated with fixed pairs of (m_χ, $\sigma_{\rm SD}$) while DM Calib allowed the two parameters to vary. The first 2 columns are the DM parameters and the 3 following columns are some of the input parameters of the calibration. Both $f_{\rm ov}$ and $[{\rm Fe/H}]_i$ are omitted because they share similar values between all models ($f_{\rm ov} \simeq 1.62 \times 10^{-2}$ and $[{\rm Fe/H}]_i \simeq -0.14$). The following columns correspond (from left to right) to: age, luminosity, total radius and the logarithms of the central temperature and central density. The χ^2 used in calibration and diagnostics are also displayed. Finally, the period spacing is shown for $\ell = 1$ and $\ell = 2$.

Model	m_χ (GeV)	$\sigma_{\rm SD}$ (10^{-36} cm^2)	M ($M_\odot$)	Y_i	α	age (Gyrs)	L ($L_\odot$)	R ($R_\odot$)	$\log\left(\frac{T_c}{1\,\rm K}\right)$	$\log\left(\frac{\rho_c}{1\ \rm gcm^{-3}}\right)$	$\chi^2_{\rm star}$ (10^{-3})	$\chi^2_{r_{02}}$	$\Delta\Pi_1$ (s)	$\Delta\Pi_2$ (s)
SSG	-	-	1.2565	0.244	1.403	4.52	4.254	1.884	7.42	2.53	5.735	27.8	1636	945
DM Calib	9.12	2.32	1.2517	0.227	1.467	5.03	4.270	1.886	7.32	2.95	5.287	29.2	548	316
DM A	6.00	10^{-3}	1.2580	0.244	1.406	4.50	4.263	1.884	7.42	2.53	5.586	26.7	1642	948
DM B	6.00	10^{-1}	1.2591	0.243	1.407	4.50	4.264	1.885	7.42	2.53	5.486	37.8	1644	949
DM C	5.00[a]	1	1.2516	0.227	1.480	5.06	4.268	1.887	7.32	2.96	5.245	20.0	543	313
DM D	6.00	10	1.2590	0.229	1.403	4.76	4.339	1.884	7.32	2.96	17.879	64.3	564	326

[a] A slightly different mass value was used in this case due to model convergence limitations.

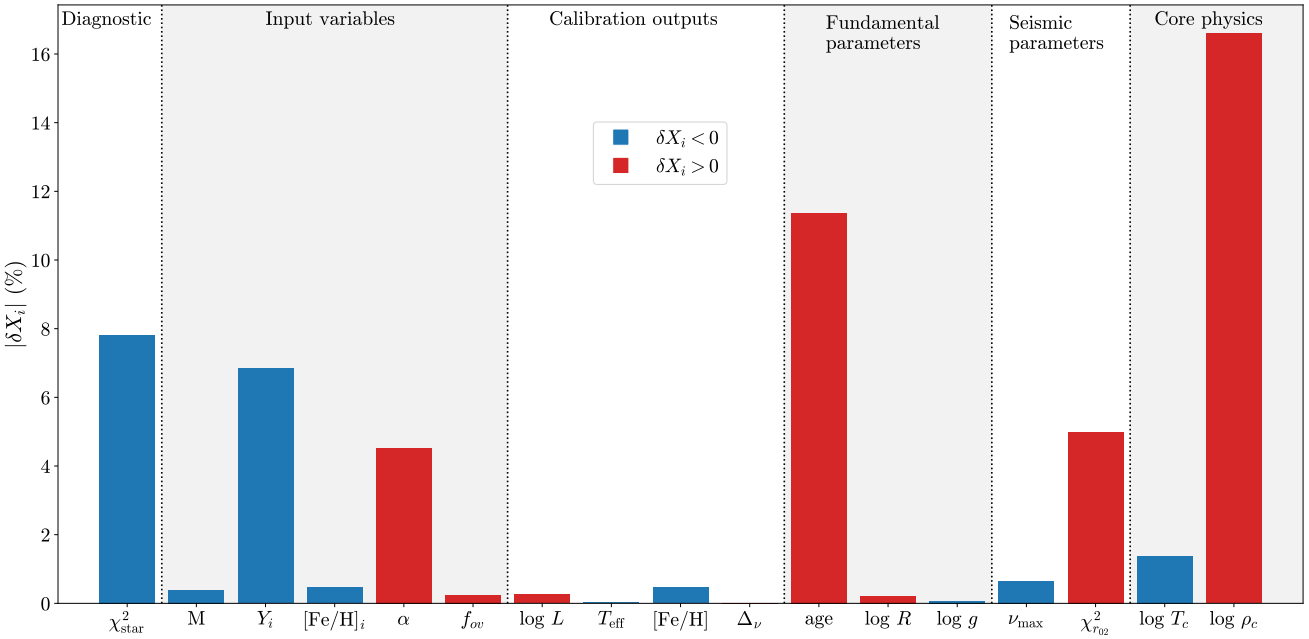

Figure 1. Direct comparison of the DM Calib and Standard Subgiant models: the percentage variations were recorded relatively to the SSG model (see Table 1). As some variations are negative, we use blue for negative values and red otherwise.

i.e., the core, is mostly devoid of hydrogen. Thus, the DM signatures shown here – and the resulting departures from the standard non-DM models – are in fact a consequence of DM interactions that occurred mainly during the MS. Therefore, the comparison with different studies in the literature about similar effects in MS stars is reasonable since we are looking at the remnants of ADM interactions during the MS phase through a SG star. It should also be noted that although we are not comparing the SSG and DM Calib models at the same age (nor do they have the same standard stellar inputs), as is the usual practice, the comparison is still of interest (and thus this effect is still expected) since it is made between two calibrated models of the same star, meaning that they are spectroscopically similar. Nevertheless, one could argue that the change in the star's age could be the driving factor of the differences found between the two models. But, in fact, that is not the case: by analysing the same profiles of the two models for the same age (for example, at t = 4.52 Gyrs, see Table 1) we confirm that the two distinct regimes are still present and identical to what is seen in Figs. 2 & 3.

Unlike the Standard model of this star, DM Calib did not exhibit a convective core. In fact, the suppression of the convective core is a recurring feature of DM influence on stars as mentioned in Section 4. Furthermore, by studying the star chemical profiles (Fig. 3) we see that while hydrogen is completely exhausted in the inner regions of the stellar core, there is a smooth increase in the hydrogen abundance (vice-versa for helium), instead of the sharp variation which is usual in stars with $M \simeq 1.3\ M_\odot$.

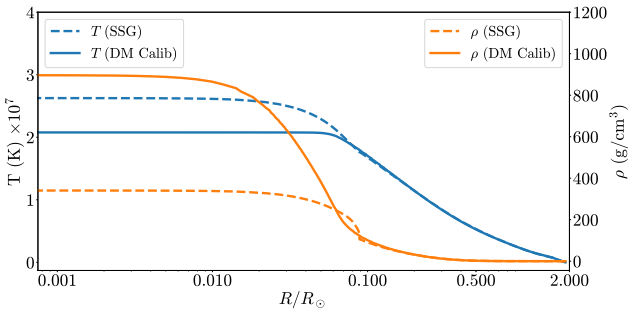

Figure 2. Temperature (left axis) and baryonic density (right axis) profiles of the SSG and DM Calib stellar models (see Table 1).

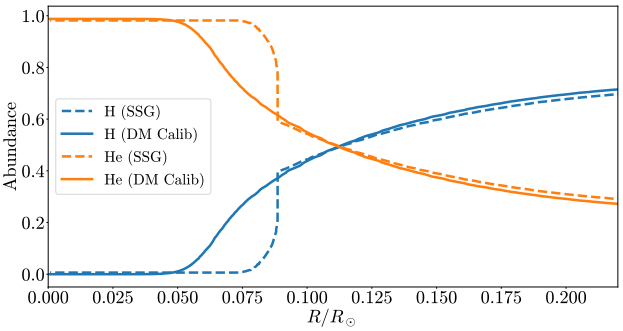

Figure 3. Hydrogen and helium abundances of the SSG and DM Calib stellar models (see Table 1).

This is a direct consequence of the stellar core being radiative, as opposed to convective, during the main-sequence: the arise of core convection during the MS promotes the homogenisation of the chemical species in the central regions of the star, and thus the exhaustion of hydrogen that characterises the end of the MS occurs everywhere within the convective zone – instead of locally in centre of the star.

One other effect that is found in this model is the extension of the MS lifetime (Lopes & Lopes 2019). While the star with DM has a radiative core during the largest part of its MS lifetime, and thus nuclear burning is limited to the local hydrogen supply, the decrease in central temperature slows down the hydrogen burning rate thus extending the MS lifetime. The age of the model itself may be another indicator of this effect since the best agreements with observations (which are the goals of a successful calibration) were found to be at a later stellar age than in the standard case.

In addition to the model DM Calib, we decided to repeat the calibration process accounting for DM effects, but instead with predefined fixed values of m_χ and $\sigma_{\rm SD}$. Stellar DM models from A to D are the best models for each of the (m_χ, $\sigma_{\rm SD}$) pairs showcased in Table 1. The first conclusion to be taken is that DM Calib, which produced an optimal pair of (m_χ, $\sigma_{\rm SD}$), does not have the lowest $\chi^2_{\rm star}$. This means that the full calibration optimisation method most likely hit a local minimum around the displayed values.

A closer inspection at the remaining columns of Table 1 reveals that the SSG model, DM A and DM B all share similar outputs. The same happens for models DM Calib, C and D, where the latter slightly deviates from the rest, leading to a $\chi^2_{\rm star}$ of an higher order of magnitude. These two distinct regimes are expected once we take

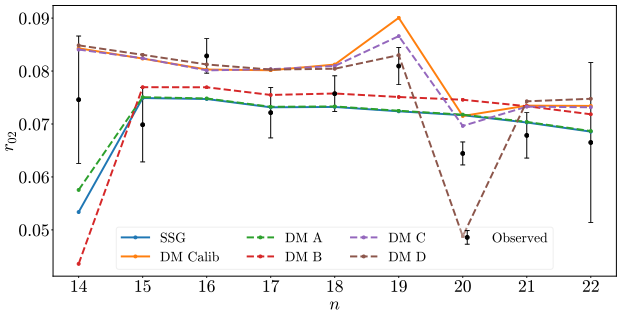

Figure 4. r_{02} ratios (see eq. (5)) for the models in Table 1 compared to observations. The dashed lines represent the 4 models with fixed values of (m_χ, $\sigma_{\rm SD}$).

into account the mass and cross-section values of the dark matter impacted models: for $\sigma_{\rm SD} \geqslant 10^{-36}$ cm^2 the effects from ADM interactions have a noticeable impact on the star, while for smaller values of $\sigma_{\rm SD}$ the effects are mostly negligible. We also confirm the prevalence of the two regimes when drawing profiles similar to Figs. 2 and 3 for the remaining models, i.e., the curves of Standard, DM A and DM B have similar behaviour between themselves whilst the remaining models follow the signature of DM Calib.

Finally, it is interesting to note that some DM models have a lower $\chi^2_{\rm star}$ than the SSG model. For DM Calib, the decrease in almost 8% of this quantity is substantial and the fact that DM A, B and C also represent an improvement on the Standard model's value reinforces the argument that the existence of DM is not incompatible with the current observational data for this star. However, the $\chi^2_{r_{02}}$ diagnostic increased in about 4% for DM Calib (even more for DM B) which hints towards the fact that the model might have fallen victim to an equivalent of overfitting. This means that, since the optimisation is done with respect to $\chi^2_{\rm star}$, other parameters of the star might have been affected to achieve a better performance in that specific diagnostic. Either way, the deviation on $\chi^2_{r_{02}}$ is not as significant as in the previous diagnostic. To better infer on the $\chi^2_{r_{02}}$ discrepancy, we compute $r_{02}(n)$ as shown in Fig. 4.

The results for $r_{02}(n)$ show that although the DM Calib ratio values deviate more from the observational average than the SSG's, the behaviour pattern is similar to that of the observed r_{02} (particularly around $n \sim 19-20$). Fig. 4 also shows that model DM C has the same regime as DM Calib, but slightly closer to the observation values, which is reflected in its smaller $\chi^2_{r_{02}}$.

Again, the two regimes are distinctively visible, with DM B being somewhat of an intermediate model. This is also expected since in this model $\sigma_{\rm SD}$ is in-between that of DM A and DM C, which showcase each one of the two different regimes.

6 ASTEROSEISMIC ANALYSIS

6.1 Probing the parameter space $m_\chi - \sigma_{\rm SD}$

Using the input stellar parameters of the SSG model as benchmark (see Table 1) and enabling DM interactions, we decide to explore the sensibility of the models in DM parameter space. This is achieved by computing 100 models in a $m_\chi - \sigma_{\rm SD}$ grid with fixed dark matter parameters within the range $4 \leqslant m_\chi \leqslant 12$ GeV and $10^{-40} \leqslant \sigma_{\rm SD} \leqslant 10^{-35}$ cm^2. As before, this range of values was chosen in agreement with the DM parameter space usually explored in the literature (e.g., Martins et al. 2017). Each input group in this grid was then used

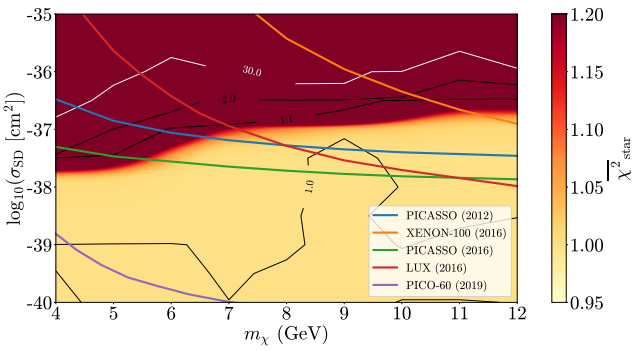

Figure 5. Contours for $\overline{\chi}^2_{star}$ (see eqs. (4) and (7)): lighter shades represent lower χ^2 and thus better models for this specific diagnostic. The contour for $\overline{\chi}^2_{star} = 1$ represents models as good as the SSG model. Direct detection experiment results from XENON-100 (Aprile et al. 2016), LUX (Akerib et al. 2016), PICASSO (Archambault et al. 2012; Behnke et al. 2017) and PICO-60 (Amole et al. 2019) are shown as solid lines.

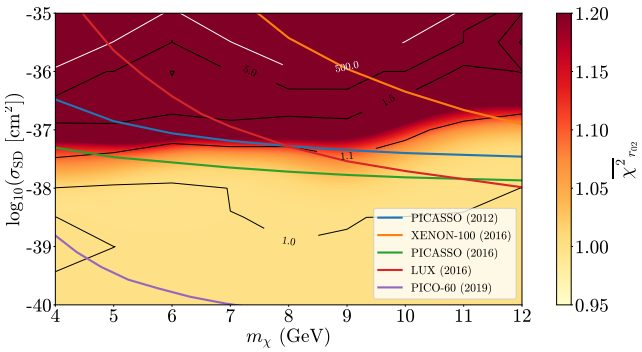

Figure 6. Contours for $\overline{\chi}^2_{r_{02}}$ (eq. (6) and normalised similarly to eq. (7)): lighter shades represent lower χ^2 and thus better models for this specific diagnostic. The contour for $\overline{\chi}^2_{r_{02}} = 1$ represents models as good as the SSG model. Direct detection experiment results from XENON-100 (Aprile et al. 2016), LUX (Akerib et al. 2016), PICASSO (Archambault et al. 2012; Behnke et al. 2017) and PICO-60 (Amole et al. 2019) are shown as solid lines.

to create a model (i.e., one single model, differently from the optimisation process discussed in the previous sections) for which χ^2_{star} was computed, allowing for the drawing of contour plots showcasing the parameter region of interest and corresponding DM parameters (Fig. 5).

A normalised $\overline{\chi}^2_{star}$ was defined as:

$$\overline{\chi}^2_{star} = \frac{\chi^2_{DM}}{\chi^2_{SSG}}, \tag{7}$$

where χ^2_{DM} corresponds to the χ^2_{star} of each model taking DM into account and, likewise, χ^2_{SSG} is that same value for the Standard model (in this case $\chi^2_{SSG} = 5.735\times10^{-3}$, see Table 1).

On the one hand, it is visible that the overall tendency is for stellar models with lower interaction cross-section to agree better with observations. On the other hand, there are some models with higher σ_{SD} that do not converge, meaning that the benchmark input parameters coupled with the given DM quantities cannot converge to an acceptable solution of the stellar evolution differential equations. This happened for models with σ_{SD} larger than 4×10^{-36} cm^2, where although not explicitly shown in the figure, the χ^2 values rose to orders of magnitude of 10^2. This relation between the cross-section and $\overline{\chi}^2_{star}$ is somewhat expected since the lower the σ_{SD} the smaller the influence of DM is on the stellar structure. Thus, the lower region of the grid performs better than the upper region since it naturally tends to the SSG case. However, it is still worth noting that for σ_{SD} as high as 10^{-37} cm^2 some models seem to perform well.

Furthermore, by looking at the contour line that defines models as good as the SSG model (at $\overline{\chi}^2_{star} = 1$, see Fig. 5), it is visible that a large portion of the 100 DM stellar models outperform it. This means that most dark matter models with the same inputs as the SSG but with m_χ between 4 and 12 GeV and σ_{SD} between 10^{-40} and 4×10^{-39} cm^2 fit the spectroscopy and large frequency separation observations better than the best performing no-DM model. It should be noted that despite the fact that $\sigma_{SD} = 10^{-40}$ cm^2 is a hard limit, i.e., it was chosen by default, that doesn't mean that the improvement in $\overline{\chi}^2_{star}$ is observed for any σ_{SD} below this value. In fact, we also obtained models below the minimum cross-section considered in Fig. 5 (e.g., $\sigma_{SD} = 10^{-42}$ cm^2) and observed that the χ^2_{star} diagnostic again tended to the SSG value (i.e., $\overline{\chi}^2_{star} = 1$), which is expected since DM is less influential for lower interaction cross-sections. Additionally, we found a model near $m_\chi = 9$ GeV and $\sigma_{SD} = 3 \times 10^{-38}$ cm^2 that exhibits the lowest χ^2_{star} of the set.

It is interesting, however, to study the performance of the best performing model and all the others under the $\chi^2_{r_{02}}$ diagnostic defined in Section 3.2. To achieve that, the r_{02} ratio was computed for all models in the grid and compared to observations, i.e., the ratio that was computed with the 32 frequencies observed in the star. After that, $\chi^2_{r_{02}}$ was computed and yet again plotted in contours.

The results shown in Fig. 6 confirm the overall trend seen before in Fig. 5: models in the lower region of the grid seem to more accurately agree with the observed r_{02} which, in itself, grants more confidence to the previous results. The contour that defines models with similar performance to that of the SSG model was again explicitly drawn at $\overline{\chi}^2_{r_{02}} = 1$. Once more, most models with $\sigma_{SD} < 10^{-38}$ cm^2 outperform the best model with no dark matter interactions, this time on a different diagnostic that better represents the core structure.

It is also interesting to note that the best performing model of the previous set (Fig. 5) is not in the same region of the best performing models in the $\chi^2_{r_{02}}$ diagnostic. This is a case where the spectroscopic results out-shadowed the structural differences in the first diagnostic, which was then covered by calculating the r_{02} ratio. Hence, the two step rejection method proves to be valuable in cases like this, since normally that model would have been accepted by passing the χ^2_{star} diagnostic with the lowest value.

A simple additional test can be done by combining the two methods, taking the maximum value of both diagnostics, $\overline{\chi}^2_{total} = \max(\overline{\chi}^2_{star}, \overline{\chi}^2_{r_{02}})$. This is shown in Fig. 7, as well as the region within the $\overline{\chi}^2_{total} = 1$ contour which represents the models that outperform the SSG model in both diagnostics.

When comparing the aforementioned grids with the direct detection experiment's limits we see that our method could provide complementary $m_\chi - \sigma_{SD}$ exclusion diagrams. This could be achieved by defining a cut-off χ^2 since it is visible that there is a steep transition region between the two regimes (from yellow to dark red) which indicates a rapid disagreement between the stellar models and the observational data. The behaviour showcased in Figs. 5 - 7 can be compared to that of the limits from PICASSO (2012; 2017) and LUX (2016). Moreover, it seems to suggest harder limits than those of XENON-100 (2016), which is not as competitive for lower m_χ. Taking into account the SSG model as the benchmark we can hint

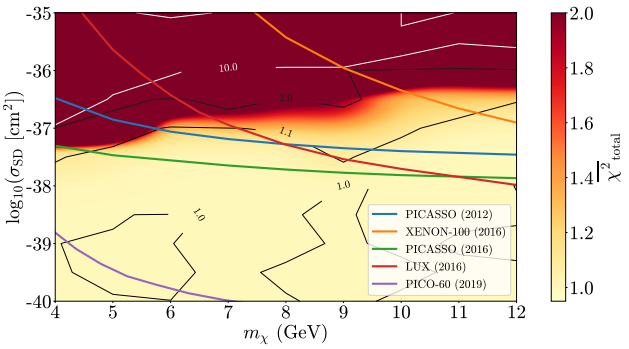

Figure 7. Maximum value between χ^2_{star} and $\chi^2_{r_{02}}$: the contour for $\overline{\chi}^2_{total} = 1$ represents the models with an equated performance to the SSG model, using their worst diagnostic. Direct detection experiment results from XENON-100 (Aprile et al. 2016), LUX (Akerib et al. 2016), PICASSO (Archambault et al. 2012; Behnke et al. 2017) and PICO-60 (Amole et al. 2019) are shown as solid lines.

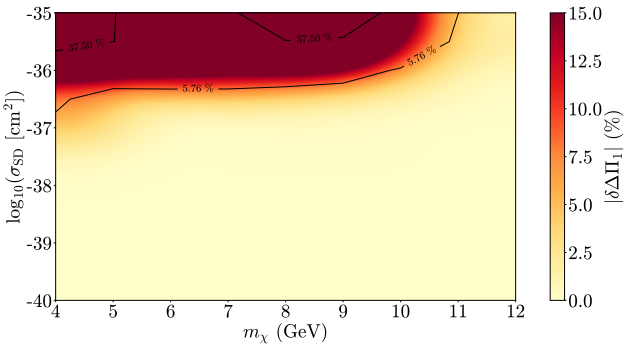

Figure 8. Contour plot of the deviation of the period separation $\Delta\Pi_1$ from the SSG model for the same grid of DM models. The two black curves represent the lower and upper boundaries of the relative error of measurement of this quantity for 39 SG stars from Mosser et al. (2014) (Lopes et al. 2019).

towards the region with $\sigma_{SD} \gtrsim 10^{-37}$ cm^2 where $\overline{\chi}^2_{total}$ rapidly increases, meaning that ADM presence in this SG star is strongly disfavoured by both spectroscopic and seismic observations.

Finally, it should be noted that the models obtained in the previous section – which were obtained by calibrating the stellar and, in the case of DM Calib, the DM parameters – can fall in the excluded region suggested in Fig. 7 (see Table 1) and still yield stellar models that are in agreement with the observational data. This may be due to the increase in the degrees of freedom associated with the extra free parameters which, given that the observational error for the star in question is substantial, allows the method to find different combinations of parameters that still fit the reality. Therefore, with access to more precise measurements from future spectroscopy and asteroseismology missions, one can expect to calibrate a standard benchmark model that allows the drawing of exclusion diagrams with more certainty.

6.2 Period Spacing Analysis

When further analysing the oscillation eigenfunctions of several models, it is clear that the amplitude rapidly falls off within the first outer 20% of the star radius. This means that despite using a seismic ratio that is designed to gather more information about the stellar interior, the acoustic modes that defined the diagnostic fall short on this task. Thus, we can conclude that the r_{02} diagnostic is not as sensitive to the core as expected, being more representative of the stellar envelope, contrary to what happens in a typical MS star.

Motivated by this, we change our focus to the gravitational character of the oscillations, which, as seen before, should be specially sensitive to the stellar interior. This is done by analysing the mixed modes of the various models, which allows the extraction of the relevant quantities of the gravity contribution.

In particular, the asymptotic value of the large period separation presented in eq. (3) can be computed from the MESA models for $\ell = 1$ and $\ell = 2$, for which there are mixed modes. It is expected that if the presence of DM in stars directly affects the size of their convective cores, as we have seen in previous sections, then the period spacing will serve as a good probing tool (Lopes et al. 2019). The $\Delta\Pi_\ell$ values are shown in the two last columns of Table 1. The already mentioned regimes are once again clearly noticeable: there is a substantial decrease in period spacing when DM is strongly influential that can go up to 66% of the benchmark value (from SSG). This, again, is explained by the suppression of the convective core caused by DM, which in turn leads to an increase of the g-mode cavity, producing a direct effect on the integral in eq. (3).

As before, we define the $\Delta\Pi_\ell$ deviation from the SSG model for the same grid of DM models to better understand the impact that the different DM parameters have on the core of the star. The variation of $\Delta\Pi_1$ is shown in Fig. 8. We only show the case with $\ell = 1$, given that, by definition, in the asymptotic limit, $\Delta\Pi_1$ and $\Delta\Pi_2$ only differ by a multiplying constant. The darker region represents models where $|\delta\Delta\Pi_1|$ is larger than 15% and, in some cases, models reach the 60% mark as was already the case for some models in Table 1. It is also clear that larger masses of ADM particles tend to result in less effects. This is twofold: first, these particles are harder to capture by virtue of requiring a larger transfer of momentum upon recoil in order to reach a velocity lower than the escape velocity (e.g., Gould 1987; Nuñez-Castiñeyra et al. 2019); secondly, if eventually captured, they cluster strongly in the innermost regions of the star and, thus, their impact is naturally not felt as much. It is important to note that most of the deviations shown in the grid happen in the negative direction, with DM impacted models exhibiting a smaller period spacing, as expected.

The overall tendency in Fig. 8 mimics that of Figs. 5 - 7: models in the upper part of the grid show a larger ADM influence on the star. Yet again, the transition region between the two regimes is narrow. The region below the 5.76% contour represents models whose $\Delta\Pi_1$ variation is lower than the lowest relative uncertainty among the large period separation measurements in Mosser et al. (2014). Likewise, models above the 37.50% curve exhibit a variation that surpasses the uncertainty of the less precise measurements. Both these statements mean that current experiments may not have enough sensitivity to resolve DM signatures in SG stars in the transition region (where the lower relative uncertainty contour is) and particularly in the region below the 37.50% contour. Above that curve, the effect should be detected, with the deviation being greater than the observable uncertainty in the worst cases. However, one should note that if this analysis is carried out for a SG star which allows for a more precise measurement of $\Delta\Pi_1$ (i.e., closer to the 5.76% mark) there should be enough sensitivity to draw any valuable conclusions regarding the acceptability of DM models for that star. In the future, this diagnostic could be used with measurement data as the benchmark, providing a strong case for model rejection and, additionally, ADM parameter constraints.

7 CONCLUSIONS

Subgiant stars are but a small fraction of the currently observed stars by virtue of that evolutionary stage being relatively short. Despite that, they can pose as important laboratories for the study of dark matter constraints. In this work, we obtained calibrated stellar models of the subgiant KIC 8228742 assuming both the presence and absence of asymmetric DM spin-dependent interactions. Focusing on SD interactions allows us to directly compare our results to the corresponding constraints placed by detectors which study the same type of interactions. More importantly, by studying only spin dependent couplings, we essentially neglect interactions with elements heavier than hydrogen , and thus also any direct effect that DM has on the star during the SG phase. Then, by carrying out this study we take advantage of the seismological benefits of the SG phase to study DM interactions in the MS stage.

The results shown here point towards the fact that, overall, DM models are in agreement with current observations of this star.

Firstly, in an attempt to study the possibility of ADM presence in SG stars, we introduce dark matter parameters into the calibration and optimisation processes. This is a new approach which aims to find the best models, in terms of the diagnostics here proposed, disregarding any prior standard (with no dark matter influence) benchmark models. Calibrated models with strong DM influence showcased a different regime from both the standard (SSG) model and DM models with lower $\sigma_{\rm SD}$. Phenomena like the suppression of the convective core, the cooling of the inner core and the increase in density of that region were all present and in agreement with past findings (e.g., Taoso et al. 2010; Casanellas & Lopes 2013; Casanellas et al. 2015; Lopes & Silk 2002). We later conclude that the results obtained at this stage of the work, which provided an optimal pair of ADM particle mass and spin-dependent cross-section of $m_\chi = 9.12$ GeV and $\sigma_{\rm SD} = 2.32 \times 10^{-36}$cm^2 may not be sufficient to constrain the DM particle candidates' properties. A number of limitations can be pointed out as the cause for this. The number of spectroscopic quantities of this star that we have measurements for pose a problem when introducing more parameters into the input group, since overfitting – typical of situations where there are too many parameters relative to the available data points – may be happening here. The precision of the current measurements is also a factor since it broadens the accepted model spectrum and limits the certainty of a possible exclusion limit. Lastly, computational time constraints were a large limitation to the minimisation problem and this is an aspect that has the potential for clear improvements.

Using seismological diagnostics as a second probing tool, we then present a method to study the influence of DM in the interior of stars, with direct applicability to SGs. The r_{02} ratio is used in an attempt to probe the stellar core, which is the region that ADM severely impacts. A study of the deviation of r_{02} from observational measurements allows us to draw several sensitivity grids (Figs. 5 - 7) which showcase the increasing influence that DM has with the increase of the spin-dependent cross-section of the interaction between ADM particles and stellar matter.

Moreover, those same figures show a class of models with $10^{-40} \leqslant \sigma_{\rm SD} < 10^{-38}$ cm^2 that consistently outperform the best standard models, which strengthens the argument that the presence of ADM particles in this star is consistent with observations. Additionally, a $\sigma_{\rm SD}$ admissible region is suggested for values up to 10^{-37} cm^2 where the χ^2 diagnostics start to deteriorate from observations. This value is comparable to those of the PICASSO (2012; 2017) and LUX (2016) experiments and improves that of XENON-100 (2016). Then, an exclusion limit may be drawn with more certainty at $\sigma_{\rm SD} \gtrsim 10^{-35}$ cm^2 since results from both Section 5 and 6 find this region as incompatible with current observations. This conclusion is similar to what Casanellas & Lopes (2013) and Martins et al. (2017) found previously for MS stars.

Lastly, we propose an additional seismic parameter to study DM influence on SG stars that allows us to further probe the stellar core. As the acoustic modes were mainly probing the stellar envelope (contrary to what typically happens in MS stars), we turned our attention to gravity and mixed modes, which carry more information about the core since they travel deeper into the stellar interior. The $\Delta\Pi_\ell$ diagnostic was calculated for the same grid of models and the results again confirm the previous analysis and hint towards the possibility of drawing exclusion diagrams for a SG star for which we have the $\Delta\Pi_\ell$ observations.

In the future, missions like PLATO (Rauer et al. 2014) which will provide high precision measurements of both spectroscopic and seismic quantities, will allow for a more extensive analysis of the impact of ADM in stars and, more importantly, will make the drawing of exclusion diagrams possible, using the method we present here. With better measurements, we also expect the calibration with DM quantities as inputs to provide a better result, with less impact from numerical constraints.

Another aspect to consider in the future is the inclusion of spin-independent interactions which will certainly drive the DM impact in the later stages of the stellar evolution, by allowing the interaction with helium and heavier elements as well.

ACKNOWLEDGEMENTS

We thank Bill Paxton and all MESA contributors along with Jørgen Christensen-Dalsgaard (ADIPLS: Christensen-Dalsgaard (2008)) and Rich Townsend (GYRE: Townsend & Teitler (2013), Townsend et al. (2018)) for making their code and work publicly available. Additionally, we acknowledge the Brown University's Particle Astrophysics Group for maintaining the DMTools database and plotting resources.

J.L. acknowledges financial support from Fundação para a Ciência e Tecnologia (FCT) grant No. PD/BD/128235/2016 in the framework of the Doctoral Programme IDPASC—Portugal.

I.L. thanks the Fundação para a Ciência e Tecnologia (FCT), Portugal, for the financial support to the Center for Astrophysics and Gravitation (CENTRA/IST/ULisboa) through the Grant Project No. UIDB/00099/2020 and Grant No. PTDC/FIS-AST/28920/2017.

DATA AVAILABILITY

This article makes use of the MESA stellar evolutionary code that is available for free in the public domain and can be found at the Zenodo repository with the DOI: 10.5281/zenodo.3473377. All of the data sets used in this work can be found in the MESA files for the release version r12115. The GYRE code has also been used to compute oscillations, and is also available for free in `https://github.com/rhdtownsend/gyre` with the corresponding documentation in `https://gyre.readthedocs.io/`. The data sets for the exclusion limits of the direct detection experiments shown in this work are publicly available upon registration in `http://dmtools.brown.edu/`. The remaining data underlying this article will be shared on reasonable request to the corresponding author.

REFERENCES

Aerts C., Christensen-Dalsgaard J., Kurtz D. W., 2010, Asteroseismology. Springer
Akerib D., et al., 2016, Phys. Rev. Lett., 116
Amole C., et al., 2019, Phys. Rev. D, 100
Appourchaux T., et al., 2012, A&A, 543, A54
Aprile E., et al., 2016, Phys. Rev. D, 94
Archambault S., et al., 2012, Phys. Rev. B, 711, 153–161
Asplund M., Grevesse N., Sauval A. J., Scott P., 2009, ARA&A, 47, 481–522
Bahcall J. N., Serenelli A. M., Basu S., 2005, ApJ, 621, L85–L88
Barger V., Keung W.-Y., Shaughnessy G., 2008, Phys. Rev. D, 78
Behnke E., et al., 2017, Astropart. Phys., 90, 85–92
Bellinger E. P., Hekker S., Angelou G. C., Stokholm A., Basu S., 2019, A&A, 622, A130
Beringer J., et al., 2012, Phys. Rev. D, 86, 010001
Bertone G., 2010, Nature, 468, 389–393
Bertone G., Hooper D., 2018, Rev. Mod. Phys., 90
Bertone G., Hooper D., Silk J., 2005, Phys. Rep., 405, 279
Borucki W. J., et al., 2010, Science, 327, 977
Bouquet A., Salati P., 1989, ApJ, 284-288
Capelo D., Lopes I., 2020, MNRAS, 498, 1992–2000
Casanellas J., Lopes I., 2010, MNRAS, 410, 535–540
Casanellas J., Lopes I., 2013, ApJ, 765, L21
Casanellas J., Brandão I., Lebreton Y., 2015, Phys. Rev. D, 91, 103535
Catena R., Ullio P., 2010, J. Cosmology Astropart. Phys., 2010, 004–004
Chaplin W. J., et al., 2013, ApJS, 210, 1
Christensen-Dalsgaard J., 2002, Rev. Mod. Phys., 74, 1073–1129
Christensen-Dalsgaard J., 2008, Ap&SS, 316, 113
Deheuvels S., Brandão I., Silva Aguirre V., et al., 2016, A&A, 589, A93
Dupret M.-A., et al., 2009, A&A, 506, 57
Floranes H. O., Christensen-Dalsgaard J., Thompson M. J., 2005, MNRAS, 356, 671
Frandsen M. T., Sarkar S., 2010, Phys. Rev. Lett., 105
Fridlund M., Baglin A., Lochard J., Conroy L., 2006, ESA, 1306
Gai N., Tang Y., Yu P., Dou X., 2017, ApJ, 836, 3
Gould A., 1987, ApJ, 321, 571
Gould A., 1990, ApJ, 356, 302
Gould A., Raffelt G., 1990, ApJ, 352, 669
Grosjean M., Dupret M.-A., Belkacem K., et al., 2014, A&A, 572, A11
Hekker S., Mazumdar A., 2013, Proc. Int. Astron. Union, 9, 325–331
Hurley J. R., Pols O. R., Tout C. A., 2000, MNRAS, 315, 543–569
Koch D. G., et al., 2010, ApJ, 713, L79
Kouvaris C., 2015, Phys. Rev. D, 92
Lopes J., Lopes I., 2019, ApJ, 879, 50
Lopes I. P., Silk J., 2002, Phys. Rev. Lett., 88
Lopes I., Silk J., 2010, The Astrophysical Journal, 722, L95–L99
Lopes I., Turck-Chieze S., 1994, A&A, 290, 845
Lopes I. P., Silk J., Hansen S. H., 2002a, MNRAS, 331, 361
Lopes I. P., Bertone G., Silk J., 2002b, MNRAS, 337, 1179
Lopes I., Panci P., Silk J., 2014, ApJ, 795, 162
Lopes J., Lopes I., Silk J., 2019, ApJ, 880, L25
Martins A., Lopes I., Casanellas J., 2017, Phys. Rev. D, 95, 023507
Metcalfe T., 2014, AMP | Run Details | KIC 8228742, https://amp.wdrc.org/browse/simulation/648/
Metcalfe T. S., et al., 2012, ApJ, 748, L10
Metcalfe T. S., et al., 2014, ApJS, 214, 27
Michel E., et al., 2008, Science, 322, 558
Molenda-Żakowicz J., et al., 2013, MNRAS, 434, 1422–1434
Mosser B., et al., 2014, A&A, 572, L5
Nelder J. A., Mead R., 1965, Comput. J., 7, 308
Nuñez-Castiñeyra A., Nezri E., Bertin V., 2019, J. Cosmology Astropart. Phys., 2019, 043–043
Paxton B., Bildsten L., Dotter A., et al., 2011, ApJS, 192, 3
Paxton B., Cantiello M., Arras P., et al., 2013, ApJS, 208, 4
Paxton B., Marchant P., Schwab J., et al., 2015, ApJS, 220, 15
Paxton B., Schwab J., Bauer E. B., et al., 2018, ApJS, 234, 34
Paxton B., Smolec R., Schwab J., et al., 2019, ApJS, 243, 10
Rauer H., et al., 2014, Exp. Astron., 38, 249–330
Renzini A., 1987, A&A, 171, 121
Ricker G. R., Winn J. N., Vanderspek R., et al., 2014, J. Astron. Telesc. Instrum. Syst., 1, 014003
Roxburgh I. W., Vorontsov S. V., 2003, A&A, 411, 215
Rubin V. C., et al., 1976, AJ, 81, 687
Salaris M., Cassisi S., 2006a, The Hydrogen Burning Phase. John Wiley & Sons, Ltd, pp 117–159, doi:10.1002/0470033452.ch5, https://onlinelibrary.wiley.com/doi/abs/10.1002/0470033452.ch5
Salaris M., Cassisi S., 2006b, The Helium Burning Phase. John Wiley & Sons, Ltd, pp 161–186, doi:10.1002/0470033452.ch6, https://onlinelibrary.wiley.com/doi/abs/10.1002/0470033452.ch6
Salaris M., Cassisi S., 2006c, The Advanced Evolutionary Phases. John Wiley & Sons, Ltd, pp 187–237, doi:10.1002/0470033452.ch7, https://onlinelibrary.wiley.com/doi/abs/10.1002/0470033452.ch7
Schumann M., 2019, J. Phys. G, 46, 103003
Shelton J., Zurek K. M., 2010, Phys. Rev. D, 82
Taoso M., et al., 2010, Phys. Rev. D, 82, 083509
Tassoul M., 1980, ApJ, 43, 469
Townsend R. H. D., Teitler S. A., 2013, MNRAS, 435, 3406
Townsend R. H. D., Goldstein J., Zweibel E. G., 2018, MNRAS, 475, 879
Turck-Chièze S., García R., Lopes I., et al., 2012, ApJ, 746, L12
Undagoitia T. M., Rauch L., 2015, J. Phys. G, 43, 013001
Verma K., et al., 2018, MNRAS, 483, 4678
Vincent A. C., Scott P., Serenelli A., 2015, Phys. Rev. Lett., 114

This paper has been typeset from a TEX/LATEX file prepared by the author.